Towards the modelling of a spray flame process for nanoparticle synthesis

Von der Fakultät für Ingenieurwissenschaften,
Abteilung Maschinenbau und Verfahrenstechnik
der
Universität Duisburg-Essen
zur Erlangung des akademischen Grades

einer

Doktorin der Ingenieurwissenschaften

Dr.-Ing

genehmigte Dissertation

von

Claudia Weise
aus
Hamm

Gutachter: Univ.-Prof. Dr.-Ing Andreas Kempf
Univ.-Prof. Dr.-Ing. habil. Lutz Mädler

Tag der mündlichen Prüfung: 12.10.2015

Abstract

This work concerns the investigation of nanoparticle synthesis processes with focus on the synthesis of titanium dioxide nanoparticles from titanium tetraisopropoxide (TTIP) in a nanoparticle spray flame reactor.

As important steps towards the complex modelling of the spray process, simpler nanoparticle synthesis processes without spray were examined first. These preliminary studies helped to understand the flow field and the influence of different process parameters, and to generate experience in gas-phase synthesis reactor modelling. Therefore, the synthesis process within a hot-wall reactor, a low-pressure microwave plasma reactor and a low-pressure flat flame reactor was investigated by means of computational fluid dynamics (CFD).

For the analysis of the spray flame reactor, different modelling approaches for a complete reactor simulation are introduced, where one major aspect for all approaches was to keep the computational effort low while achieving sufficient accuracy. The several processes within the reactor can be divided in three main parts: a) the break-up of the liquid jet from the spray nozzle, b) the combustion of the spray and in the pilot flame, and c) the formation and growth of the nanoparticles. Additionally, the interaction between turbulence and nanoparticle dynamics had to be considered, which has been a key part of this thesis. Due to many simultaneous and interacting physical processes of such a spray flame synthesis, the modelling was quite challenging. First, the primary break-up had to be analysed to determine the spray droplet properties, which were required as boundary conditions for further simulations of the complete synthesis process. Therefore, Volume of Fluid (VOF) modelling was performed and shadowgraphs provided by Jan Menser were used, which both together delivered good estimations of the droplet characteristics. For the modelling of the turbulent spray combustion and the calculation of the nanoparticle dynamics, different modelling approaches were used. To break the first ground, the Partially Stirred Reactor (PaSR) concept was used to model the turbulent combustion. The simplified population balance equations (PBE) for the calculation of the nanoparticle dynamics were solved coupled to the combustion using a monodisperse model and an Eulerian approach. With this method a sensitivity study was performed applying modified droplet properties as boundary conditions to analyse their influence on the combustion and the nanoparticle characteristics and to quantify the effect of the uncertainties in the boundary conditions. Additional simulations were performed using the Eddy Break-Up (EBU) model for turbulent combustion, where the monodisperse PBE were solved in a post-processing step in the Eulerian frame. Finally, a simplified hybrid Lagrangian Monte Carlo approach was used for a more complex and precise modelling of the turbulence-PBE interactions, where the Monte Carlo particle statistics were used to calculate discrete probability density functions (PDF) of the nanoparticle characteristics.

The modifications of the spray boundary conditions for the PaSR simulation were found to have a negligible effect on the flame and the final nanoparticle size distribution, which indicates a stable reactor design. The PaSR simulation has given a first insight into the investigated reactor and particularly into the nanoparticle synthesis process. The EBU model predicted a slightly wider spray flame, which was shifted further downstream of the reactor nozzle in comparison to the PaSR model. The nanoparticle properties were in the same range, but due to the later precursor decomposition, the EBU model determined a slightly lower nanoparticle surface area, volume and primary nanoparticle diameter. Due to the short computational time, the Euler-Euler modelling approaches are well suited to conduct parameter studies in nanoparticle reactors. Whereas for the Euler-Euler simulations the precursor decomposed rapidly and all nanoparticles emerged at the same time at a low height above the nozzle, the Monte Carlo model has shown that newly formed and older nanoparticles coexist and feature different properties. Monte Carlo particles with different trajectories at the same time and location were sampled, where particle statistics could be derived for each individual computational cell. The mean of the nanoparticle properties determined by the Monte Carlo simulation were in the same range as predicted by the Euler-Euler approach for the multiphase flow. The Monte Carlo model could predict a bimodal nanoparticle size distribution in the population of the numerical particles due to different particle histories. This bimodal distribution was already observed for TiO2 formation in the gas-phase in different previous experiments, as for example by Tsantilis et al. [1], where it was ascribed to similar coagulation and nucleation modes. In this thesis, it is shown, that a bimodal size distribution can also be caused by turbulent phenomena.

Zusammenfassung

Diese Arbeit befasst sich mit der numerischen Simulation von Nanopartikelsynthese-prozessen. Den Schwerpunkt der Untersuchungen bildet die Modellierung der Synthese von Titaniumdioxid-Nanopartikeln aus Titanium-Tetraisopropoxid (TTIP) in einem Sprayflammenreaktor.

Wichtige Schritte hin zu der komplexen Gesamtmodellierung des Spray-Syntheseprozesses waren Modellierungen simplerer Syntheseprozesse ohne Sprayverbrennung. Diese vorausgehenden Studien gaben Aufschluss über das Strömungsfeld in Gasphasenreaktoren und den Einfluss verschiedener Betriebsparameter auf die Synthese. Außerdem generierten sie wichtiges Verständnis und Kenntnisse im Bereich der Reaktormodellierung. Die vorherigen Untersuchungen umfassten die Modellierung eines Heißwandreaktors, eines Niederdruck-Mikrowellenplasmareaktors und eines Niederdruck-Flachflammenreaktors mittels numerischer Simulation.

Für die Analyse des Sprayflammensynthesreaktors werden in dieser Arbeit verschiedene Modellierungsansätze zur Simulation des Gesamtprozesses vorgestellt. Ein Hauptaspekt für alle Modellierungsansätze war, den Rechenaufwand möglichst gering zu halten. Die Prozesse im Sprayflammenreaktor können grob in drei Hauptprozesse aufgeteilt werden: a) der Zerfall des Flüssigkeitsstrahls aus der Spraydüse, b) die Verbrennung des Sprays und in der Pilotflamme und c) die Bildung und das Wachstum der Nanopartikel. Zusätzlich muss der Einfluss der Turbulenz auf die Prozesse berücksichtigt werden. Die Wechselwirkungen zwischen Turbulenz und Nanopartikelentwicklung sind daher Kernstück dieser Arbeit. Durch die unterschiedlichen simultan ablaufenden und wechselwirkenden physikalischen Prozesse war die Gesamtmodellierung des Reaktors sehr komplex. Als erster Schritt musste der Primärzerfall des Flüssigkeitsstrahls untersucht werden, um die Randbedingung für die Spraytropfen für die Gesamtmodellierung zu bestimmen. Der Primärzerfall wurde mithilfe einer Volume of Fluid (VOF) Methode modelliert und zusätzlich wurden Schattenbilder, welche von Jan Menser bereitgestellt wurden, herangezogen. Beide Methoden zusammen lieferten eine gute Abschätzung der Tropfeneigenschaften. Zur Modellierung der turbulenten Sprayverbrennung und der Berechnung der Nanopartikelentwicklung wurden unterschiedliche Methoden verwendet. Als erster Schritt wurde das Partially Stirred Reactor (PaSR) Konzept zur Berechnung der turbulenten Verbrennung verwendet. Die Populationsbilanzgleichungen (PBE: population balance equations) zur Bestimmung der Entwicklung der Nanopartikel wurden mit einem monodispersen Ansatz modelliert und gekoppelt zur Verbrennungssimulation mittels eines Euleransatzes gelöst. Mit dieser Methode wurde eine Sensitivitätsstudie durchgeführt, um den Einfluss kleiner Abweichungen in den Spraytropfeneigenschaften auf die Nanopartikeldurchmesser, -anzahlen und -morphologien zu untersuchen. Diese Sensitivitätsstudie diente dazu, Unsicherheiten in der Definition der

Randbedingungen auszuschließen. Zusätzliche Simulationen wurden mit dem Eddy Break-Up (EBU) Model für turbulente Verbrennungen durchgeführt, bei denen die monodispersen vereinfachten PBE in einem Postprozessingschritt gelöst wurden. Schließlich wurde ein vereinfachter hybrider Lagrang'scher Monte Carlo Ansatz für eine komplexere und präzisere Modellierung der Turbulenz-PBE Interaktion verwendet. Monte Carlo Partikelstatistiken wurden hierbei zur Berechnung der diskreten Wahrscheinlichkeitsdichtefunktionen (PDF: probability density function) für die Nanopartikeleigenschaften herangezogen.

Die Modifizierung der Randbedingungen der Spraytropfen in den PaSR Simulationen zeigte keinen nennenswerten Einfluss sowohl auf die Verbrennung als auch auf die Nanopartikeleigenschaften, was auf einen stabilen Reaktorbetrieb schließen lässt. Die PaSR-Simulationen konnten einen ersten Einblick in den untersuchten Reaktor und in die Prozessabläufe während der Synthese geben. Das EBU-Modell lieferte eine etwas breitere nach oben verschobene Sprayflamme im Vergleich zum PaSR-Modell. Die Nanopartikeleigenschaften beider Methoden wiesen die gleichen Größenordnungen auf, jedoch waren die Durchmesser, die Oberflächen-, Volumen- und Anzahldichte beim EBU-Modell etwas kleiner als beim PaSR-Model, was auf eine spätere Umsetzung des Prekursors zurückzuführen ist. Durch die geringe Rechenzeit sind die Euler-Euler Simulationen, d.h. die PaSR- und die EBU-Simulation, zur Durchführung von Parameterstudien in Nanopartikelreaktoren gut geeignet. Bei den Euler-Euler Modellen wurde der Prekursor in der heißen Zone direkt umgesetzt und alle Nanopartikel entstanden zeitgleich. Die Monte Carlo Modellierung hat jedoch gezeigt, dass Nanopartikel mit unterschiedlichen Trajektorien zeitgleich an derselben Stelle existieren. Für jede individuelle Rechenzelle konnten Nanopartikelstatistiken abgeleitet werden. Die gemittelten Werte für die Nanopartikeleigenschaften waren in der gleichen Größenordnung wie die Ergebnisse der Euler-Euler Simulationen. Das Monte Carlo-Modell konnte eine bimodale Nanopartikel-größenverteilung im Reaktor vorhersagen, welche auf unterschiedliche Trajektorien der Partikel zurückzuführen ist. Diese bimodale Verteilung wurde für TiO_2-Gasphasensynthese bereits in Experimenten, z.B. von Tsantilis et al. [1], beobachtet und als Grund wurden ähnliche Koagulations- und Nukleationsmode aufgeführt. In der vorliegenden Arbeit wird jedoch gezeigt, dass die bimodale Größenverteilung auch auf turbulente Effekte zurückgeführt werden kann.

Acknowledgements

The present thesis was developed in the course of my activity as a research associate at the Institute for Combustion and Gasdynamics (IVG) at the University Duisburg-Essen.

I would like to express special thanks to my team leader and friend Dr.-Ing. Irenäus Wlokas for supporting me during my four years at the IVG. With his infinite knowledge he was always on hand with help and advice.

My gratitude goes also to my supervisor Prof. Dr.-Ing. Andreas Kempf, who led my work into the right direction. Many thanks for his excellence supervision and the many fruitful discussions. His ideas, and, not least, his determination in particular have contributed to the success of my work.

Furthermore, I would like to thank Prof. Dr. Christof Schulz for his supervision during my first year at the IVG and also for his professional support and the many technical discussions during my whole time at the IVG.

I also express my gratitude to my co-examiner Prof. Dr.-Ing. habil. Lutz Mädler for his interest in my thesis.

Acknowledgements go also to Jan Menser for the many nice results and images and for the fruitful and uncomplicated teamwork.

I would also like to thank all my colleagues, who made the four years really special. Despite the hard work and many worked through weekends, I really had a great time. Special thanks to my neighbor in the office and in Mülheim, Andreas Rittler and his wife Lisa, for their motivation, the nice evenings and the shuttle service.

Without my boyfriend Benni I would have lost my head. Therefore, I would like to thank him for his emotional support and of course for his programming expertise.

Index

List of Figures

1. Introduction

Nanoparticles can be found nearly everywhere in our environment, such as soot from combustion or volcanic ash. They are often released as (unwanted) by-products from technical processes for example in exhaust gases, but they can also be specifically produced. The synthesis of custom-tailored nanoparticles is state-of-the-art, where the particle properties and functionalities can be adjusted by modifying their size, shape and composition. Due to their small size with a maximum diameter of 100 nm (10^{-7} m), nanoparticles have a large specific surface area. Therefore, the physical and chemical properties of nanoparticles differ from that of macroscopic bulk materials. Nanomaterials feature special optical characteristics regarding their refraction index, their photo luminescence, their transparency, and their plasmon resonance [2, 3]. Nanoparticles are used for electrotechnical applications, for example in resistors and conductor material and for manufacture of magnetic materials [3]. Due to their large contact surface and boundary layer, nanoparticles are applied as catalysts and for the control of chemical reactions [4]. Nanomaterial-based catalysts are for example important for the synthesis of Diesel fuel or herbicides [5]. Biomedicine makes use of nanoparticles due to their porosity, functionality and their special properties for surface coating purposes [6]. Magnetic nanoparticles are used in biomedicine to deliver medicine to regions within the human body, for example to a tumour [7]. Additionally, biomimetic technology benefits from the so called nanobiotechnology [8]. Nanobiology techniques are for example used to culture bladders, for stem cell treatments or to produce artificial proteins [9].

The broad application area of nanomaterials results in a huge demand of large amounts of high specific nanoparticles. The gas-phase synthesis enables the production of nanoparticles with high purity with a narrow size distribution [10]. For this purpose, different reactor types are employed, which differ in their type of heat release. There are hot wall reactors [11-13], plasma reactors [14, 15] and flame reactors [16, 17]. In flame reactors, millions of tons of nanoparticles are produced annually, where high temperatures, steep temperature gradients and high production rates can be achieved [9, 18]. The flame synthesis delivers a wide range of feedstocks (SiO_2, TiO_2, ZrO_2, Al_2O_3) for the pigment industry, for fibre glass lines, as anticaking agents, as catalysts, and for the telecommunication industry [18], where the range of precursors is limited to gas-phase precursors for usual flame processes. The spray flame synthesis increases the range of possible precursors to liquid materials. For the spray-flame assisted synthesis, the precursor does not need to overcome the vapor pressure, because the liquid precursor is directly injected into the hot reaction zone. This technique increases the possibilities for the production of specific nanomaterials. For the spray flame process, the precursor is dissolved in a liquid fuel, which is injected into the reactor, forms a spray and evaporates. The gaseous fuel mixes with the inserted oxygen and burns. The nanoparticles are produced by nucleation and grow due to coagulation and sintering.

Due to the interaction of all mentioned processes and the turbulent flow within the reactor, the spray flame synthesis is a very complex physical system, which has not been sufficiently investigated and understood so far.

1.1. Motivation

The size distribution, morphology and purity of produced nanoparticles strongly depend on the operating conditions and the reactor design [19]. The gas composition, the used precursor, the mixing of the species within the reactor, the operating pressure and the temperature, all influence the particle properties and the production rate [9, 20, 21]. The geometry of the reactor and the operating condition dictate the flow field and therefore the particle residence time inside the reactor chamber and so the particle dynamics [22, 23]. The effect of the operating conditions on the particle formation and growth is analysed in laboratory scale reactors. The aim of all investigations is to optimize the production of high-specific nanoparticles to upscale the process from laboratory to industrial scale. For this purpose, the reactor processes must be fundamentally understood. These processes are the heat release within the reactor such as combustion, the particle formation and growth, additional processes, for example spray formation, and the possible interactions of these processes. The analysis of the interacting physical processes solely by experiments is nearly impossible, because most reactors are not accessible for in-situ diagnostics. A full investigation of the synthesis process, especially in turbulent flow reactors, is also very expensive or even not feasible, because it requires detailed measurements with corresponding statistics for each parameter such as species concentration, flow velocity, temperature, and particle size distribution. However, flow simulations known as computational fluid dynamics (CFD) in combination with calculations of the particle dynamics enable a three-dimensional analysis of the interacting processes during particle synthesis. Additionally, the influence of different process parameters on the particle formation and growth can be analysed efficiently by parameter studies by means of simulations. Hence, numerical modelling provides an insight into the reactor and helps to understand the synthesis processes.

This work addresses the modelling of a spray flame process for the production of metal-oxidic nanoparticles for the example of titanium dioxide nanoparticles from titanium tetraisopropoxide (TTIP). The focus of the study is on the determination of appropriate boundary conditions for the spray simulation and on the interaction of turbulence and particle formation and growth. Therefore, different modelling approaches to determine the turbulent flow field and the particle characteristics were applied and their results compared. Additionally, further research potential was detected and the sensitivity of the spray parameters on the produced particle properties investigated.

1.2. Structure of the thesis

The first part of this thesis gives a general introduction to the theoretical background and the modelling. Therefore, the physical basics and the modelling of turbulent combustion are explained in detail in chapter 2. Chapter 3 deals with the gas-phase synthesis of nanoparticles; the theory of particle synthesis is described, followed by the modelling of particle dynamics. The population balance equations (PBE) are introduced and the simplifications for its numerical solution are presented together with the modelling approaches for the turbulence-nanoparticle dynamics interaction. In section 4, the actual modelling approach for the spray process simulation using a simplified hybrid Lagrangian Monte Carlo method is presented, showing the Monte Carlo Finite Volume coupling, the algorithm strategy and the calculation of the statistics. Additionally, the limitations of the applied model are specified. The basics of numerical simulation are discussed in section 5, presenting the requirements for an appropriate simulation, the discretisation schemes, the pressure-velocity coupling and finally, the used software package OpenFOAM. Chapter 6 shows previous CFD investigations of other synthesis processes without spray injection, which are a hot-wall, a low-pressure microwave plasma, and a premixed low-pressure flat flame reactor process. These previous simulations were performed as a step towards the development of software and models. The modelling of the spray flame process for the synthesis of TiO_2 nanoparticles is presented in chapter 7. This chapter explains the experimental setup, the simulation and experimental investigations and finally shows and discusses the results. Lastly, in section 8, a conclusion and an outlook are given for all presented studies.

2. Theoretical background and modelling of turbulent combustion

During the spray flame synthesis, different interacting processes happen simultaneously within the reactor. The theoretical background of these processes is introduced in this chapter and their modelling approaches are discussed. First of all, the conservation equations for mass, momentum, energy, and species, which are necessary for the description of the gas-phase and hence the flow within the reactor, are described in chapter 2.1. This section is followed by the description of chemical reactions in chapter 2.2. Due to the high jet velocities, turbulence has to be considered and is therefore described in chapter 2.3 including corresponding modelling approaches. The liquid fuel and the dissolved precursor form a spray, for which in section 2.4 the theoretical background and the modelling approach are explained. The heat release inside the spray reactor is induced by turbulent combustion, which is announced with the applied models in section 2.5.

2.1. Conservation equations

Fluid mechanics and the corresponding conservation equations base on the principles of continuum mechanics. The fluid is treated as a continuum and its properties as continuous functions in the three-dimensional flow domain. These functions are determined by macroscopic values. Balance equations are used for the description of the flow into and out of a control volume. They are based on the conservation principle: everything that flows into a system will leave the system or will be accumulated. From this conservation principle, equations for mass, momentum, energy, and species can be derived, which are formulated as balance equations for a quantity φ, namely the density ρ, the momentum $\rho\boldsymbol{u}$, the specific enthalpy times density ρh, and the specific species mass fraction times density ρY for a control volume V. The conservation of mass, momentum and energy are well known as the Navier-Stokes-equations and are subsequently described for the flow of a Newtonian fluid.

The conservation principle for an intensive scalar φ can be expressed in general by the integral control volume equation in Equation 1:

$$\int_V \frac{\partial \varphi}{\partial t} dV + \oint_A \varphi \boldsymbol{u} \cdot \boldsymbol{n} dA = \int_V \boldsymbol{s} dV \tag{1}$$

In this formula $\boldsymbol{u}$ is the velocity, $\boldsymbol{n}$ the normal vector of the surface A of the volume boundary and $\boldsymbol{s}$ the sources as for example the volume forces for the momentum. The second term on the left-hand side (LHS) gives the fluxes normal to the volume surface and is denoted as convective term.

The conservation equation for the specific **mass** ρ is also known as continuity equation. The change of mass per time is equal the sum of in- and out-flowing mass normal to the volume boundary. The integral form of the mass conservation equation is:

$$\int_V \frac{\partial \rho}{\partial t} dV + \oint_A \rho \boldsymbol{u} \cdot \boldsymbol{n} dA = 0 \tag{2}$$

The divergence theorem converts the surface integral into a volume integral:

$$\int_V \frac{\partial \rho}{\partial t} dV + \int_V \nabla \cdot \rho \boldsymbol{u}\, dV = \int_V \left(\frac{\partial \rho}{\partial t} \nabla \cdot \rho \boldsymbol{u} \right) dV = 0 \tag{3}$$

By differentiating the resulting equation in respect to the volume, the continuity equation can be written in its differential form:

$$\frac{\partial \rho}{\partial t} + \nabla \cdot \rho \boldsymbol{u} = 0 \tag{4}$$

This form of equation is also called divergence form or conservative form. In multiphase flows, a mass balance can be formulated for each phase. Due to different processes, such as vaporization or condensation, a mass exchange between the different phases occurs, which has to be considered by sources and sinks in the mass balance equations of the phases. This exchange for example takes plays for a spray, which is discussed in chapter 2.4. The total mass of all phases is conserved.

The **momentum** of a fluid is the product of its (specific) mass and its velocity. The change of momentum in a volume plus the sum of the momentum fluxes and stresses normal to the volume boundary is equal the sum of the volume forces. The balance equation for the momentum in integral form is expressed in Equation 5.

$$\int_V \frac{\partial \rho \boldsymbol{u}}{\partial t} dV + \oint_A (\rho \boldsymbol{u}\boldsymbol{u} + p\boldsymbol{I} - \boldsymbol{T}) \cdot \boldsymbol{n} dA = \sum \int_V \boldsymbol{f_V} dV \tag{5}$$

In this equation, $\boldsymbol{pI}$ is the pressure tensor; the product of static pressure and the identity matrix. The product $\boldsymbol{uu}$ is a dyad product, which is a second order tensor. The stress tensor $\boldsymbol{T}$ considers additional normal and shear stresses on the fluid. The term on the right-hand side (RHS) sums up the volume forces $\boldsymbol{f_V}$, which are responsible for the acceleration of the fluid, for example due to buoyancy.

The divergence form of the momentum equation reads:

$$\frac{\partial \rho \boldsymbol{u}}{\partial t} + \nabla \cdot (\rho \boldsymbol{u}\boldsymbol{u} + p\boldsymbol{I} - \boldsymbol{T}) = \sum \boldsymbol{f_V} \tag{6}$$

The stress tensor $\boldsymbol{T}$ for a Newtonian fluid is described by Equation 7, where μ is the dynamic viscosity.

$$\boldsymbol{T} = \mu(\nabla \boldsymbol{u} + (\nabla \boldsymbol{u})^{\boldsymbol{T}} - \frac{\mathbf{2}}{\mathbf{3}} \boldsymbol{I}\, \nabla \cdot \boldsymbol{u}) \tag{7}$$

For an incompressible flow, the third term on the RHS vanishes:

$$\boldsymbol{T} = \mu(\nabla \boldsymbol{u} + (\nabla \boldsymbol{u})^{\boldsymbol{T}}) \tag{8}$$

The **energy** in a thermodynamic system can be expressed by the enthalpy. The enthalpy is the sum of the internal energy (thermal energy + chemical binding energy + potential energy of the atoms) and the volume work stored in the system, which is needed for the propagation of the observed system in space (system volume) in the direction of a pressure gradient.

The change of the specific enthalpy times density ρh in a control volume dV plus the sum of the in- and out-flowing energy and heat fluxes $\dot{\boldsymbol{q}}$ over the surface dA of the volume boundary is equal the sum of the power due to volume forces and the heat release due to chemical reactions $\dot{\omega}_h$. This correlation is described by the integral balance equation and its divergence form in Equation 9 and 10, respectively.

$$\int_V \frac{\partial \rho h}{\partial t} dV + \oint_A (\rho h \boldsymbol{u} + p \boldsymbol{I} \boldsymbol{u} - \boldsymbol{T} \boldsymbol{u} - \dot{\boldsymbol{q}}) \cdot \boldsymbol{n} dA = \int_V \boldsymbol{f_V} \boldsymbol{u} dV + \dot{\omega}_h \tag{9}$$

$$\frac{\partial \rho h}{\partial t} + \nabla \cdot (\rho h \boldsymbol{u} + p \boldsymbol{I} \boldsymbol{u} - \boldsymbol{T} \boldsymbol{u} - \dot{\boldsymbol{q}}) = \sum \boldsymbol{f_V}\, \boldsymbol{u} + \dot{\omega}_h \tag{10}$$

The heat release due to chemical reactions is described in subchapter 2.2.

The heat flux $\dot{\boldsymbol{q}}$ is determined by Fourier's law with the heat conductivity λ and depends on the gas composition and temperature:

$$\dot{\boldsymbol{q}} = -\lambda \nabla T \tag{11}$$

For a multispecies mixture with chemical reactions, additionally the balance of the **species** has to be considered. Mixing processes take place and reactions cause the production or consumption of certain species. The balance equation for a species *i* can be described by a conservation equation for the mass fraction of the species y_i in a control volume. The species mass fraction is defined as the ratio of the species mass and the total mass of all species in the system:

$$y_i = \frac{m_i}{\sum_j m_j} \tag{12}$$

The rate of change of the species mass fraction inside a control volume is balanced by the species mass flow into or out of the control volume, the species mass diffusion and the species mass production or consumption due to chemical reactions. The corresponding balance

equation is presented by Equation 13 in integral form and by Equation 14 in differential form, respectively.

$$\int_V \frac{\partial \rho y_i}{\partial t} dV + \oint_A (\rho y_i \boldsymbol{u} + \boldsymbol{J_i}) \cdot \boldsymbol{n} dA = \dot{\omega}_i \tag{13}$$

$$\frac{\partial \rho y_i}{\partial t} + \nabla \cdot (\rho y_i \boldsymbol{u} + \boldsymbol{J_i}) = \dot{\omega}_i \tag{14}$$

In the above equations, $\dot{\omega}_i$ is the production or the consumption rate of the species due to chemical reactions, which is described in subchapter 2.2, and $\boldsymbol{J_i}$ the diffusion flux of the species. Diffusion causes mixing of species: fluxes from regions with high concentrations to regions with lower concentrations result in concentration equilibrium for the system. A mixture without concentration differences is completely mixed. Ficks' law describes the flux, which corresponds to the particle flux density of a species. This flux is proportional to the gradient of the mass fraction:

$$\boldsymbol{J_i} = -\rho D \nabla \cdot y_i \tag{15}$$

The molecular diffusion coefficient *D* accounts for the mobility of the species particles, it depends on the species molar mass and on the pressure and temperature. The binary diffusion coefficient for two gaseous species *a* and *b* is described by the Chapman-Enskog theorem [24, 25]:

$$D = \frac{1.863 \cdot 10^{-3} \sqrt{T^3 (M_a^{-1} + M_b^{-1})}}{p \sigma_{ab}^2 \Omega_{ab}} \tag{16}$$

In the above equation, is $M_{a/b}$ the molar mass of the species *a* and *b*, respectively. The mean collision diameter is $\sigma_{ab} = (\sigma_a + \sigma_b)/2$ and Ω_{ab} is the collision integral, which depends on the temperature. The data for the collision diameter and integral are tabulated [25]. Alternatively, tabulated or parameterized diffusion coefficients can be used directly.

2.2. Chemical reactions and combustion

Chemical reactions lead to a change in the amount of substances in the mixture, where the number of atoms of each chemical element in the mixture is conserved. As an example, the Jones and Lindstedt [26] four-step mechanism for combustion of hydrocarbons is shown on the next side:

$$CH_4 + 0.5O_2 \rightarrow CO + 2H_2$$
$$CH_4 + H_2O \rightarrow CO + 3H_2$$
$$CO + H_2O \leftrightarrow CO_2 + H_2$$
$$H_2 + 0.5O_2 \leftrightarrow H_2O$$

The composition of a material depends on the temperature, the reaction progress, and the species concentrations. For a chemical reaction, balance equations are formulated for the species. An elementary reaction is described by Equation 17, where n is the number of species, the chemical symbol of an element i is X_i and ν_i' and ν_i'' are the stoichiometric coefficients for the educts and products, respectively.

$$\sum_{i=1}^{n} \nu_i' X_i \Leftrightarrow \sum_{i=1}^{n} \nu_i'' X_i \tag{17}$$

The reaction rate R_R is calculated from the mean species concentrations c_i and the reaction coefficients k_f and k_b for forward and backward reaction, respectively.

$$R_R = k_f \prod_{i=1}^{n} c_i^{\nu_i'} - k_b \prod_{i=1}^{n} c_i^{\nu_i''} \tag{18}$$

The reaction coefficients can be determined theoretically for simple elementary reactions by molecular kinetic equations. Due to their complexity, many reactions require experiments for the identification of proper reaction coefficients. The reaction coefficients for forward reactions are generally estimated by the empirical Arrhenius approach for the average temperature T:

$$k_f = A T^n e^{\left[-\frac{E_A}{RT}\right]} \tag{19}$$

The frequency factor A considers the number of molecule collisions per time, T^n describes the pre-exponential temperature dependency, E_A is the activation energy, and R the gas constant. The parameters for A, T^n and E_A are tabulated for many reactions in databases or publications. The reaction coefficient for the backward reaction k_b is calculated with the equilibrium constant K_c:

$$\frac{k_f}{k_b} = K_C \tag{20}$$

The equilibrium constant for an ideal gas depends on the temperature, the pressure and the change of the Gibb's potential $\Delta\mu_i{}^0$ of a species:

$$K_C = \exp\left[-\frac{\Delta\mu_i^0}{RT}\right] \frac{p}{RT}^{\Sigma_{i=1}^{n}(\nu_i' - \nu_i'')} \tag{21}$$

The formation velocity $\dot{r}_i$ for a species i during a chemical reaction can be calculated from the reaction rate R_R and the difference of the stoichiometric coefficients of educts and products. The produced specific amount of substance per time is:

$$\dot{r}_i = R_R(\nu_i' - \nu_i'') \tag{22}$$

For the species conservation (Equation 13 and 14), the production and consumption rate of the species have to be determined related to the mass. This rate is calculated as the product of the

sum of the formation velocities of all corresponding reactions N_R and the molar mass M_i of the species.

$$\dot{\omega}_i = M_i \sum_{\gamma=1}^{N_R} \dot{r}_{i,\gamma} \tag{23}$$

For the energy equation (Equations 9 and 10), the heat release $\dot{\omega}_h$ for the chemical reaction is needed, for which the formation enthalpy h_i^0 of the species has to be considered:

$$\dot{\omega}_h = \sum_{i=1}^{n} \dot{\omega}_i \frac{h_i^0}{M_i} \tag{24}$$

Combustion processes can be categorized (idealised) in premixed and non-premixed combustion processes. For premixed combustion processes, the fuel and the oxidiser are homogenously mixed before ignition. The present work focuses on non-premixed combustion, due to the fact, that for the investigated spray flame no complete mixing of fuel and oxidiser can be assumed. Due to the evaporation of individual fuel droplets, the mixture may be locally rich or lean and a homogenous mixture is quite unlikely.

The ratio of fuel and oxidiser during a combustion process can be described by a normalised conserved scalar, the mixture fraction *Z*. From the mixture fraction, the mass fractions of the educts and products, the temperature and the combustion progress can be derived. Hence, it is an important quantity for the investigation of combustion processes, especially for turbulent combustion simulations, which is described in detail in chapter 2.5. The mass fraction of a fuel in a mixture can be described by the mixture fraction Z:

$$Z = \frac{\dot{m}_F}{\dot{m}_O + \dot{m}_F} \tag{25}$$

In the equation above, $\dot{m}_F$ is the mass flow of the fuel and $\dot{m}_O$ the mass flow of the oxydiser, respectively.

The mixture fraction can vary between zero and unity; it is equal unity for pure fuel and equal zero for pure oxidiser. The mass fraction of fuel $y_{F,U}$ and oxidiser $y_{O,U}$ for the unburnt mixture can be calculated with the mixture fraction in the unburnt mixture and the fuel mass fraction in the fuel stream $y_{F,0}$ and the oxidiser mass fraction in the oxidiser stream $y_{F,0}$,:

$$\begin{aligned} y_{F,U} &= Z\, y_{F,0} \\ y_{O,U} &= (Z-1)\, y_{O,0} \end{aligned} \tag{26}$$

With the relation $sy_F - y_O = sy_{F,U} - y_{O,U}$ and the stoichiometric oxygen-fuel ratio $s = \nu_{O_2} M_{O2}/M_F$ with the stoichiometric reaction coefficient ν_{O_2} for oxygen and the molar mass for oxygen M_{O2} and fuel M_F the mixture fraction reads [27]:

$$Z = \frac{sy_F - y_{O2} + y_{O2,0}}{sy_{F,0} + y_{O2,0}} \tag{27}$$

Furthermore, Bilger [27] has introduced a definition for the mixture fraction of the products for the combustion of hydrocarbon fuels:

$$Z = \frac{2(y_C - y_{C,0})/M_C + (y_H - y_{H,0})/(2M_H) - (y_O - y_{O,0})/M_O}{2(y_{C,F} - y_{C,0})/M_C + (y_{H,F} - y_{H,0})/(2M_H) - (y_{O,F} - y_{O,0})/M_O} \quad (28)$$

The subscripts C, H and O in the equation above correspond to the elements carbon, hydrogen and oxygen, respectively.

2.3. Turbulence

One has to distinguish laminar and turbulent flow. Considered macroscopically, laminar (lat. laminar: layer, plate) flow consists of individual parallel layers that do not mix: a filament of paint injected into a laminar flow [28] only spreads minimally due to molecular diffusion. Turbulent flows (lat. turba = disturbance, confusion) are irregular three-dimensional, random, unsteady and dissipative. For turbulent flows, the above mentioned paint filament mixes rapidly directly after the injection with the flow due to turbulent diffusion, which is much stronger than molecular diffusion. The turbulent eddies within a turbulent flow can be imagined as local circulating motions with different turbulent length scales. These three-dimensional eddies enhance the transport processes within the flow and hence the mixing. This leads to an increase of transport and mixing of matter, momentum and heat in flows [29]. The rate of chemical reaction can also be enhanced by turbulence due to the faster and better mixing of reactants [30]. The formation and growth of nanoparticles in a gas-phase synthesis process depend on mixing processes and hence, are affected by turbulence. An increased rate of mixing can lead to larger formation rates with lower variance in particle size [31].

The range of the turbulent length scales is wide and turbulent kinetic energy is transferred from larger to smaller scales. At the smallest scales (Kolmogorov's microscales) the kinetic energy of the average velocity is finally dissipated into heat by the molecular viscosity. One property of turbulent flow is the increased dissipation compared to laminar flow.

The Reynolds number *Re* enables to estimate how turbulent a flow is - or if turbulent at all. It describes the ratio of inertia and viscosity forces and is defined by Equation 29.

$$Re = \frac{\rho u d}{\mu} \quad (29)$$

For the calculation of the Reynolds number, the characteristic length *l* or the characteristic diameter *d* of the body, which the flow surrounds or passes, is required. Relative to the respective flow problem, a critical Reynolds number Re_{krit} can be defined. From a Reynolds number of Re_{krit} small fluctuations cause disturbances within the flow field and turbulence develops: a transition from laminar to turbulent flow occurs. If $Re < Re_{krit}$ turbulent structure are not stable and perturbations are damped and dissipated. The transition from laminar to

turbulent is smooth and the values for the critical Reynolds number are therefore only approximate values.

For the calculation of the Reynolds number, of a pipe flow the inner diameter is the corresponding characteristic length and the cross section averaged velocity the characteristic velocity. The critical Reynolds number for a pipe flow is assumed to be $Re_{krit} \sim 2300$ [33]. Nevertheless, in experiments a laminar flow could be observed in a pipe also for Reynolds numbers larger than 50,000 if any perturbations were carefully avoided [34]. However, disturbances in this flow field would cause an irreversible transition to a turbulent flow.

2.3.1. Modelling

The solution of the three-dimensional Navier-Stokes equation can theoretically be realized by a direct numerical simulation (DNS) without any modelling. For a DNS, all turbulent eddies must be resolved and therefore, the grid resolution is dictated by the smallest turbulent scales, which are defined by the Kolmogorov length scale η_K. The size of the investigated domain and the Kolmogorov length scale determine the number of grid cells *n*. In one direction it is proportional to the 0.75^{th} power of the Reynolds number [29]: $n \sim L/\eta_K \sim Re^{3/4}$. Therefore, for a three-dimensional simulation, the number of grid cells is approximately $n \sim Re^{9/4}$. Due to this fine resolution, a DNS is restricted to small Reynolds Numbers and small computational domains. Therefore, for most applications, turbulence modelling is required. For the modelling of turbulence, there are two main approaches: the Large Eddy Simulation (LES), where large eddies are resolved and only small ones are modelled, and the solution of Reynolds averaged Navier-Stokes (RANS) equations, where all turbulent scales are modelled. LES represents a bridge between DNS and RANS and provides a good resolution of flow structures with low computational effort compared to a DNS. However, a LES simulation for real application still requires large computational resources, such as a cluster or even a supercomputer, and long computational times, whereas RANS simulations can often be performed on a small number of processors or even serially on a personal computer (PC) in a few days or even a few hours. To some degree, RANS modelling is also more „satisfying“ since all the relevant physics are involved in the (modelled) equations, and fully converged solutions can be achieved, which is normally not possible with LES. Therefore, for many technical applications, especially in industry, RANS simulations are still state-of-the-art.

Turbulence models do not describe the turbulent motion and behaviour itself, but only the effect of turbulence on the mean flow, on combustion, radiation, particle formation and transport and on other physical and chemical processes. The basis for the RANS approach is the Reynolds decomposition: an instantaneous quantity is split into a time, sample or phase averaged and a fluctuating part [35]. This decomposition is shown below for the velocity, pressure and the stress tensor:

$$\boldsymbol{u} = \overline{\boldsymbol{u}} + \boldsymbol{u}', \quad p = \bar{p} + p', \quad \boldsymbol{T} = \overline{\boldsymbol{T}} + \boldsymbol{T}' \tag{30}$$

Here, $\overline{\boldsymbol{u}}$ represents the time averaged part and $\boldsymbol{u}'$ the fluctuating part of $\boldsymbol{u}$ (and for p and $\boldsymbol{T}$, respectively). The definition for a time averaged quantity φ is:

$$\bar{\varphi} = \lim_{\tau\to\infty}\left(\frac{1}{\tau}\int_0^{\tau}\varphi(t)dt\right) \tag{31}$$

The time averaged fluctuating component is zero:

$$\bar{\varphi'} = \lim_{\tau\to\infty}\left(\frac{1}{\tau}\int_0^{\tau}\varphi'(t)dt\right) = 0 \tag{32}$$

The Navier-Stokes equations can be split into a mean and a fluctuating part. Here, density and viscosity are assumed to be constant without fluctuations. With the Reynolds decomposition (Equations 30), the mass conservation equation (Equation 3) and the momentum conservation equation (Equation 5) read (neglecting external forces):

$$\rho\nabla\cdot(\overline{\boldsymbol{u}} + \boldsymbol{u}') = 0 \tag{33}$$

$$\frac{\partial\rho(\overline{\boldsymbol{u}} + \boldsymbol{u}')}{\partial t} + \nabla\cdot(\rho(\overline{\boldsymbol{u}} + \boldsymbol{u}')(\overline{\boldsymbol{u}} + \boldsymbol{u}') + (\bar{p} + p')\boldsymbol{I} - (\overline{\boldsymbol{T}} + \boldsymbol{T}')) = 0 \tag{34}$$

Time-averaging of these equations yields:

$$\rho\overline{\nabla\cdot(\overline{\boldsymbol{u}} + \boldsymbol{u}')} = 0 \tag{35}$$

$$\overline{\frac{\partial\rho(\overline{\boldsymbol{u}} + \boldsymbol{u}')}{\partial t}} + \overline{\nabla\cdot\rho(\overline{\boldsymbol{u}} + \boldsymbol{u}')(\overline{\boldsymbol{u}} + \boldsymbol{u}')} + \overline{\nabla\cdot(\bar{p} + p')\boldsymbol{I}} - \overline{\nabla\cdot(\overline{\boldsymbol{T}} + \boldsymbol{T}')} = 0 \tag{36}$$

With the averaging identities shown below, the Reynolds averaged momentum equation for an incompressible flow is expressed by Equation 37.

$\bar{\bar{a}} = \bar{a}$,

$\overline{a + b} = \bar{a} + \bar{b}$,

$\overline{\bar{a}\bar{b}} = \bar{a}\,\bar{b}$,

$\overline{(\bar{a})^2} = (\bar{a})^2$,

$\overline{\bar{a}a'} = 0$,

$\overline{ab} = \bar{a}\,\bar{b} + \overline{a'b'}$,

$\overline{a^2} = (\bar{a})^2 + \overline{(a')^2}$,

$\frac{\partial\bar{a}}{\partial t} = \frac{\overline{\partial a}}{\partial t} = 0$,

$\frac{\partial\bar{a}}{\partial x} = \frac{\overline{\partial a}}{\partial x}$

$$\rho\left(\frac{\partial\overline{\boldsymbol{u}}}{\partial t} + \nabla\cdot\overline{\boldsymbol{u}\boldsymbol{u}}\right) + \nabla\cdot\bar{p}\boldsymbol{I} = \nabla\cdot(\mu(\nabla\overline{\boldsymbol{u}} + (\nabla\overline{\boldsymbol{u}})^{\boldsymbol{T}}) - \rho\overline{\boldsymbol{u}'\boldsymbol{u}'}) \tag{37}$$

With this averaging, a stress tensor $\boldsymbol{R} = -\rho\overline{\boldsymbol{u}'\boldsymbol{u}'}$ remains, which results from the turbulent fluctuations. This tensor is called Reynolds stress tensor. The Reynolds stress tensor is a symmetrical tensor and incorporates six independent stress components. Therefore, six additional relations are needed, which have to be solved by appropriate turbulence models, leading to a closure problem for the RANS equations. One elaborate concept for this closure

represent the Reynolds Stress Models (RSM), which solve a transport equation for each of the six unknown turbulent stresses plus one for the dissipation rate. The method of closure for the RSM is called Second Moment Closure and was proposed by Launder et al. [36] in 1975. The RSMs models are computationally expensive and are normally only applied for flow featuring anisotropic turbulence.

Another approach is the introduction of a linear relation between the Reynolds stress tensor and the mean velocity gradients, which is known as the Boussinesq or eddy viscosity approximation:

$$\boldsymbol{R} = -\rho\overline{\boldsymbol{u}'\boldsymbol{u}'} = \mu_T\overline{\boldsymbol{S}} - \frac{2}{3}\rho k\boldsymbol{I} \tag{38}$$

In contrast to the molecular viscosity μ, the turbulent eddy viscosity μ_T is not a characteristic of the fluid, but it is a flow field property. It describes the apparent viscosity increase due to turbulent fluctuations. The Reynolds averaged strain rate tensor $\overline{\boldsymbol{S}} = (\nabla\overline{\boldsymbol{u}} + (\nabla\overline{\boldsymbol{u}})^{\boldsymbol{T}})$ can be derived in analogy to the strain rate tensor for the viscous stresses of a Newtonian fluid. The square root of the turbulent kinetic energy $k = 1/2\,\overline{\boldsymbol{u}' \cdot \boldsymbol{u}'}$ represents the velocity fluctuations due to turbulence. The Boussinesq approximation reduces the RANS closure problem from a lack of six equations for the stress tensor to only one missing equation for the turbulent eddy viscosity. Hence, the advantage of this model is the low computational cost. The turbulence models, which rely on the Boussinesq approximation, can be distinguished due to the number of independent variables, respectively equations, which are used for the calculation of the turbulent viscosity. The most common approaches are the two-equation models, for which two coupled transport equations are solved. The two main groups of these models are the k-ω and the k-ε model. For both groups, two partial differential equations are introduced, where one equation describes the transport of the turbulent kinetic energy *k*. The k-ω model additionally solves a partial differential equation for the characteristic frequency ω of the energy dissipating eddies and the k-ε model for the isotropic dissipation rate ε. In the present work, a k-ε model is used and therefore, further focus is on this model.

One of the most commonly used turbulence models is the **k-ε model**. There are different formulations of the k-ε model, where the model of Jones and Launder [37] and Launder and Sharma [38] are known as the standard k-ε model. For simplicity, the equations below are shown for a constant density flow.

The conversion of Equation 37 by implementing Equation 38 with the kinematic viscosity $\nu = \mu/\rho$ and neglecting additional volume forces leads to (all quantities are Reynolds averaged):

$$\frac{\partial\overline{\boldsymbol{u}}}{\partial t} + \nabla\cdot\overline{\boldsymbol{u}\boldsymbol{u}} = -\nabla\cdot p\overline{\boldsymbol{I}} + \nabla\cdot[(\nu+\nu_T)(\nabla\overline{\boldsymbol{u}} + (\nabla\overline{\boldsymbol{u}})^{\boldsymbol{T}})] \tag{39}$$

For the standard k-ε model, the turbulent kinematic viscosity can be expressed as $\nu_T = C_\mu k^2/\varepsilon$ with a model constant C_μ. Two transport equations are introduced for k and ε, respectively, from which the turbulent viscosity can finally be calculated:

$$\frac{\partial k}{\partial t} + \nabla \cdot k\overline{\boldsymbol{u}} = \nabla \cdot \left(\nu + \frac{\nu_T}{\sigma_k}\nabla k\right) + P_k - \varepsilon \tag{40}$$

$$\frac{\partial \varepsilon}{\partial t} + \nabla \cdot \varepsilon\overline{\boldsymbol{u}} = \nabla \cdot \left(\nu + \frac{\nu_T}{\sigma_\varepsilon}\nabla \varepsilon\right) + \frac{\varepsilon}{k}(C_1 P_k - C_2\varepsilon) \tag{41}$$

In both equations on the RHS $P_k = 1/2\nu_T[\nabla\overline{\boldsymbol{u}} + (\nabla\overline{\boldsymbol{u}})^{\boldsymbol{T}}]^2 = 1/2\nu_T\overline{\boldsymbol{S}}^2$ describes the production and $\boldsymbol{\varepsilon}$ the dissipation of turbulent kinetic energy. The model constant in these two equations are C_μ = 0.09, C_1 = 1.44, C_2 = 1.92, σ_k = 1.0 and σ_ε = 1.3 [39].

The **Re-Normalisation group (RNG) k-ε model** was developed by Yakhot et al. [40] using a statistical approach; the renormalisation group theory. As the standard k-ε model only accounts for a single turbulent length scale, the RNG k-ε model considers different scales of turbulent motion. The RNG k-ε model considers low-Reynolds number effects by applying a differential formula for the effective viscosity. This formula was analytically derived and comes as an additional production term $\varepsilon^2 C_3/k$ in the transport equation for ε.

$$\frac{\partial \varepsilon}{\partial t} + \nabla \cdot \varepsilon\overline{\boldsymbol{u}} = \nabla \cdot \left(\nu + \frac{\nu_T}{\sigma_\varepsilon}\nabla \varepsilon\right) + \frac{\varepsilon}{k}(C_1 P_k - C_2\varepsilon + C_3\varepsilon) \tag{42}$$

The model constants for the above equation are C_μ = 0.0845, C_1 = 1.42, C_2 = 1.68, σ_k = 0.7194 and σ_ε = 0.7194 [40]. The additional model parameter C_3 is calculated with $\eta = k/\varepsilon\sqrt{\mathrm{P_k}}$, β = 0.012 and η_0 = 4.38 [40]:

$$C_3 = \frac{C_\mu \eta^3(1 - \eta/\eta_0)}{1 + \beta\eta^3} \tag{43}$$

In many cases, two-equation models are advantageous due to the low computational cost and their good performance. However, some applications require the use of more complex turbulence models such as the RSM. These are mostly cases where the anisotropy of the turbulence is dominating (e.g. swirling flows), as the Boussinesq concepts only assume isotropic turbulence (introducing a turbulent viscosity). Nevertheless, the isotropic assumption works for most technical cases, for example for jet flows as shown in this thesis.

2.4. Spray processes

A spray is a multiphase flow with dispersed droplets in a gas. The spray forming process is called atomization. Sprays can be formed by naturally occurring processes such as sea spray that arises from crashing ocean waves or high winds. However, most sprays are produced with spray nozzles. Spray processes are used for many applications, commonly for the

distribution of a liquid onto a surface or into a chamber to support evaporation and improve mixing of the two phases for subsequent combustion. Spray assisted processes are used for surface coating, in gas turbines, Diesel engines or for the nanoparticle spray flame process investigated in this thesis.

Liquid jets break up and form a spray due to disturbances, which result from deformations of the liquid-gas interface, pressure or velocity fluctuations, or fluctuations in the liquid properties [41, 42]. Experiments have shown how the destabilization of the liquid jet evolves: waves are formed on the liquid interface due to shear instabilities. The liquid is locally accelerated and Rayleigh-Taylor instabilities at the wave crests lead to a formation of ligaments, which are stretched in the gas stream and break into droplets as outlined by Marmottant and Villermaux [43]. The size of the droplets, the separation frequency, the spray angle and the break-up height depend on many parameters such as the velocity of the gas and liquid phase, the pressure and the material properties (surface tension). The first studies on liquid jet break-up were done by Rayleigh in 1879 [44] for a simplified test case, where he neglected the ambient fluid and the influences of the liquid viscosity. In 1931, Weber [45] was the first who considered the effect of the liquid viscosity and the ambient pressure. Another pioneering work was performed by Taylor in 1962 [46], who investigated the role of the ambient gas density on the droplet diameters. There have been many further studies on liquid jet break-up [46], which deliver linear theories for a qualitative description of the break-up phenomena and the main break-up regimes. However, a quantitative prediction of the spray properties by analytical calculations is only possible for simple laminar test cases. For most applications, an analytical calculation of the spray properties is still not possible due to the large number of parameters such as turbulence, internal flow effects within the nozzle, the thermodynamic states of gas and liquid phase and the real jet velocity profile, which cannot be covered by the linear stability theory.

For the modelling and simulation of a multiphase flow containing spray droplets, the determination of appropriate spray boundary conditions is important and quite challenging. Therefore, experiments or detailed simulations of the primary jet break-up process are needed. The underlying modelling approaches for multiphase flows are described in the following section.

The spray modelling in this work is performed in two consecutive steps: firstly, the primary break-up is calculated with a Volume of Fluid method (VOF) and subsequently, the evolution of the developed spray droplets is described by a Lagrangian particle method. The coupling occurs by determining the statistics of the droplets by the VOF simulations, and setting these as inlet boundary conditions for the Lagrangian particle calculations.

2.4.1. Volume of Fluid method

A common method to model a segregated two-phase flow is the Volume of Fluid method [48]. Although it is not applicable to model certain interface phenomena, it is often used for free surface applications. It is commonly applied to determine break-up and recombination processes. The VOF method is based on an Eulerian approach, where an additional transport equation for the fraction function *C* is introduced. The afore-mentioned function describes the volume fraction of a fluid phase within a cell: *C* equal zero means, none of the traced fluid is in the cell and *C* equal unity, that the cell is full of the fluid. A value of *C* between zero and unity implies a free fluid surface within the cell. In each computational cell, the volume fractions of all phases sum to unity. The transport equation considers the convective transport of *C* due to the velocity field (second term on the LHS) and the mass exchange between the phases (term on the RHS) as outlined in Equation 44:

$$\frac{\partial C}{\partial t} + \nabla \cdot (\boldsymbol{u}C) = \sum_{i=1}^{n} \left(\dot{m}_{ij} - \dot{m}_{ji}\right) \tag{44}$$

In the above equation, *n* is the number of phases, $\dot{m}_{ij}$ is the mass transfer from phase *i* to phase *j* and $\dot{m}_{ji}$ the mass transfer from phase *j* to phase *i*, respectively. This mass transfer may be due to evaporation, condensation or other processes.

Within the VOF method the volume is a conserved quantity. A single set of transport equations for mass, momentum and energy is solved, which is shared by all phases. The average thermophysical properties, such as density or viscosity, are determined by the phase distribution of *C*. These values are then used to correct the predicted velocity field. A well-known problem of the shared fields is that in cases, where large velocity and temperature differences occur between the different phases, the accuracy of the corresponding value near the phase interface can be disadvantageously affected. The value of the volume fraction is stored at the centre of each computational cell. Therefore, the flux of *C* across the cell faces has to be determined and hence, which phase or, which mixture of phases crosses the cell faces. There are different approaches to reconstruct the phase interface (piecewise constant, piecewise linear or stair stepped approximation), where the piecewise linear interface calculation (PLIC) [49] is the most common one. In this method, the phase interface represents a plane for a three-dimensional case. The plane is calculated by a piecewise linear reconstruction for each cell. For interface grid cells, meaning where $0 < C < 1$, the normal vector $\boldsymbol{n_\gamma}$ of the plane is calculated by the gradient of *C* at the cell centre $\boldsymbol{x_c}$ [49]:

$$\boldsymbol{n_\gamma} = \frac{-\nabla C(\boldsymbol{x_c})}{\|\nabla C(\boldsymbol{x_c})\|} \tag{45}$$

The position of the interface is determined with the variable *C*: the volume fraction of the cell enclosed by the cell boundaries and the plane is equal the volume fraction *C*. The volume between the phase interfaces is closed over all cells [50] and describes a polygon. The schematic of the PLIC method is illustrated in Figure 2-1.

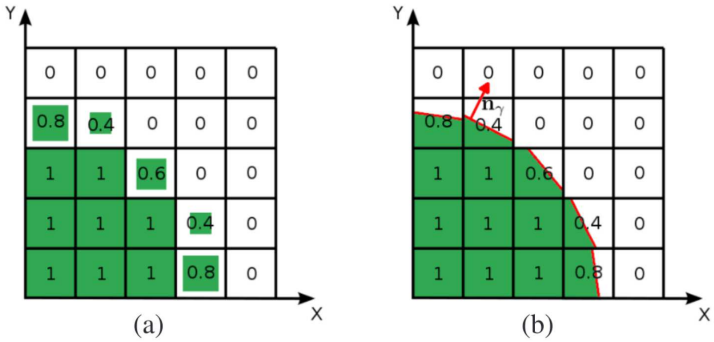

Figure 2-1: PLIC interface reconstruction: a) information for the volume fraction *C* is stored at the cell centres, b) interface reconstruction by determination of the plane normal $\boldsymbol{n_\gamma}$, taken from the publication of Karch et al. [50].

For the VOF simulation performed in this work, a two-fluid (gas and liquid) formulation is applied. To control numerical diffusion, an additional convective term (the compression term) is introduced for the transport equation for *C* [51] by calculating the velocity as the weight averaged velocity of the two phases as given by the third term on the LHS in Equation 46:

$$\frac{\partial C}{\partial t} + \nabla \cdot (\boldsymbol{u}C) + \nabla \cdot (\boldsymbol{u_r} C(1-C)) = 0 \tag{46}$$

The relative velocity $\boldsymbol{u_r} = \min(c_\alpha|\boldsymbol{u}|,\ \max|\boldsymbol{u}|)\boldsymbol{n_\gamma}$ is the velocity of the free surface with the compression coefficient c_α . The compression term aims to steepen the gradient of the volume fraction function and therefore sharpens the interface resolution. It vanishes in the region, where only a single fluid is located (*C = 1* or *C = 0*). Theoretically, the free surface is infinitesimal thin and hence the relative velocity tends to zero and Equation 46 becomes the conventional Equation 44.

For a VOF simulation, the effect of surface tension at the interface between the different phases can also be determined. For example at a bubble surface the net force is radially inward, which increases the pressure on the bubble and contracts its surface. Due to the surface tension, the bubble does not collapse: the surface tension balances the radially inward forces and the outward pressure gradient force. The force due to surface tension is calculated as follows [52] with the surface tension coefficient σ_s:

$$\boldsymbol{F_{ST}} = \int_V \sigma_s \boldsymbol{n_\gamma} \nabla C \, dV \tag{47}$$

This force is considered as an additional term in the momentum equation. The importance of the surface tension can be determined by the Weber number *We* for *Re* >> 1 and by the

capillary number *Ca* for *Re* << 1. The Weber number is defined as the ratio of inertia force and surface tension.

$$We = \rho_g \boldsymbol{U}^2 l/\sigma_s \tag{48}$$

The characteristic length *l* corresponds to the characteristic interface length, as for example to the diameter of a droplet, and the velocity to the relative velocity of the two phases.

The capillary number is the ratio of viscous forces and surface tension and defined as follows:

$$Ca = \mu \boldsymbol{U}/\sigma_s \tag{49}$$

The surface tension can be neglected when *Ca* or *We* >> 1 [53].

For a high curvature surface and dominant surface tensions, as for example for very slow bubbles or droplets with a diameter smaller or equal 1 µm, numerical problems might occur: for these cases, two terms become very large in the momentum equation, which are the pressure and the surface tension force term. All other terms tend to zero for a nearly steady bubble or droplet. These two forces have to balance each other. The pressure force depends on the gradient of the pressure and the surface tension force on the gradient of the volume fraction (Equation 47). As the curvature $\boldsymbol{n_\gamma}$ also depends on the gradient of the volume fraction (Equation 45), a balance of the two terms can hardly be achieved, especially for an arbitrary grid [54]. These stress imbalances at the interface cause spurious or parasitic currents, which are vortical flows, which might affect the interface shape and provide unphysical results. This problem has to be considered for the discretisation [54, 55].

Additionally, when using the VOF method, higher order discretisation schemes should be used, as low-order discretisation schemes for the solution of the convective term can introduce artificial mixing of the phases and smear the phase interface. Local grid refinement is important for an accurate resolution of free surfaces, as the free surface cannot be sharply defined and is smeared over one to three cells [54].

A DNS of a **primary break-up** process provides a promising tool to investigate the dense region of a spray. Unfortunately, when the VOF method is applied, uncertainties in the interface description and hence the surface tension can occur, as already described above. Therefore, different approaches for the interface reconstruction are commonly combined with the VOF method. Sussman et al. [56] have combined a level set [57] and a VOF method, denoted as combined level set Volume of Fluid (CLSVOF) approach, to benefit from both strategies. The level set method provides an accurate and smooth reconstruction of the interface, but would (standalone) cause mass losses at regions, where the computational mesh is not resolved properly. The combination of the level set and the VOF technique features an accurate interface reconstruction with the good mass conservation property of the VOF approach.

Menard et al. [58] have further enhanced the CLSVOF approach [56]. They combined a VOF method with a level set and a ghost fluid method (GFM) [59] to benefit from the advantages of all three strategies. They used the level set method for interface tracking and the GFM to capture sharp discontinuities for pressure, density and velocity. The combination of these three approaches was applied and validated for the three-dimensional modelling of a primary break-up of a liquid jet. The new technique reduces the parasitic currents and avoids the artificial smoothing that normally occurs for a VOF calculation.

Li et al. [60] have coupled the CLSVOF formulation with the Lagrangian tracking of the spray on a dynamically adaptive, block-structured grid. This adaptive technique selectively features high grid densities at the liquid interface, which increases the accuracy of the prediction of the primary break-up. For this approach, small liquid structures, which are formed by atomization, are transformed from the Eulerian description into Lagrangian particle. Hence, for this method, no mesh refinement is required in the dilute spray region.

2.4.2. Lagrangian particle method

The Lagrangian particle method is used for dispersed multiphase flows. In the present work, it is therefore applied where primary break-up is assumed to be completed and spray droplets are dispersed in the gas flow. In this method, the Lagrangian particles are material particles, which underlie Newton's law of motion. In comparison to the Eulerian approach, no fixed control volume is observed in the Lagrangian framework, instead, the observer follows a Lagrangian particle in time and space. For the Lagrangian particle method, an initial particle diameter distribution and mean particle velocity (including the spreading angle) are required. However, better descriptions would be possible considering their correlation and more detailed descriptions of the joint particle velocity-size distribution function.

Commonly, a Lagrangian particle represents a parcel, which comprises a certain number of real liquid droplets. The Lagrangian particle position $\boldsymbol{X(t)}$ and its velocity $\boldsymbol{U(t)}$ are calculated from the local Eulerian field and a dispersion rate. The Lagrangian particle is affected by the Eulerian field due to the drag force. Additionally, other external forces may act on the particles, such as buoyancy or electromagnetic forces. The resulting equation for the particle velocity (neglecting external forces) reads:

$$\frac{d\boldsymbol{U}}{dt} = \boldsymbol{F_d} \tag{50}$$

In this equation, $\boldsymbol{F_d}$ is the drag force, which is calculated according to Equation 51 with the relative velocity between the particles (Lagrangian phase) and the gas phase (Eulerian field) $\boldsymbol{U_{rel}} = \boldsymbol{u} - \boldsymbol{U}$.

$$\boldsymbol{F_d} = \frac{18\mu_g}{\rho_l d_l^2}\frac{C_d Re}{24}\boldsymbol{U_{rel}} \tag{51}$$

Here, μ_g is the dynamic viscosity of the gas, d_l the Lagrangian particle diameter, ρ_l the particle density (l for liquid), C_d the drag coefficient and Re the relative Reynolds number with the gas density ρ_g:

$$Re = \frac{\rho_g d_l |\mathbf{U_{rel}}|}{\mu_g} \tag{52}$$

For Low-Mach number flows, the drag coefficient is constant or can be calculated as a function of the Reynolds number. For a spherical object, the drag can be calculated as follows [61]:

$$C_{d,sphere} = \begin{cases} 0.424 & \text{for Re} > 1000 \\ \frac{24}{Re}\left(1 + \frac{1}{6}Re^{2/3}\right) & \text{for Re} \leq 1000 \end{cases} \tag{53}$$

Combining Equations 50 and 51, the equation for the particle velocity reads:

$$\frac{d\boldsymbol{U}}{dt} = \frac{3}{4}\frac{C_d}{d_l}\frac{\rho_g}{\rho_l}|\boldsymbol{U_{rel}}|^2 \tag{54}$$

The change of the position of a Lagrangian particle is determined by its velocity:

$$\frac{d\boldsymbol{X}}{dt} - \boldsymbol{U}(t) = 0 \tag{55}$$

The influence of turbulence on Lagrangian particle trajectories is captured by a random walk model. In this work, a discrete random-walk (DRW) dispersion model is used, which imposes a velocity in random direction on the particles for the turbulent time scale $\tau_t = k/\varepsilon$. This causes a deflection of the particles from their trajectories. The random motion is calculated from a Gauß distribution with the variance $\sigma = \sqrt{2/3\,k}$ [62]. This variance corresponds to the standard deviation of the velocity squared. Therefore, the velocity fluctuation is $u_i' = \zeta_i\sqrt{2/3\,k}$ with the Gaussian random variable ζ, with its mean being zero and the standard deviation of unity.

Due to high relative velocities (between the droplets and the gas phase) and due to turbulence, the droplets or ligaments can break up into smaller droplets, denoted as secondary break-up process. A criterion for a break-up of a droplet is the Weber number (Equation 48).

The Ohnesorg number considers the effect of viscosity on the break-up. It is defined as the ratio of the viscous force and the surface tension force with the liquid viscosity μ_l:

$$Oh = \mu_l/\sqrt{\rho_l d_l \sigma_s} \tag{56}$$

The secondary break-up model used in this work is the Pilch-Erdman model [63]. This model distinguishes between six different break-up mechanisms, depending on the Weber number. These break-up mechanisms are illustrated in Figure 2-2.

Each mechanism has its dimensionless break-up time t_{bu}. The characteristic break-up time τ_{bu} is calculated from t_{bu}:

$$\tau_{bu} = t_{bu} \frac{d_l}{|\boldsymbol{U_{rel}}|} \sqrt{\frac{\rho_l}{\rho_g}} \tag{57}$$

The dimensionless break-up time is determined according to Equation 58. The vibrational break-up mode, for We ≤ 12, represents the primary break-up and hence is not modelled.

$$t_{bu} = \begin{cases} 6(We-12)^{-0.25} & \text{for } 12 \le We \le 50 \\ 2.45(We-12)^{0.25} & \text{for } 50 \le We \le 100 \\ 14.1(We-12)^{-0.25} & \text{for } 100 \le We \le 350 \\ 0.766(We-12)^{0.25} & \text{for } 350 \le We \le 2670 \\ 5.5 & \text{for } We \ge 2670 \end{cases} \tag{58}$$

The stable droplet diameter can be calculated from the critical Weber number $We_{crit} = 12(1 + 1.077Oh^{1.6})$ according to Equation 59 when $We \geq We_{crit}$.

$$d_{l,st} = We_{crit} \frac{\sigma_s}{\rho_g |\boldsymbol{U_{rel}}|^2} \tag{59}$$

In this thesis, two-way coupling between the Eulerian and the Lagrangian phase is considered, due to the fact that the spray and the gas-phase interact by exchange of mass, momentum and heat, respectively. The interphase heat transfer is described by the model by Ranz and Marshall [64]. The Ranz-Marshall model is a well-tested correlation based on boundary layer theory. The heat transfer at a surface can be determined by the Nusselt number, which is the ratio of the convective and the conductive heat transfer normal to the surface. For a droplet, the Nusselt number reads $Nu = \alpha d_l/\lambda$ with the thermal conductivity λ and the convective heat transfer coefficient α.

The Ranz-Marshall approach introduces an additional expression of the Nusselt number as a function of the Reynolds and Prandtl number:

$$Nu = 2 + 0.6Re^{0.5}Pr^{0.33} \tag{60}$$

The Prandtl number $Pr = c_p\mu_l/\lambda$ only depends on the fluid and the state; it is defined as the ratio of the viscous to thermal diffusion rate with the viscosity μ_l of the liquid phase and the specific heat capacity c_p.

The phase change from liquid to gaseous due to evaporation is determined with an expression given by Baumgartner [65]. The corresponding evaporated mass $\dot{m}_{evap}$ is calculated according to Equation 61:

$$\dot{m}_{evap} = \pi\, d_l\, Sh\, D_v \rho_s ln\left(1 + \frac{x_s - x_c}{1 - x_s}\right) \tag{61}$$

In the previous equation x_s is molar fraction for the liquid phase at the droplet surface (determined by Raoult's law), x_c the molar fraction for the liquid phase in the surrounding field, D_v the vapor diffusivity, ρ_s the vapor density at the droplet surface and $Sh = k_m d_l / D_v$ the Sherwood number with the mass transfer coefficient k_m.

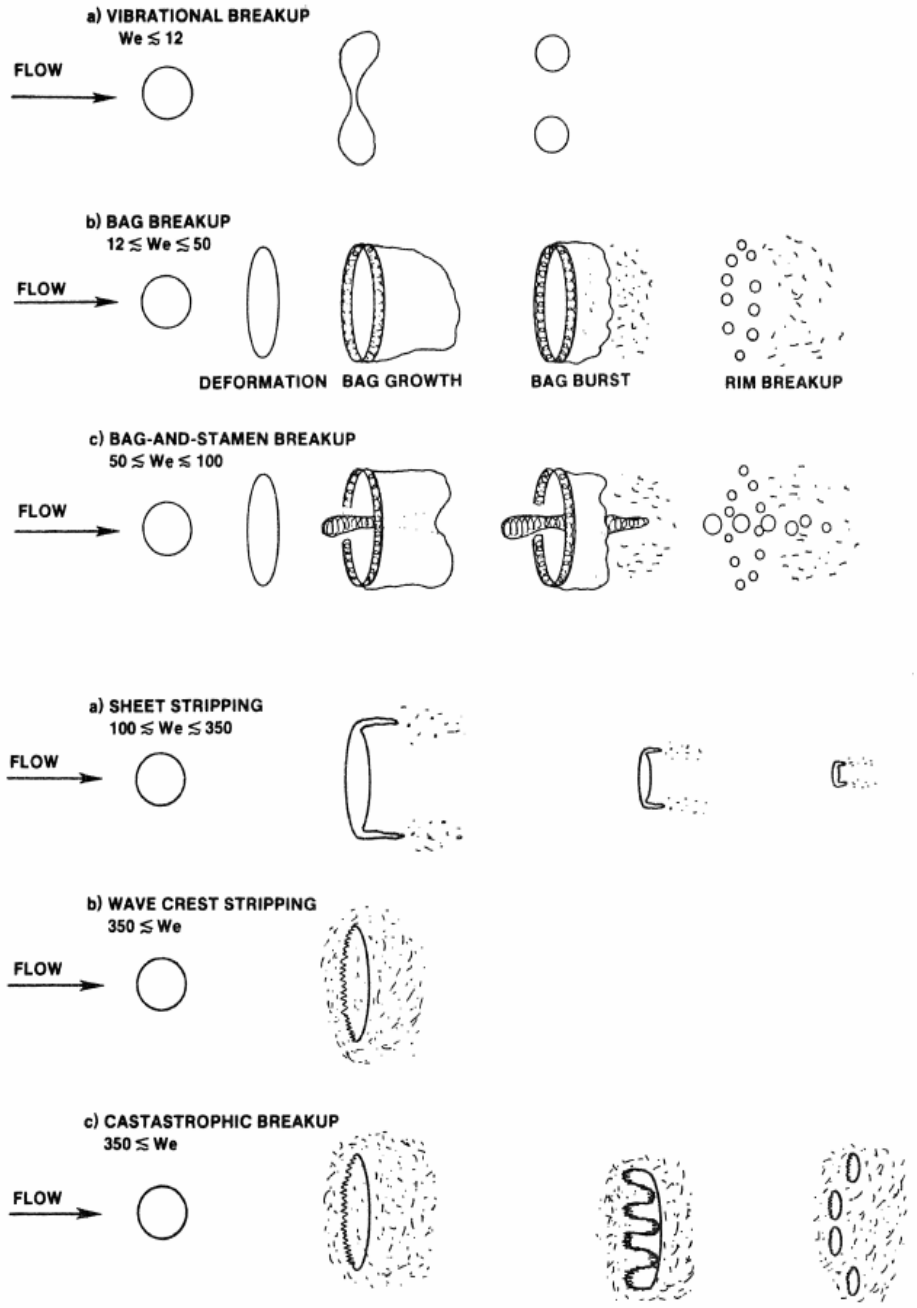

Figure 2-2: Droplet break-up modes, taken from the publication of Pilch et al. [63].

2.5. Turbulence chemistry interaction and its modelling

Chemical reactions can only occur when the reactants mix on a molecular level. Turbulence enhances the molecular diffusion by stretching the mixing layer and by keeping it locally thin it greatly increases the diffusive fluxes in mean gradient direction and hence the molecular mixing itself. The main objective of turbulent non-premixed combustion theory is therefore to understand how the turbulent motion affects the mixing and hence the chemical reaction rate [30].

As already mentioned in chapter 2.2, combustion processes can be categorized in premixed and non-premixed. For turbulent combustion processes, further classification considers the ratio of turbulent times scale τ_T and chemical time scale τ_C, defined by the Damköhler number $Da = \tau_T/\tau_C$ [66]. For small Damköhler numbers ($Da < 1$), the reaction process is relatively slow compared to the turbulent transport. For large Damköhler numbers ($Da > 1$), vice versa, the reaction progress is fast compared to the turbulent transport, normally at high temperature. Most turbulent combustion processes involve fast chemistry, where the chemical time scale is so small that chemical kinetics do not limit the reaction rate, fuel conversion rate, or heat release rate. The reaction heat release depends on the interaction between chemistry and turbulence. For $Da >> 1$, the chemistry can be assumed to be infinitely fast.

In turbulent flows, the reaction rate R_R is a non-linear function of the pseudo random variables temperature and species concentration. Therefore, it cannot be calculated from the mean temperature and mean species concentration (Equation 18) directly, as R_R is a non-linear function: the mean of the epression $\overline{R_R(T,c)}$ is not equal the result calculated from the mean variables: $\overline{R_R(T,c)} \neq R_R(\bar{T},\bar{c})$.

Hence, there is no straightforward way for the closure of the non-linear source terms and appropriate models are needed to calculate the temperature and species concentrations. For non-premixed combustion and infinitely fast chemistry ($Da >> 1$), it can be assumed that the combustion progress is dominated and limited by mixing (as mentioned above) [67]. Therefore, the mixture fraction Z, can be used to describe the composition of the mixture, the instantaneous temperatures, and the material mass fractions that evolve from the reacting fuel stream [68]. Due to the randomness of turbulence (chapter 2.3), the mixture fraction has random fluctuations at a certain point and time in turbulent flows. Therefore, the mixture fraction must be treated as random variable with statistical distribution. For a continuous random variable, a probability density function (PDF) can be defined, which describes the probability P for the random variable φ to have a certain value in the sample space Ω. The integral of a PDF is always unity and the PDF is everywhere nonnegative. A PDF contains the entire information of the statistical distribution of a continuous random variable. Hence, a turbulent variable at a given point and time is fully described by its PDF. The mean of the variable φ can be calculated as followed:

$$\bar{\varphi} = \int_{-\infty}^{+\infty} \varphi P(\varphi) d\varphi \tag{62}$$

The variance, the second moment of φ, is calculated based on the squared deviation from the mean value:

$$\overline{\varphi'^2} = \int_{-\infty}^{+\infty} (\varphi - \bar{\varphi})^2 P(\varphi) d\varphi \tag{63}$$

As the mean of a dependent variable $\theta = f(\varphi)$ cannot be calculated directly from the mean of the independent variable, the mean is derived by the PDF with $P(\varphi)d\varphi = P(\theta)d\theta$ and $d\theta = f(d\varphi)$:

$$\bar{\theta} = \int_{-\infty}^{+\infty} \theta P(\theta) d\theta = \int_{-\infty}^{+\infty} \theta(\varphi) P(\varphi) d\varphi \tag{64}$$

A good approach for the solution of the closure problem for the reaction source term are PDF models [70-72] to determine the random values of a turbulent flow from the mixture fraction. Common PDF methods are introduced in the following section.

2.5.1. PDF methods

PDF methods have been published by many authors [73-75] and are commonly used for the closure of the reaction source term for the modelling of turbulent reacting flows in the gas-phase. In this thesis, a PDF method is used to solve the interaction of turbulence and particle dynamics. A detailed overview of the variety of approaches is given by Pope [71] and Haworth [76].

For a turbulent gaseous reactive mixture, the fluid state can be determined by the velocity $\boldsymbol{u}$, the pressure p, the specific enthalpy h, and the species mass fractions y_i. The mass fractions and the enthalpy can be combined in a set of scalars $\boldsymbol{\psi} = \psi_1 .... \psi_n$, with $\psi_i = y_i$ (i = 1... n - 1) and $\psi_n = h$, for n - *1* species. Some methods additionally include $\boldsymbol{u}$ and p in this vector. Methods that do not involve $\boldsymbol{u}$ and p are normally called hybrid methods. A conservation equation for the scalar vector can be determined according to Equation 65.

$$\frac{\partial \rho \boldsymbol{\psi}}{\partial t} + \nabla \cdot (\rho \boldsymbol{\psi u} + \boldsymbol{J}) = \rho \boldsymbol{S} \tag{65}$$

In the above equation, $\boldsymbol{J}$ is the diffusive flux of $\boldsymbol{\psi}$ and S is the rate of creation of $\boldsymbol{\psi}$.

For this scalar vector, a PDF has to be determined to solve the random evolution due to turbulence, denoted as composition PDF.

The PDF methods can be divided in two categories, the presumed and the transported PDF method: For a presumed PDF method a particular shape is assumed for each scalar PDF, which is parameterized by its moments, which are further solved by transport equations [77] or by algebraic models (typically in LES). These moments are usually the mean value of the

scalar (first moment) and the variance, respective co-variance (second moment). Quite often, a PDF is formulated for the mixture fraction and a flamelet model is used for the calculation of the thermochemical quantities, such as temperature, density, viscosity and species mass fractions [78-80]. An example for a common presumed PDF is the β-PDF [81], which provides a qualitative good representation of monomodal and bimodal PDF shapes for a wide scale of variances [82]. The PDF follows a β-function B for a scalar variable as defined by Equation 66.

$$B(\alpha,\beta) = \int_0^1 t^{\alpha-1}(1-t)^{\beta-1}dt \tag{66}$$

For the mixture fraction Z ($0 \leq Z \leq 1$), the β-PDF is introduced by Equation 67 [83]:

$$f(Z,\alpha,\beta) = \frac{Z^{\alpha-1}(1-Z)^{\beta-1}}{B(\alpha,\ \beta)} \tag{67}$$

The PDF is parameterised by its moments α and β, which are the shape parameters for the β-function. The shape parameters α and β are a function of the Reynolds averaged mixture fraction $\bar{Z}$ and its variance $\bar{Z}''^2$ and are calculated according to equations 68 and 69 [83]:

$$\alpha = \bar{Z}\left(\frac{\bar{Z}(1-\overline{Z})}{\bar{Z}''^2} - 1\right) \tag{68}$$

$$\beta = (1-\bar{Z})\left(\frac{\bar{Z}(1-\overline{Z})}{\bar{Z}''^2} - 1\right) \tag{69}$$

It is often difficult or even impossible to guess a realistic shape of the PDF of the scalars, especially for the joint PDF, which is usually not the product of the marginal PDFs. The method of a presumed PDF can therefore be inaccurate. A more accurate, but a more CPU intensive method [84] is to calculate the joint PDF of the scalars directly from its transport equation. This modelling approach is known as the composition joint PDF or the transported PDF method [71]. The first model of a transported PDF was derived by Lundgren in 1967 as he used a transport equation for the joint PDF of the scalars and the velocity [85, 86]. A model equation for the PDF for a set of scalars was developed by Dopazo and O'Brien in 1974 [87]. They used a composition joint PDF to describe the thermo-chemical state of a turbulent reacting flow.

For a complete description of a fluid state, a PDF is needed for all scalar values at all temporal and spatial positions, resulting in an infinite-dimensional functional equation [70]. Therefore, one-point multivariate PDF methods are commonly used. The joint PDF of the scalars is defined as $f(\boldsymbol{\psi};\ \boldsymbol{x},\ t)$, which considers the random variables at a given location $\boldsymbol{x}$ and time t in the scalar space ($\boldsymbol{\psi}$-space) [71] and is denoted as composition PDF. The scalar space ($\boldsymbol{\psi}$-space) is the sample space of the random vector $\boldsymbol{\varphi}$. A transport equation for the composition

PDF $f(\boldsymbol{\psi}; \boldsymbol{x}, t)$ has to be formulated, which can be derived from the scalar transport equation (Equation 65) following Pope [71] and Kollmann [88]:

$$\frac{\partial \rho f}{\partial t} + \nabla \cdot (\rho f \boldsymbol{u}) + \frac{\partial}{\partial \psi_i}(\rho f S_i) = -\nabla \cdot [\rho \langle \boldsymbol{u}' \,|\boldsymbol{\psi}\rangle f] + \frac{\partial}{\partial \psi_i}\left[\rho \left\langle \frac{1}{\rho} \nabla \cdot \boldsymbol{J}_i \middle| \boldsymbol{\psi} \right\rangle f\right] \tag{70}$$

In the above equation, ρ and $\boldsymbol{u}$ are the mean density and velocity, respectively. The fluid velocity fluctuations are represented by the variable $\boldsymbol{u}'$. The brackets on the RHS $\langle .. | .. \rangle$ denote expectations; for example $\langle x \,| y \rangle$ gives the probability that *x* occurs when the event *y* is present. The first term on the LHS is the temporal change of the PDF, the second determines the convection by the mean velocity field and the third the change due to chemical reactions. The terms on the RHS represent the scalar convection due to turbulence and the molecular diffusion, respectively.

The unclosed term of the turbulent scalar convection (first term on the RHS in Equation 70) has to be modelled, for which commonly the gradient diffusion assumption is used [89]:

$$-\nabla \cdot [\rho \langle \boldsymbol{u}' \,|\boldsymbol{\psi}\rangle f] = \nabla \cdot \left(\frac{\rho \mu_t}{Sc_t} \nabla \bar{f}\right) \tag{71}$$

In the above equation, the turbulent viscosity is denoted by μ_t, and the turbulent Schmidt number, which is the ratio of diffusive momentum transport and diffusive species transport, by Sc_t.

The mean velocity and the turbulence field have to be determined for the PDF transport equation. These fields can be provided by a finite volume method, where the transport equations for mass- and momentum are solved in the Eulerian frame. This combination of a scalar PDF and the solution of the mean velocity and turbulence field with an Eulerian Finite Volume approach is known as hybrid PDF method.

The scalar PDF transport equation itself can be solved whether in the Eulerian or in the Lagrangian frame with a Monte Carlo approach [71]. As the PDF transport equation features a high dimensionality, the use of an Eulerian approach is in most cases unfeasible, whereas the Lagrangian Monte Carlo concept is suitable for PDFs with high dimensionality, albeit consuming long computational times. In this thesis, a simplified hybrid Lagrangian PDF method is introduced for the solution of the turbulent effect on the nanoparticle formation and growth. The hybrid Lagrangian PDF method in general is therefore discussed in detail in chapter 3.4.2. The specific concept applied for this thesis is explained in chapter 4.

While the scalar PDF method overcomes the closure problem of the non-linear reaction rates, it cannot determine the turbulent flow field. A composition PDF can therefore be combined with a velocity PDF. For the solution of a velocity-composition PDF, a Monte Carlo method is advantageous, because it can handle joint PDFs of large dimensionality. For this combined velocity-composition PDF, the velocity space ($\boldsymbol{v}$-space) is additionally considered, which is the sample space for the random velocity $\boldsymbol{u}$. A transport equation has to be solved for this

joint scalar velocity PDF $f(\boldsymbol{v}, \boldsymbol{\psi}; \boldsymbol{x}, t)$, for which both, reaction and convection, appear in a closed form. The composition PDF $f(\boldsymbol{\psi}; \boldsymbol{x}, t)$ can be recovered from the velocity-composition PDF $f(\boldsymbol{v}, \boldsymbol{\psi}; \boldsymbol{x}, t)$ by integrating over the velocity space:

$$f(\boldsymbol{\psi}; \boldsymbol{x}, t) = \int f(\boldsymbol{v}, \boldsymbol{\psi}; \boldsymbol{x}, t)\, d\boldsymbol{v} \tag{72}$$

A detailed description of the velocity-composition joint PDF can be found in the elaborated reviews of Pope [71] and Haworth [76].

Another closure approach to solve the turbulence-chemistry interaction is the conditional moment closure (CMC) [90, 91]. For this method, a presumed PDF is used as an independent value and the conditional means of the scalars are calculated in relation to the mixture fraction [90-92]. A presumed PDF for the mixture fraction itself is not transported [70]. The CMC method couples the fluctuations of the scalar quantities with the fluctuations of the mixture fraction [90, 91]. It is assumed that the conditional fluctuations of most gaseous species are small in comparison to their conditional means [70, 90, 91, 93].

A detailed description of PDF methods for modelling the interaction of turbulence and particle dynamics is given in chapter 3.4 with focus on Lagrangian PDF methods.

2.5.2. Infinitely fast chemistry - the Eddy Break-Up model

Infinitely fast chemistry implies that the combustion process is controlled by the rate of mixing of oxidiser and fuel and reaction kinetics have no influence. Therefore, the local mixture of fuel and oxidiser defines the rate of reaction. The reaction progress is assumed to be fully completed at the moment of mixing. The Eddy Break-Up (EBU) model, a common model, which assumes mixed-is-burnt combustion, was introduced by Spalding [94] and developed further by Magnussen and Hjertager [95]. The basis of the EBU model is a global single step, infinitely fast reaction. The EBU model determines the fuel consumption rate as a function of the mass fractions of fuel y_F and oxidiser y_O in the gas mixture and the mass fractions of the products y_P. The species mixing rate is defined by the turbulent time scale k/ε. The turbulent scalar dissipation rates of fuel $R_{D,F}$, oxidiser $R_{D,O}$ and the product species $R_{D,P}$ [96] are calculated according to Equation 73.

$$\begin{aligned} R_{D,F} &= -C_R \rho y_F \frac{\varepsilon}{k} \\ R_{D,O} &= -C_R \rho \frac{y_O}{s} \frac{\varepsilon}{k} \\ R_{D,P} &= -C'_R \rho \frac{y_P}{1+s} \frac{\varepsilon}{k} \end{aligned} \tag{73}$$

In the above equations, C_R and C_R' are model constant, which have to be tuned according to the investigated applications. In the literature, C_R and C_R' have the values 1 and 1.5, respectively [96]. For the spray flame modelled in this thesis, the values 0.6 and 15 were set

for C_R and C_R', respectively. The mean mixture density is denoted by ρ and s is the stoichiometric ratio. The product species dissipation rate has to be considered, as combustion only takes place in hot zones, where existing products can trigger the combustion process. Combustion can therefore only occur when oxidiser, fuel and products coexist. The reaction rate of the fuel $R_{R,F}$ is limited by the above shown dissipation rates. Therefore, the reaction rate corresponds to the smallest dissipation rate:

$$R_{R,F} = -min\left[R_{D,F}, R_{D,O}, R_{D,P}\right] \tag{74}$$

The produced and consumed specific amount of a species per time has to be determined for the calculation of the production rate $\dot{\omega}_i$ in the species conservation equation (Equation 14) and the heat release due to chemical reaction $\dot{\omega}_h$ in the energy conservation equation (Equations 10). This formation velocity is calculated from the reaction rate provided by Equation 74 according to Equation 22:

$$\dot{r}_i = R_{R,F}(\nu_i' - \nu_i'')$$

The source terms for the species and energy conservation equation can then be determined for a one-step reaction by Equation 24 and 24, respectively:

$$\dot{\omega}_i = M_i \dot{r}_i$$

$$\dot{\omega}_h = \sum_{i=1}^{n} \dot{\omega}_i \frac{h_i^0}{M_i}$$

For the infinitely fast chemistry approach, equilibrium chemistry is assumed, which is based on the Burke-Schumann equilibrium.

2.5.3. The Partially Stirred Reactor (PaSR) concept

The PaSR concept was developed by Golovitchev et al. [97, 98] for turbulent non-premixed and partially-premixed spray flames (for example in Diesel engines). The PaSR model has been applied by many groups for the modelling of turbulent combustion processes [99-103], commonly within Diesel engines. Chomiak and Karlsson [99] used the PaSR concept with complex reaction chemistry to predict the flame lift-off and the spray stabilization for Diesel-engine like conditions, which captured the general fluid dynamical interactions for flame formation and lift-off. The lift-off height, which increased linearly with the nozzle exit velocity, was found to correlate with experimental data. Additionally, the simulated flame stabilization zone also conforms to the expected location determined by the premixed flame stabilization theory. D'Errico et al. [100] compared the simulation results of two combustion models, the eddy dissipation model (EDM) and the PaSR model for combustion and pollutant emissions investigations in DI Diesel engines. The EDM was modified to account for the

ignition delay and for the PaSR model the In-Situ Adaptive Tabulation (ISAT) [104] algorithm was implemented to save computational time. Both models show a good agreement with experiments for the pressure rate trend in a combustion vessel and a Fiat engine. The flame calculated with the PaSR model was also found to resemble the findings by Chomiak and Karlsson [99]. Mikalsen and Roskilly [101] also applied the PaSR model with detailed chemistry to investigate the in-cylinder gas motion, the combustion and the NO_x formation in a turbocharged free-piston Diesel engine and their effects on the engine performance.

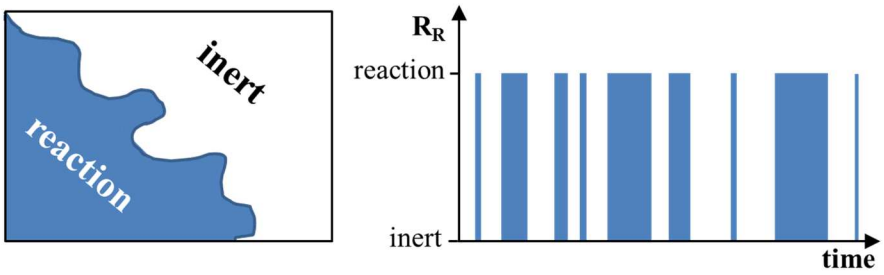

Figure 2-3: The influence of mixture imperfections on the reaction rate within a fluid volume.

The PaSR model aims to account for the influence of mixture imperfections on the chemical reaction rates due to turbulence. In a fluid volume, only a part of the volume may react, while the other part is inert, as illustrated in Figure 2-3 on the LHS. These mixture imperfections occur on the subgrid level and therefore are not captured in a RANS simulation. In a RANS context it means, that at a given point there are time-intervals with and without reaction, as shown in Figure 2-3 on the RHS. This process can be modeled by a bimodal PDF with a reacting and a non-reacting mode, as sketched in Figure 2-4. The probability that reaction occurs in a fluid volume is express by the parameter κ.: if it is zero no reaction occurs and if it is unity a perfectly mixed fluid volume can be assumed and hence, the complete mixture reacts (finite-rate chemistry).

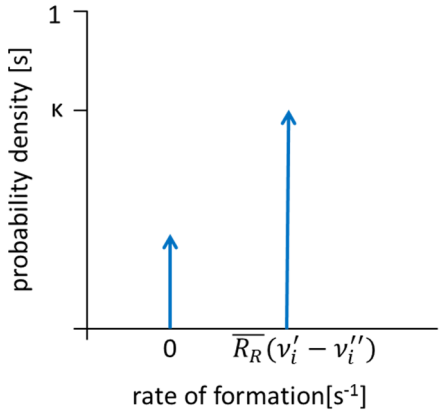

Figure 2-4: The bimodal PDF for the rate of formation in a fluid volume.

The Reynolds averaged source terms for the species transport $\bar{\dot{\omega}}_h$ and the energy transport equation $\bar{\dot{\omega}}_h$ have to be scaled by this probability κ. The corresponding equations are given by Equation 75 and 76, respectively.

$$\bar{\dot{\omega}}_i = M_i \kappa \bar{R}_R (\nu_i' - \nu_i'') \tag{75}$$

$$\bar{\dot{\omega}}_h = \sum_{i=1}^{n} \bar{\dot{\omega}}_i \frac{h_i^0}{M_i} \tag{76}$$

The reaction rate $\bar{R}_R$ in the above equation is calculated according to Equation 18. The derivation of this coefficient κ is explained subsequently.

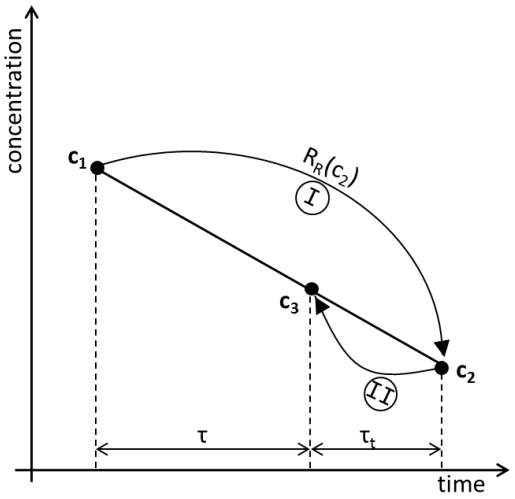

Figure 2-5: The transient process within a fluid volume for the PaSR model.

For the determination of the Reynolds averaged reaction rate $\kappa \bar{R}_R (\nu_i' - \nu_i'')$, the transient process within a fluid volume is investigated. During this process, three molar concentrations of a species have to be distinguished: c_1, c_2 and c_3. The initial molar concentration of a species within the fluid volume is c_1 and the final molar concentration is c_3. During the transient process the concentration within a fluid volume dV changes from c_1 to c_3 during the time step τ. This change corresponds to the formation velocity $\dot{r}_i$ (Equation 22) per fluid volume and is calculated by Equation 77.

$$\frac{\dot{r}_i}{dV} = \frac{dc}{\tau} = \frac{c_3 - c_1}{\tau} \tag{77}$$

The third molar concentration c_2 is the fraction of the initial concentration c_1 which takes part at the reaction. This intermediate concentration is unknown in the RANS context. The amount of time when reaction takes place, illustrated by the blue bars on the RHS in Figure 2-4, is denoted as α. At this time α the molar concentration c_1 changes to c_2, while during the other amount of time (1 - α) the molar concentration c_1 within the fluid volume is constant. The

final molar concentration can therefore be calculated from the molar concentration during reaction c_2 and the initial molar concentration according to Equation 78.

$$c_3 = \alpha c_2 + (1-\alpha)c_1 \tag{78}$$

Regarding Equation 78, it is obvious that c_3 can be obtained by a linear interpolation between c_1 and c_2, as illustrated in Figure 2-5. The transient process inside a fluid volume is divided in two steps. This assumption is illustrated in the concentration-time diagram in Figure 2-5:

I. Reaction:
A certain percentage of the molar concentration of each species changes from c_1 to c_2 due to chemical reactions.

II. Reynolds averaging:
The molar concentration c_2 of the reaction zone and the non-reacting molar concentration *c1* are averaged to the final molar concentration c_3.

During the time step τ the concentration changes from c_1 to c_3. The Reynolds averaging step can analogously be considers as a final mixing (after reaction) of c_1 to c_2 and the "mixing" time is denoted as τ_t. The whole process is described for each species by Equation 79.

$$\frac{c_3 - c_1}{\tau} = \frac{c_2 - c_3}{\tau_t} = R_R(c_2) \tag{79}$$

Equations 78 and 79 can be rearranged providing an expression for the reacting time fraction α:

$$\alpha = \tau/(\tau + \tau_t) \tag{80}$$

For Equation 79, the intermediate molar concentration in the reacting zone c_2 is unknown and also the corresponding reaction rate $R_R(c_2)$, the reaction rate for an imperfectly mixed fluid volume.

The Taylor series expansion for $R_R(c_2)$ at the point c_3 yields [98]:

$$R_R(c_2) \cong R_R(c_3) + \frac{\partial R_R}{\partial c}(c_2 - c_3) = R_R(c_3) - \frac{c_2 - c_3}{\tau_c} \tag{81}$$

In the above equation, the reaction rate $R_R(c_3)$ corresponds to the reaction rate if all fluid volume would participate in the reaction, meaning a perfectly mixed fluid volume. The reaction time τ_c is the reciprocal of the Jacobian element $\partial R_R/\partial c$ and $(\partial R_R/\partial c)_{|c=c_3} < 0$.

Equation 79 can be rearranged and the expression for c_2 substituted in Equation 81:

$$\begin{aligned} \frac{c_3 - c_1}{\tau} = R_R(c_2) &= R_R(c_3) - \frac{1}{\tau_c}\left[\left(\frac{c_3}{\alpha} - \frac{1-\alpha}{\alpha}c_1\right) - c_3\right] \\ &= R_R(c_3) - \frac{1}{\alpha\tau_c}[(1-\alpha)c_3 - (1-\alpha)c_1] \end{aligned} \tag{82}$$

Grouping c_3-c_1 yields:

$$\left(\frac{1}{\tau}+\frac{1-\alpha}{\alpha\tau_c}\right)(c_3-c_1)=R_R(c_3) \tag{83}$$

This reads finally with $\kappa=\tau_c/(\tau_c+\tau_t)$ [98]:

$$\frac{c_3-c_1}{\tau}=\kappa R_R(c_3) \tag{84}$$

The reaction rate for the imperfect mixed fluid volume $R_R(c_2)$can then be calculated with the reaction rate of a perfectly mixed fluid volume $R_R(c_3)$ scaled by the factor κ.

$$R_R(c_2)=\kappa R_R(c_3) \tag{85}$$

The reaction rate $R_R(c_3)$ in the above equation is calculated according to Equation 18 by an Arrhenius approach. The time for final "mixing" τ_t is calculated by the equation $\tau_t=C_{mix}\sqrt{\mu_{\mathrm{eff}}/(\rho\varepsilon)}$, where C_{mix} is a scaling parameter, μ_{eff} the effective viscosity (the sum of laminar (molecular) and turbulent viscosity) and ρ the density.

The reaction rate calculated from Equation 85 is then used to determine the heat release and the species source term for the energy (Equation 10) and the species conservation equation (Equation 14), respectively. Therefore, the produced specific amount of a species per time is determined according to Equation 22, but considering the imperfect mixing by the factor κ:

$$\bar{\dot{r}}_i=\kappa\overline{R_R}(\nu_i'-\nu_i'')$$

The heat release $\bar{\dot{\omega}}_h$ and the produced species $\bar{\dot{\omega}}_i$ are then calculated for each reaction and species according to Equation 75 and 76, respectively considering the imperfect mixing by this factor κ.

3. Gas-phase synthesis of nanoparticles

In this chapter, the physical processes during gas-phase synthesis of nanoparticles are described. Further, the modelling techniques for particle dynamics are introduced and the most common approaches are explained.

3.1. The synthesis process – theory

Gas-phase synthesis of nanoparticles is a continuous process, which involves many physical and chemical interacting phenomena. The three main effects of particle formation and growth, commonly described as "particle dynamics", are (a) the particle evolution from the gas-phase due to nucleation and surface growth, (b) coagulation, and (c) sintering. The particle evolution is sketched in Figure 3-1 for a spray-flame assisted gas-phase synthesis. The illustrated processes may appear simultaneously and determine the particle size and properties according to the dominant process.

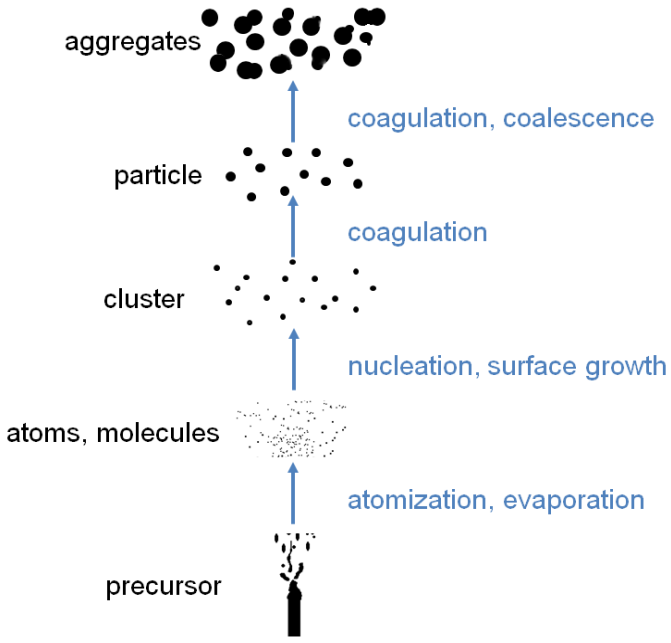

Figure 3-1: Spray-flame assisted gas-phase synthesis of nanoparticles.

3.1.1. From spray to particle

The first steps of the synthesis process can be described as follows. The injected liquid precursor within the spray flame reactor evaporates. The gaseous precursor is heated up due to the heat release from the fuel combustion. It decomposes (by thermal pyrolysis) or reacts with the flame atmosphere forming condensable products. A non-equilibrium, supersaturated state,

tends to equilibrium by generating new particles due to homogeneous nucleation or heterogeneous nucleation [105, 106].

The nucleation process is an abrupt phase transition, for gas-phase synthesis a transition from gas to a condensed state. Nucleation occurs due to a metastable thermodynamic state of the system. It is the first irreversible formation step of solid phase with supersaturation as driving force. Supersaturation is the difference in chemical potential between a molecule in the solution μ_s and the bulk of the crystal μ_c phase [107] according to Equation 86. The chemical potential is a form of potential energy, which describes the probability of a species to react, to change its phase or to diffuse. A system always tends to the state with the least chemical potential, which means that at chemical or phase equilibrium the chemical potentials sum to zero.

$$\Delta\mu = \mu_s - \mu_c = k_B T \ln S \tag{86}$$

In the above equation, k_B is the Boltzmann constant, T the absolute temperature and S the supersaturation ratio, which depends on the physical conditions of the system. When $\Delta\mu > 0$ the solution is supersaturated and nucleation and growth can occur. However, small supersaturation only causes a negligible amount of newly formed clusters, which are defined as nuclei [108]. Only when the metastable zone is reached, the nucleation rate increases rapidly. Unfortunately, there is no standard definition for the metastable zone. In general, the metastable limit for a certain material occurs at a specific temperature and concentration, where instantaneous nucleation starts.

A nucleation process can be homogeneous or heterogeneous. A **homogeneous nucleation** is a spontaneous process, which occurs in the absence of seed particles or crystals in the system. The exact process of homogeneous nucleation is quite complex and uncertain. The classical theory of nucleation was introduced for condensation of vapor to water by Becker and Döring [109], Gibbs [110] and Volmer [111] in the early 20th century, but it can be extended also to other crystallisation processes.

Homogeneous nucleation is due to a change in free energy, which is illustrated in Figure 3-2. For the formation of a new nucleus, an interface between the phases is created. For the creation of the nucleus' volume, energy is released, whereas the creation of a new interface consumes energy. When the gained energy from the formation of the volume is less than the energy needed for creation of the nucleus' surface, the nucleus is too small and unstable (also called embryo) and the nucleation process stops [112]. Assuming a spherical nucleus and spherical molecules, a cluster with the radius r_c contains $n = 4/3\pi r_c^3/V_m$ molecules with the volume V_m. Hence, the energy ΔG, which is necessary to form a cluster is the sum of the difference between the free energy of the initial and final state of the system [112] and the energy needed for the interface formation due to surface free energy with the surface tension σ [112]:

$$\Delta G = -\frac{4}{3}\pi\frac{r_c^3}{V_m}\Delta\mu + 4\pi r_c^2\sigma \tag{87}$$

For a certain cluster radius, the change in free energy in Equation 87 has a maximum as illustrated in Figure 3-2. This maximum represents the energy barrier for nucleation [112] and is calculated according to Equation 88.

$$\frac{d\Delta G}{dr} = -4\pi\frac{r_c^2}{V_m}\Delta\mu + 8\pi r_c\sigma = 0 \tag{88}$$

The corresponding cluster radius is the critical cluster radius, which is the minimal radius to assume a stable cluster [113], introduced by Equation 89.

$$r_{c,crit} = \frac{2\sigma V}{\Delta\mu} = \frac{2\sigma V}{k_B T \ln S} \tag{89}$$

Equation 89 implies that an increased supersaturation decreases the critical cluster radius [113] and hence the probability of nucleation grows.

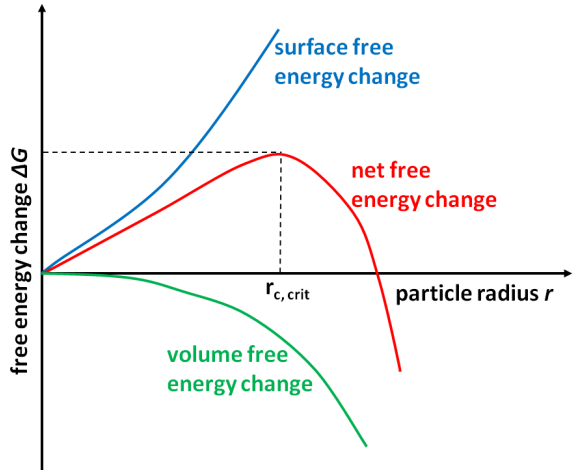

Figure 3-2: Change in free energy for homogeneous particle nucleation processes.

A **heterogeneous nucleation** process is induced by foreign particles or clusters, which are already present in a solution [107]. In a heterogeneous nucleation process, new particles are formed on the surfaces of existing particles or clusters. This nucleation process is therefore also called surface growth. For the heterogeneous nucleation, much lower supersaturation is required than for the homogeneous nucleation. In the presence of a foreign substrate, the surface free energy reduces [113]. This is due to a smaller free surface area, which can be visualised by a droplet on a surface, which has a smaller surface area than a spherical droplet. Hence, the interfacial area reduces, which leads also to a reduction of the energy barrier for nucleation (Equation 87). For the same supersaturation, particles become stable at a smaller radius than for a homogeneous nucleation process. Therefore, the heterogeneous nucleation process is more likely to occur than the homogeneous nucleation. When the existing substrate

and the nucleating substance are the same material, the maximal reduction of surface free energy can be achieved. This case is called secondary nucleation [107].

3.1.2. Coagulation

Particle coagulation is an irreversible process. It describes the process when dispersed particles collide, stick to each other and form irregular particle clusters, the so called (soft) agglomerates. The probability for particles to stick to each other after they collide depends on microscopic attachment mechanisms, which are due to physical, intermolecular forces. A coagulation of particles leads to a decrease of the total number of particles and an increase of the average particle size. The probability that two particles *i* and *j* coagulate can be determined by the corresponding collision frequency $\beta_{i,j}$. The collision frequency depends on the particle sizes and the properties of the ambient flow field, such as temperature, pressure, and velocity. The mathematical formulation for the collision frequency depends on the mechanism, with which the particles come into contact.

Collision mechanisms include Brownian motion, laminar shear and turbulence [105] and can also be affected by force fields like van der Waals forces or, if an electric field is applied, by Coulomb forces. Collision processes are mainly nonlinear, which makes a mathematical description and modelling quite challenging.

The collision and coagulation of nanoparticles, which are addressed in this thesis, are driven by **Brownian coagulation** with absence of external forces. For a particle laden flow, three regimes can be distinguished for the calculation of the Brownian coagulation. These regimes depend on the ratio of the molecular free path in the fluid to the particle radius, denoted as the Knudsen number. A Knudsen number smaller than 0.1 covers the continuum regime, for which the particle motion is described by the Stokes-Einstein diffusion coefficient. The collision frequency $\beta_{i,j}$ of two spherical particles *i* and *j* can be calculated according to Equation 90 [105] with the collision radius r_c.

$$\beta_{i,j} = \frac{2k_B T}{3\mu}\left(\frac{1}{r_{c\,i}} + \frac{1}{r_{c\,j}}\right)(r_{c\,i} + r_{c\,j}) \tag{90}$$

Large Knudsen numbers (> 10) describe the free molecular regime, where the particles and the fluid do not interact. For this region, the particle motion is molecular-like and can be calculated from the kinetic molecular theory. With the assumption of spherical nanoparticles *i* and *j*, their collision frequency $\beta_{i,j}$ can therefore be determined with the magnitude of their relative velocity $u_{rel} = \sqrt{8k_B T/(\pi m_{p_{i,j}})}$, their collision diameter d_c and their mass m_p [105]:

$$\beta_{i,j} = \pi(d_{c_i} + d_{c_j})^2 \sqrt{\frac{k_B T}{2\pi}\left[\frac{1}{m_{p_i}} + \frac{1}{m_{p_j}}\right]} \tag{91}$$

For Knudsen numbers between 0.1 and 10, the transition regime occurs, for which no adequate theory is present. However, an interpolation method can be applied to cover the whole range from continuum to the mean free path. One method was introduced by Fuchs [114] and will be described in chapter 3.3.

The simplest assumption in the coagulation theory is that particles coalesce and form one new spherical particle with a volume equivalent diameter. This is true for liquid particles. But this is not the case for many gas-phase synthesis processes, where the particles do not coalesce completely and form agglomerates with branched structures. The agglomerates' irregular shapes can change in morphology and size, which influences their transport properties and hence further collision, coagulation and sintering processes. Unfortunately, a full mathematical description of the evolving morphologies is impossible. However, the agglomerates have fractal morphologies, which can be described by different approaches [115, 116]. The irregular agglomerate structure can be described by fractal concepts [106]. The fractal dimension D_f describes the relation of the number of primary particles n_p (ratio of agglomerate v_a and the primary particle volume v_p) to the ratio of the agglomerate and primary particle diameter d_a, respective d_p [105]:

$$n_p = \frac{v_a}{v_p} = A\left(\frac{d_a}{d_p}\right)^{D_f} \tag{92}$$

In the above equation, the proportionality constant A depends on the definition of the agglomerate diameter, on the agglomeration process and on the Knudsen number. It varies from 0.95 to 1.43 for the free molecular and the continuum regime and higher values for the transition regime [105]. The concept of a fractal dimension accounts for the influence of the agglomerate structure on the collision process, where agglomerates with the same fractal dimension act similarly. It is obvious that this simple concept does not describe all agglomerate structures and characteristic processes during particle growth, but it was found to be an appropriate concept for the modelling of many aerosol processes.

3.1.3. Sintering

The sintering process changes the structure and the surface area of the particles. During the sintering process a material transport takes place in the particle agglomerates or at their interfaces. The process depends on the agglomerate structure, the thermodynamic state, and the particle (material) properties, which again depend on the particle sizes. In general, the sintering time and temperature are less for smaller particles than for larger ones [117, 118]. The agglomerate is in equilibrium when its thermodynamic potential has a minimum. The free

enthalpy of the particle interfaces is determined by the surface tension and the size of the boundary layer of the particle agglomerate. The surface tension can be assumed to be constant. Therefore, the free enthalpy of the particle interfaces can only be minimized by reducing the particles' boundary layers, which are the surface area of the particles and the grain boundaries. At the beginning of a sintering process a neck is developed between two particles, which are assumed to be spherical with the diameter d_p. This neck is defined by its characteristic diameter d_s, the sintering neck diameter. A sketch of such a neck binding is shown in Figure 3-3.

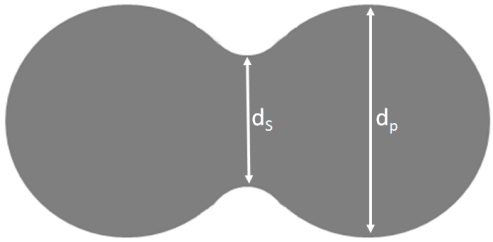

Figure 3-3: Schematic of two sintering particles.

During the sintering process, the particles' sintering neck grows until one spherical particle is formed, which has the minimum aggregate surface area a_{ss}. Particles that are bound by sinter necks are called hard agglomerates [21]. For the early sintering stages ($d_s/d_p < 0.3$), the neck growth is determined by the Equation 93 for the ratio of the neck diameter to the diameter of the uniformly sized particles [119].

$$\left(\frac{d_s}{d_p}\right)^n = C\,\frac{t}{d_p^m} \tag{93}$$

The exponents m and n depend on the type of material transport, which commonly is diffusion, evaporation or condensation. The sintering time t and the coefficient C additionally depend on the temperature and the material properties. The characteristic sintering time for a complete fused particle can be calculated from the above equation with d_s being the corresponding volume equivalent diameter of a sphere.

The change of the aggregate's surface area a can be defined by the following relaxation approach with the characteristic sintering time τ.

$$\frac{\partial a}{\partial t} = \frac{1}{\tau}(a - a_{ss}) \tag{94}$$

This linear approach is only valid for small deviations from the equilibrium in the final sintering stages [120], in contrast to the calculation approach for the neck diameter (Equation 93) used for early sintering stages. However, due to a lack of appropriate, general models, these two latter equations are commonly used for the modelling of the sintering process.

3.2. Modelling of particle dynamics

The modelling of nanoparticle synthesis enables a cost effective process design and the optimization of the operation conditions by means of parameter studies. In turbulent flame reactors, the modelling of the synthesis process involves four aspects:

- modelling of the turbulent flow field,

- modelling of the population balance equations (PBE) [70],

- solution of the turbulence-chemistry interaction during combustion, and

- modelling of the interaction of turbulence and particle dynamics.

In the first subchapter, usual models for PBE and the approach used in this work are explained. Then, common approaches for the third aspect (the particle dynamics-turbulence interaction) are introduced and the used coupling method via Lagrangian Monte Carlo particles is introduced.

3.2.1. Population balance equations

The processes within the gas-phase synthesis, i.e. formation, growth, coagulation and coalescence, specify the evolution of the size distribution in space and time. All these processes are considered in the general dynamic equation (GDE) for aerosols. The GDE is the basis for the development of aerosol models; it is a full mathematical description of the dynamics of the aerosol particles. The synthesis processes are captured by a particle size distribution function n [106]. Unlike soot and spray particles, metallic or metal-oxidic nanoparticles do not require a sink or evaporation term. The continuous distribution function changes with time and position including particle growth and coagulation as described as follows in the Eulerian frame [105].

$$\frac{\partial n}{\partial t} + \nabla \cdot n\boldsymbol{u} - \nabla \cdot D\nabla n = \left[\frac{\partial n}{\partial t}\right]_{growth} + \left[\frac{\partial n}{\partial t}\right]_{coagulation} - \nabla \cdot \boldsymbol{c}n \tag{95}$$

In this equation, the diffusion coefficient D is a function of the particle size and the particle velocity $\boldsymbol{c}$ is due to external forces. The convection is determined by the Eulerian velocity $\boldsymbol{u}$. The growth term in Equation 95 can be expressed by the particle current, which represents the particles per unit time and volume of gas passing the point or space v:

$$\left[\frac{\partial n}{\partial t}\right]_{growth} = \frac{\partial I}{\partial v} \tag{96}$$

The coagulation term can be written according to the following expression:

$$\left[\frac{\partial n}{\partial t}\right]_{coag} = \frac{1}{2}\int_0^v \beta(\tilde{v}, v-\tilde{v})\, n(\tilde{v}) n(v-\tilde{v}) d\tilde{v} - \int_0^\infty \beta(\tilde{v}, v)\, n(v) n(\tilde{v}) d\tilde{v} \tag{97}$$

In the above equation, β represents the collision frequency function or coagulation kernel (see chapter 3.1.2). The first term on the RHS describes the number of particle collisions between two classes of particles of volume $\tilde{v}$ and v, this term is multiplied by 1/2 so that a collision between two particles is not count twice. The second term on the RHS refers to the rate of loss of particles of size v by collision with all other particles [105].

Finally, the GDE of the continuous distribution function n in vector form reads [105]:

$$\frac{\partial n}{\partial t} + \nabla \cdot n\boldsymbol{u} - \nabla \cdot D\nabla \mathrm{n} = \frac{\partial I}{\partial v} + \frac{1}{2}\int_0^{\mathrm{v}} \beta(\tilde{\mathrm{v}}, \mathrm{v} - \tilde{\mathrm{v}})\, \mathrm{n}(\tilde{\mathrm{v}})\mathrm{n}(\mathrm{v} - \tilde{\mathrm{v}})\mathrm{d}\tilde{\mathrm{v}} - \int_0^{\infty} \beta(\tilde{\mathrm{v}}, \mathrm{v})\, \mathrm{n}(\mathrm{v})\mathrm{n}(\tilde{\mathrm{v}})\mathrm{d}\tilde{\mathrm{v}} - \nabla \cdot \boldsymbol{c}n \tag{98}$$

The first term on the LHS is the rate of change of the particle size distribution function per time and the second term on the LHS is the convection term. The third term on the LHS considers the diffusion of the particle size distribution. The terms on the RHS have already been discussed above. In Figure 3-5, an overview of the processes included in the GDE are shown for a fluid volume.

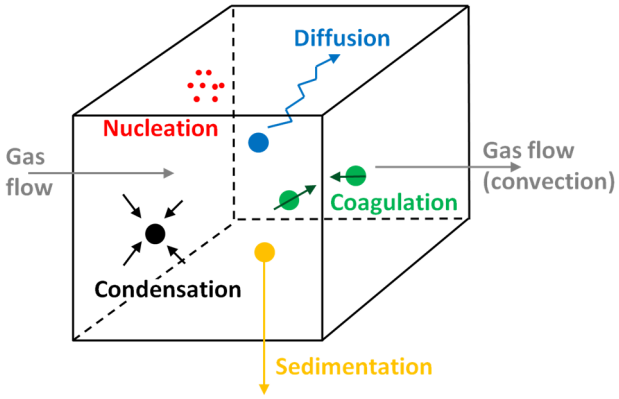

Figure 3-4: Particle processes in a fluid volume included in the GDE, according to [105].

The GDE is a type of a population balance equation (PBE) [105], where the type of equation depends on the particular case. The GDE cannot be solved analytically except for very simple cases. Normally, the GDE is transferred into simplified forms, which can be calculated numerically. Common simplified models of the GDE are discrete models, sectional models (and moving sectional), method of moments, and monodisperse methods [106]. A detailed overview over the PBE models can be found in literature, where the fundamentals and model principles are explained extensively by Friedlander [105] and Ramkrishna [121]. Therefore, only a brief overview of the most common models should be given, with focus on the monodisperse model as it is used in the present work. An overview of the principles of the different models is illustrated by the distribution functions of the particle size (defined by the diameter, volume, mass or surface area of the particles) in Figure 3-5. In this figure, the

approaches are lined up from the most accurate and most computational expensive (a) to the least accurate and least expensive (d) model.

For **discrete models,** the particle size distribution is decribed by discrete sizes, such as monomer (atom or molecule), dimer, trimer and so on [106]. Discrete models can be used for the calculation of nanoparticle synthesis processes, as the size distribution of nanoparticles comprises a relative small size range (up to 100 or 1000 monomers) compared to other synthesis processes as for example the formation of polycyclic aromatic hydrocarbons (PAHs) (soot formation). For each size class, an additional differential equation has to be solved. The discrete model is therefore not applicable for large size ranges due to the high computational cost.

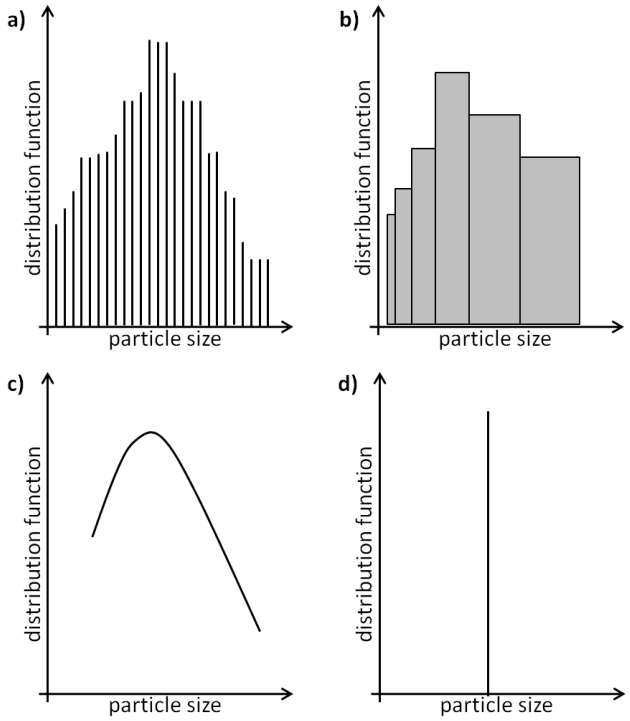

Figure 3-5: Distribution function of the a) discrete, b) sectional, c) moments and d) monodisperse model.

For wider particle size ranges, the discrete model can be combined with a sectional model, the so called discrete-sectional model, where for small particles the discrete approach is applied and for larger particles or clusters the sectional model is employed. The transition point (from discrete to sectional) depends on the application. This hybrid model is also limited due to comparatively long computational times, normally to < 100 discrete sizes and < 100 sections [106]. For further reduction of the number of differential equations, which have to be solved, a sectional model can be used for all particle size classes.

The **sectional model** divides the size distribution, as its name already implies, into sections. The particle sizes of each section have a constant value, which is normally the average of all particles of that section. The particle size distribution can therefore be illustrated by a histogram, as shown in Figure 3-5b. For every section, a differential equation has to be solved

for the conservation of e.g. the total particle number, volume or mass. The accuracy of a sectional model depends on the number of chosen sections. A larger number of sections increases the accuracy, but also the computational cost, which has to be considered according to the particular case.

Whereas discrete, discrete-sectional and sectional models provide a distribution function by approximations, for a **method of moments** an assumption of the shape of the particle size distribution has to be made. Methods of moments are used to determine the integral of the given particle size distribution function. The integro-differential GDE can be converted to ordinary differential equations [106] for the space and time dependent moments of the distribution function. These moments are integral quantities of the size distribution and are directly related to the particle characteristics, such as the total particle concentration, volume concentration or surface area concentration. The assumed size distribution is commonly a log-normal distribution, which is characterized by the particle concentration, the geometrical volume and the standard deviation. One advantage of the method of moments is that it accounts for the main physical and chemical processes such as collision, coalescence and particle deposition. A disadvantage is the presumption of the size distribution (as for example log-normal), which often does not correlate with the real distribution. However, if the distribution shape is known already and can be expressed by an analytical function, the method of moments is quite advantageous, because the complex system of equations used for discrete and sectional models can be simplified and hence, the computational effort decreased. However, this simplification also involves that only integral quantities and no distribution density functions are calculated.

Monodisperse models assume a delta peak shaped particle size distribution. Hence, they are an extremum among the methods of moments with a presumed distribution function. The advantage of these models is that they capture the main characteristics of aggregate formation with low computational effort compared to other models as for example the two-dimensional sectional model [122, 123]. The space and time dependency of a mean particle size can be determined by the monodisperse approach. These models feature simple equations for the description of the particle dynamics and consider the particle sintering rate. The implementation of monodisperse models into CFD codes is normally simple and straightforward making these models a commonly used approach for aerosol dynamics calculations. Unfortunately, the monodisperse treatment of the particles, meaning all particles having the same size for the same time and space, is a simplification that might be unrealistic and only applicable for a few cases. For monodisperse models, the soft and hard agglomerates, which evolve due to the processes described in chapter 3.1, contain the same number of equally sized primary particles [106]. The particular models differ in their mechanisms, which are used to describe the formation, growth and transport of the particles.

3.3. The particle model applied in this thesis

The synthesis of TiO_2 nanoparticle has been simulated by Tsantilis et al. [124] with monodisperse and sectional models. They found, that the average results of the monodisperse concept are in good agreement with the results of a more accurate moving sectional model and correspond well to data from experimental measurements. Hence, they have shown that monodisperse models are well suited for the calculation of the TiO_2 synthesis process. Therefore, a monodisperse model could be used in the present work for the prediction of the particle characteristics for the synthesis of TiO_2 nanoparticles.

3.3.1. The Kruis' model

A very common model for modelling particle dynamics is the simple monodisperse model by Kruis et al. [125], which was used and validated by many research groups for different reactor types and material systems [125-128].

Instantaneous chemical reactions induce the formation of product molecules, which grow to molecular clusters and form macroscopic particles due to collision. All aggregates are assumed to have the same number of primary particles of the same size. The evolution of the aggregate number concentration N is calculated by Equation 99. The rate of change of the total aggregate number concentration N is due to coagulation by particle collision at the collision frequency β of monodisperse particles leading to a decrease of N. The determination of the collision frequency (Equation 102) is described below.

$$\frac{dN}{dt} = -\frac{1}{2}\beta N^2 \tag{99}$$

The surface area of a particle aggregate a takes into account the sintering of the particles; it increases due to coagulation und decreases due to sintering [105, 120]. The aggregate surface area is calculated by Equation 100.

$$\frac{da}{dt} = -\frac{1}{N}\frac{dN}{dt}a - \frac{1}{\tau}(a - a_s) \tag{100}$$

The first term on the RHS in the above equation accounts for the increase of the surface area due to coagulation, the second term for the decrease of the surface area due to sintering, respectively. The characteristic sintering time is represented by τ and described below, according to Equation 106. The minimum surface area of an aggregate a_s is the surface area of a completely fused (spherical) aggregate [106, 125].

The aggregate volume v grows due to coagulation. It is calculated according to Equation 101.

$$\frac{dv}{dt} = -\frac{1}{N}\frac{dN}{dt}v \tag{101}$$

The **coagulation coefficient** β is modelled according to Equation 102 with Fuchs' interpolation expression, which is valid for the free molecular and the continuum regime for Brownian coagulation [122]. The solid-sphere radius, which is normally used for the Brownian coagulation expression, is replaced by the collision radius r_c, considering the irregular shape of the particle aggregate. This radius is equal the primary particle collision radius, if the number of primary particles in an aggregate is one. If the aggregate consists of more than one primary particle, the collision radius is the radius of gyration of the aggregate [106]. The radius of gyration defines the spatial expansion of an aggregate, the more compact the aggregate the smaller the radius. The parameter g, which accounts for the transition from free molecule regime to continuum is introduced by Equation 103 with the particle mean free path $l = 8D_p/(c\pi)$ and the average particle velocity $c = \sqrt{8k_BT/(\pi\rho_p v)}$ with the density of the particulate matter ρ_p.

$$\beta = 8\pi D_p\, r_c \left[\frac{r_c}{2r_c + \sqrt{2}g} + \frac{\sqrt{2}D_p}{c r_c}\right]^{-1} \tag{102}$$

$$g = \frac{[(2r_c + l)^3 - (4{r_c}^2 + l^2)^{1.5}]}{6 l r_c} - 2r_c \tag{103}$$

The collision radius is calculated by Equation 104 [129]. In this equation, $D_f = 1.8$ is the mass fractal dimension [125].

$$r_c = \frac{3v}{a}\left(\frac{a^3}{36\pi v^2}\right)^{1/D_f} \tag{104}$$

The diffusion coefficient D_p is computed from following formula [129]:

$$D_p = \frac{k_B T}{6\pi\mu\, r_c}\left[\frac{5 + 4Kn + 6Kn^2 + 18Kn^3}{5 - Kn + (8+\pi)Kn^2}\right] \tag{105}$$

Here, k_B is the Boltzmann constant ($1.38\cdot10^{-23}$ [*J/K*]), *Kn* the Knudsen number, *T* the temperature, and μ the viscosity of the flow field.

The **sintering process** in Equation 100 is characterized by the characteristic sintering time. This time depends on the synthesized material properties and corresponds to the time needed to reduce by about 63 % the excess surface area of the aggregate over that of an equal mass sphere [130]. The characteristic sintering time for TiO_2 particles used in this thesis is defined as follows, with the pre-exponential factor $A = 7.4 \cdot 10^{-8} [s\, m^{-4} K^{-1}]$ and the activation temperature $T_a = 31{,}000\ [K]$ [131]:

$$\tau = A T d_p^4 e^{\left[\frac{T_a}{T}\right]} \tag{106}$$

3.3.2. The modified Kruis' model considering nucleation

The original Kruis' model considers the evolution of existing aggregates, but does not consider the formation of new particles. Therefore, in this thesis, an extension of this model is used including a nucleation term. The particle nucleation rate is equal the formation rate of product molecules due to gas-phase reactions over a wide range of conditions [133-135]. This simplified assumption is commonly made for TiO_2 synthesis due to the lack of reliable information of the early stages of TiO_2 formation [21, 135].

An emerged particle represents a monomer particle and the nucleation rate I is calculated according to Equation 107.

$$I = -\frac{dy_{prec}}{dt}\rho N_A/M \tag{107}$$

The nucleation rate is determined by the change of precursor mass fraction dy_{prec} per time step dt, the density ρ, the molar mass M of the produced material, and Avogadro's number N_A.

Three transport equations are applied in this thesis to solve the particle dynamics; one for the particle number concentration N, one for the particle surface area concentration $A = Na$ and one for the particle volume concentration $V = Nv$. All transport equations include an additional source term, the nucleation term according to Equation 107, in comparison to the original Kruis' model. Instead of the aggregate surface area and the aggregate volume, the area surface and volume concentration are transported. The differential equations for the particle number concentration N, the surface area concentration A and volume concentrations V are expressed as follows:

$$\frac{dN}{dt} = -\frac{1}{2}\beta N^2 + I \tag{108}$$

$$\frac{dA}{dt} = -\frac{1}{\tau}(A - Na_s) + Ia_0 \tag{109}$$

$$\frac{dV}{dt} = Iv_0 \tag{110}$$

For the calculation of the nucleation term for the surface area and volume concentration in Equation 109 and 110, respectively, the surface area a_0 and volume v_0 of a monomer are used.

The introduced extended model has been commonly used for the calculation of nanoparticle dynamics. Pratsinis et al. [135], Heine et al. [136], Jeong et al. [137], Schild et al. [138], and Hong et al. [139] have applied this modified Kruis' model for the modelling of TiO_2 synthesis. A spray-flame assisted synthesis process was investigated by Gröhn et al. [140], Büsser et al. [141] and Tsantilis et al. [142], who all used this extended model. The model has provided good results in comparison with experimental data [135, 139-141], has given an insight into the synthesis process itself [135, 136, 139-141], helped to determine the essential

process parameters to control the synthesis process [139-142] and was a fundamental tool for up-scaling the synthesis process [140, 141].

The above listed publications show that the extended Kruis' model is a good first step for modelling TiO_2 nanoparticle synthesis within a spray process as attempted in this PhD project. As also turbulence effects have to be considered, the simplified Kruis' model was applied to limit the overall complexity. However, its shortcomings should not be ignored: it assumes only one size distribution, which is not realistic when particles are formed, coagulate and a second particle formation occurs, leading to a bimodal size distribution. In this thesis, a simplified Monte Carlo method is used and the Kruis' model is for these Monte Carlo particles; all Monte Carlo particles together then provide statistics of the nanoparticle dynamics. These statistics show that there are phenomena caused by turbulence that are hard to distinguish from the phenomena captured by a solution of the bimodal PBE in a laminar case. It will be shown in chapter 7 that different particle histories due to turbulence lead to bimodal size distributions. In particle measurements, it is impossible to distinguish, if a bimodal size distribution refers to similar formation and coagulation modes or to different particle histories due to turbulence.

3.4. Coupling of turbulence and particle dynamics

The calculation of the turbulent flow for the processes analysed in this thesis is realised by the solution of the Reynolds averaged Navier-Stokes (RANS) equations (see chapter 2.3.1). The RANS simulations only provide temporally averaged values for the flow field and do not reproduce the instantaneous turbulent fluctuations and the transient chemistry-turbulence interaction. The influence of the turbulent fluctuations on the particle dynamics is only negligible if the particle formation is very slow in comparison to the mixing processes, which is not the case for gas-phase synthesis of nanoparticles [19]. The transient behaviour of the flame propagation and the local micromixing effects have a crucial influence on the particle dynamics, because the formation and growth of the particles depend on the local temperature and particle nucleation rate, which are likewise not steady-state. For the particle nucleation rate and the temperature, which are required to determine the particle number, surface area, and volume concentration are random values, a probability density function (PDF) can be assigned like for example for the species composition and the temperature in turbulent combustion processes, as discussed in chapter 2.5. The nucleation rate dictates the particle formation and is proportional to the formation rate of the corresponding precursor species. The problem of the turbulence-particle dynamics (or rather the nucleation rate) interaction, is therefore equivalent to the closure problem for the reaction source terms in turbulent combustion process modelling [70], which has already been discussed in chapter 2.5. Interestingly, the coagulation process of the very small nanoparticles is not affected by

turbulence as Balthasar et al. [143] have shown that the turbulent enhancement of the collision frequency is small compared to Brownian coagulation under a wide range of conditions.

An introduction of the use of common PDF methods for particle formation processes is presented in the next subchapter. For the closure of the turbulence and particle dynamics interaction, a simplified hybrid Lagrangian PDF method is used in this work. This strategy is discussed later in this chapter.

3.4.1. PDF methods for particle formation in turbulent flows

In one of the first studies on solving the closure problem of nucleation and growth, in 1997 Baldyga et al. [144] used a presumed PDF for the modelling of a reactive precipitation process in a tubular reactor. They combined a moment transformation for the particle size distribution and a β-PDF for the mixture fraction of the chemical species. Balthasar et al. [145] simulated soot formation in aero engines with detailed chemistry and a laminar flamelet approach for the gas-phase. For soot modelling, the gas-phase reactions and the formation of the polycyclic aromatic hydrocarbons (PAH) were also calculated with the use of a flamelet library. Because the time scales of the soot particle processes (start of particle formation, heterogeneous surface growth, oxidation, and condensation) are much bigger than the turbulent time scales, the soot formation rates were stored in an additional flamelet library. The soot formation was calculated in the mixture fraction-scalar dissipation space. In a post-processing step, a transport equation for the soot mass fraction was solved with the corresponding soot formation rates from the flamelet libraries. This method has shown a good agreement with soot measurements in a lab-scale jet flame. The method of a presumed PDF and the flamelet approach for the calculation of soot formation was also applied by other groups, among them Moss et al. [146, 147].

Balthasar et al. [143] have applied a multivariate PDF for the calculation of soot formation in a plug-flow reactor with detailed gas-phase chemistry and a detailed kinetic soot model based on the method of moments. The combination of a transported PDF method and a method of moments for soot calculations was also adopted by Lindstedt and Louloudi [148]. They modelled two turbulent ethylene diffusion flames and found a good agreement of temperature and soot statistics with experimental data, showing the practical potential of the PDF approach and the importance of turbulence-chemistry interactions during soot formation. Kollmann et al. [149] simulated soot formation with a transported PDF for the mixture fraction, the enthalpy and the soot volume fraction and modelled the chemistry with an equilibrium model.

The CMC method, which was already discussed for turbulent combustion modelling, can also be applied for the calculation of soot formation. Kronenburg et al. [92] have shown by the use of a CMC method that the differential diffusion can have an influence up to 40% on the soot volume fraction. However, as the soot formation depends on the applied fuel, the setup and

other operating conditions, the effect of the differential diffusion may vary for other applications.

Akroyd et al. [150] have introduced a two-stage methodology for the detailed modelling of titania nanoparticle formation. They investigated the chloride process for a turbulent reactive flow. Their approach consists of two parts. The first part of their method was the solution of the velocity field and the gas-phase composition PDF. They applied a projected field method with a method of moments and detailed chemistry. This projected field method uses a weighted field approximation for the solution of the transport equation for a joint composition PDF. The authors' approach aimed to involve a full coupling between the flow, the chemistry and the particle dynamics. For their second modelling stage, the nanoparticle evolution should be described by a detailed population balance model. This should be realized in a post-processing step to avoid a resolution of the chemistry or the flow field. This second step will need to consider a full composition PDF instead of the mean composition considered in the first part. However, the authors addressed that the solution of this second part remains an open question.

3.4.2. Lagrangian Monte Carlo PDF methods

Lagrangian PDF methods were pioneered by Pope in 1985 in the context of turbulent flows [71, 151]. PDF transport equations used for the closure of chemistry-turbulence or particle dynamics-turbulence interaction account for a large number of independent variables, such as velocity, composition, location and time. The solution in the Eulerian framework is therefore very challenging using standard discretisation schemes [72], because the computational time increases exponentially with the number of independent variables. Hence, a very common approach to solve the PDF equations is the Lagrangian PDF method, where the computational time increases only linearly with the number of independent variables. The Lagrangian Monte Carlo PDF method provides a simple approach by employing particles to describe the stochastic differential equations and hence a direct way to model turbulent processes. The link between partial differential equations (PDE) and stochastic processes is defined by the Feynman Kac theorem [69], which states that PDEs can be expressed by random paths of stochastic processes. A review of different Lagrangian PDF solution algorithms can be found for example in the paper of Muradoglu et al. [152].

Besides the common usage of the Lagrangian PDF methods to solve the turbulence-chemistry interaction in flames, the Lagrangian Monte Carlo approach can be used for the closure of various turbulent processes. In the present work, a Lagrangian Monte Carlo PDF method is used to close the interaction of turbulence and nanoparticle formation and growth processes, where the method for the calculation of the PBE is analogous to the method used in turbulent combustion modelling. The hybrid Lagrangian Monte Carlo PDF method implemented in this

thesis is described in detail in chapter 4 and an overview of the implementation into OpenFOAM can be found in the appendix.

Lagrangian PDF methods for the solution of the turbulence-PBE interaction are commonly used for the simulation of precipitation processes in pipe flows and aerosol formation in a turbulent jet. A hybrid PBE-PDF method has been applied by Veroli and Rigopoulos [153], who coupled a PDF-Monte Carlo method to a RANS-based CFD solver. They used this approach for the calculation of turbulent precipitation in a turbulent pipe flow. The simulations were performed for the precipitation of $BaSO_4$ with a method of moments. Comparisons to experimental results of Baldyga and Orciuch [154] showed a good agreement for the particle size distribution in size and shape. Another study of Veroli and Rigopoulos [155] applied the same method for the modelling of aerosol formation in a turbulent jet. They found a critical effect of the turbulence on the particle formation at the first process stages, but a secondary effect of the turbulence further downstream, where most of the particles nucleate. Additionally, the results correlate well with experimental results given by Lesniewski and Friedlander [156]. The Lesniewski jet was also investigated by Seubert et al. [157] with a Monte Carlo particle method combined with LES to model the turbulent droplet nucleation and condensation. Their method was able to reproduce the experimental data and they have shown that the large turbulent scale must not be neglected for the calculation of the mean nucleation rate. Whereas the particle growth is not affected by the large scales, the small turbulent scales lead to a reduction in particle growth. The droplet number density correlated well with the experimental data, but some discrepancies were found for the particle size distribution. However, to the author's knowledge, no Lagrangian PDF methods for the simulation of nanoparticle synthesis in turbulent flames have been published so far.

For the Lagrangian Monte Carlo approach, the fluid is assumed to consist of particles. Each particle has a position $\boldsymbol{X}(t)$, a velocity $\boldsymbol{U}(t)$ and a thermo-chemical state vector $\boldsymbol{\varphi}(t)$, such as temperature or mixture fraction and evolves along the so called Lagrangian trajectory [151]. Along the trajectories, the statistical properties are calculated [151, 158]. For every cell of the computational grid, the PDF of a variable can be reproduced from the statistics of the Monte Carlo particles. Therefore, Lagrangian Monte Carlo methods provide a closure for the transport equation for the one-point and one-time Eulerian joint PDF. Instead of solving an Eulerian PDF transport equation, as introduced by Equation 70 for a composition joint PDF, the species composition and temperature field of the turbulent reactive flow can be derived from the Monte Carlo particles' positions in the physical and composition space.

For the determination of the Monte Carlo particle trajectories and statistics, the particle state is assumed to evolve from a Markov process. The Markov assumption describes that a current state $\theta_{\boldsymbol{n}}$ at the time t_n only depends on the previous state θ_{n-1} at time t_{n-1} and is not affected by all earlier states $\theta_{\boldsymbol{n-k}}$ at the time t_{n-k} with $k > 1$ [158]. For hybrid Lagrangian PDF methods, the

Lagrangian solver is coupled to a Finite Volume code, which provides the mean velocity and the turbulent field. The velocity vector and the turbulence, expressed for example by k and ε, are stored at the Finite Volume grid nodes and must be interpolated to the location of the Lagrangian particles. The composition Finite Volume field (for example defined by the mixture fraction) is also needed as the mean composition field for the micromixing model to determine the thermo-chemical state vector of the Monte Carlo particles [72].

As the Monte Carlo particle velocity for a hybrid method is provided by the Eulerian field (from a RANS simulation), the velocity-composition joint PDF $f(\boldsymbol{v}, \boldsymbol{\psi}, \boldsymbol{x}; t)$ reduces to a function in composition and physical space $f(\boldsymbol{\psi}, \boldsymbol{x}; t)$ [89]. For the Monte Carlo approach, the PDF can be formulated in a discrete form. For n_p equally weighted Monte Carlo particles in a cell, the three-dimensional discrete PDF $f_N(\boldsymbol{\psi}, \boldsymbol{x}; t)$ of n_s random variables φ in the sample space $\boldsymbol{\psi}$ can be expressed by scalar delta functions [71] according to Equation 111.

$$\begin{aligned} f_N(\boldsymbol{\psi}; \boldsymbol{x}, t) &= \frac{1}{n_p} \sum_{n=1}^{n_p} \delta\left(\boldsymbol{\psi} - \boldsymbol{\varphi}^{(n)}\right) \delta(\boldsymbol{x} - \boldsymbol{x}^{\boldsymbol{n}}) \\ &= \frac{1}{n_p} \sum_{n=1}^{n_p} \left[\prod_{\alpha=1}^{n_s} \delta\left(\psi_\alpha - \varphi_\alpha^{(n)}\right) \prod_{i=1}^{3} \delta\left(x_i - x_i^{(n)}\right) \right] \end{aligned} \tag{111}$$

A Dirac delta function $\delta(a - b)$ like in the above equation, represents the delta function at $a = b$. This means, that $\delta(a - b)$ is only non-zero, when the event $a = b$ occurs, where it becomes infinity and its integral unity. Hence, the product of two delta functions at the RHS is only non-zero, when both delta functions are non-zero, meaning when both defined events occur. These scalar delta function products describing the PDFs in single flow realizations are also denoted as fine-grained PDFs [74]. The delta functions are determined for all Monte Carlo particles and therefore, a probability for each scalar at each position can be derived.

Due to their different trajectories, Monte Carlo particles within one cell (at one position) can have different velocities and compositions. The distribution of the particle properties within a cell reflects the turbulent fluid properties distribution and provides the above shown discrete PDF, which represents the joint PDF in the turbulent flow. The averages of the Monte Carlo particle properties within a grid cell additionally represent an estimate of the mean fluid properties at the cell centre [151].

The initial position of the Monte Carlo particle at time t_0 is at a random location $\boldsymbol{x}$ in the physical space, where the Monte Carlo particle represents a fluid particle. The initial velocity and composition are taken from the Eulerian field [71, 72]:

$$\begin{aligned} \boldsymbol{X}(0) &= \overline{\boldsymbol{x}}, \\ \boldsymbol{U}(0) &= \overline{\boldsymbol{u}}(\boldsymbol{x}, t_0), \\ \boldsymbol{\varphi}(0) &= \overline{\boldsymbol{\varphi}}(\boldsymbol{x}, t_0) \end{aligned} \tag{112}$$

In this thesis, the Eulerian field is determined by a preliminary RANS Finite Volume simulation.

The evolution of the PDF in space and composition was introduced in chapter 2.5.1 by Equation 70, shown below and explained as follows.

$$\frac{\partial \rho f}{\partial t} + \nabla \cdot (\rho f \boldsymbol{u}) + \frac{\partial}{\partial \psi_i}(\rho f S_i) = -\nabla \cdot [\rho \langle \boldsymbol{u}' \,|\boldsymbol{\psi}\rangle f] + \frac{\partial}{\partial \psi_i}\left[\rho \left\langle \frac{1}{\rho} \nabla \cdot \boldsymbol{J}_i \middle| \boldsymbol{\psi} \right\rangle f\right]$$

The PDF evolves in physical space by convection transport due to the mean velocity (second term on LHS) and due to velocity fluctuations (first term on RHS). It also evolves in composition space due to molecular mixing (second term on RHS) and due to chemical reactions (third term on LHS) [72]. The mean velocity is provided by an Eulerian field and the chemical source term is closed. Hence, the molecular mixing and the velocity fluctuations are left, which have to be calculated by using Monte Carlo particles. Therefore, a mixing model is applied to model the molecular mixing and a discrete random walk model to determine the velocity fluctuations. Both models are subsequently discussed.

A **mixing model** is used to determine the molecular mixing for the PDF transport equation discussed in chapter 2.5.1 and shown above. The composition $\boldsymbol{\varphi}$ for each Monte Carlo particle is determined by interaction through exchange with the mean (IEM) [161] to account for the scalar mixing of the particles within each computational cell:

$$\frac{d\boldsymbol{\varphi}}{dt} - S[\boldsymbol{\varphi}(t)] = -\omega_m[\boldsymbol{\varphi} - \bar{\boldsymbol{\varphi}}] \tag{113}$$

The IEM model is a very simple model to describe the molecular mixing. It is also known as linear mean square estimation (LMSE) [162]. In the IEM model, the particle composition relaxes to the local mean composition at a given rate. The Finite Volume field provides the values for the mean composition $\bar{\varphi}$ and for $\bar{k}$ and $\bar{\varepsilon}$, which are used to calculate the turbulent mixing rate $\omega = 1/2 C_\gamma \bar{\varepsilon}/\bar{k}$ with the model constant C_γ. This approach is a hybrid method; usually, the finite volume species concentration is determined from the mean of all particles, not from a transported quantity. The second term on the LHS in Equation 113 describes the chemical source term for the particle composition. The IEM model satisfies three main requirements for a mixing model: the mean quantities do not change due to the mixing, the scalar variances decay at a given rate and the scalar quantities are bounded. Besides the IEM, various other mixing models have been published, two common approaches are the Modified Curls method [155, 156] and the Euclidean Minimum Spanning Tree (EMST) model [157, 158], respectively. For the Modified Curls model, the particles interact in pairs not with the mean. This model is based on the Curl's model [156], but for the Modified Curls model, the particles mix to a random extent and not completely as assumed for the original model. The final compositions $\boldsymbol{\varphi_i}$ and $\boldsymbol{\varphi_j}$ for two particles i and j with the mass m_i and m_j and the initial composition $\boldsymbol{\varphi_i^0}$ and $\boldsymbol{\varphi_j^0}$, respectively, are calculated with the Modified Curls model according to Equation 114. The variable a takes a random value between zero and unity.

$$\boldsymbol{\varphi_i} = (1-a)\boldsymbol{\varphi_i^0} + a\left(\frac{\boldsymbol{\varphi_i^0} m_i + \boldsymbol{\varphi_j^0} m_j}{m_i + m_j}\right)$$
$$\boldsymbol{\varphi_j} = (1-a)\boldsymbol{\varphi_j^0} + a\left(\frac{\boldsymbol{\varphi_i^0} m_i + \boldsymbol{\varphi_j^0} m_j}{m_i + m_j}\right) \quad (114)$$

The EMST model is a more complex model, but also incurs greater computational effort. It considers the location of the particles by introducing an additional state variable. The EMST model mixes particle pairs that are close to each other in composition space. The scalar fields are locally smooth and hence, particles close in composition space are probably close in physical space. The particle pairing is performed by calculating the minimum length of edges, which connects a particle with other particles; this calculation method is called Euclidean Minimum Spanning Tree. A problem of the model is that, unlikely but possible, mixing of particles that are far apart in state and space is supressed. That means that non-premixed flame quenching events at high strain, where cold fuel will mix with cold oxidiser, are not captured - so the EMST model tends to overestimate the stability of a flame.

The velocity fluctuations have to be determined for the calculation of the PDF evolution in space (Equation 70) by a **random walk model**. The Lagrangian Monte Carlo particles are gaseous fluid particles that evolve statistically in physical and composition space. The Lagrangian particle moves with the local fluid velocity of the gas-phase depending on time. The Monte Carlo particle velocity and its position at the current time are general functions of its position of the previous time. In the applied Lagrangian method in this thesis, the particles are assumed to follow the flow field calculated in the Eulerian frame. The Monte Carlo particle position is determined according to the velocity by Equation 55:

$$\frac{d\boldsymbol{X}(t)}{dt} - \boldsymbol{U}(t) = 0$$

The turbulent diffusion causes the gas molecules and hence the Monte Carlo particles, which represent these gaseous particles, to move in random directions. The effect of turbulence on the particles is calculated using the discrete random walk (DRW) model. With the discrete random walk (DRW) model a velocity in random direction is imposed on the gas-phase particles and hence, the velocity fluctuations are determined. The fluctuations can be calculated from a Gauß distribution with a variance of $\sigma = \sqrt{2/3\ k}$ [62] corresponding to the average value of the velocity fluctuations squared. The velocity fluctuation are determined by the Gaussian random variable ζ with a zero mean and a standard variation of unity: $u_i' = \zeta_i\sqrt{2/3\ k}$. The connection between discrete random walks and continuous diffusion was already proposed in 1900 by Bachelier [159]. Also Albert Einstein modelled gas-phase particle motion by a discrete random walk, which determined the random movement of gaseous molecules due to Brownian motion [160], for which he was awarded the Nobel Prize.

4. Modelling of the spray flame process

In this chapter, the final approach for the calculation of the nanoparticle synthesis for the spray flame process is presented. The Lagrangian Monte Carlo concept in general was already described in general in a previous chapter. Here, the realization of a simplified Monte Carlo method for the spray reactor is presented in a step-by-step manner. The entire simulation process is illustrated in Figure 4-1 in an activity diagram. The RANS simulation of the spray combustion within the reactor provides the initial solution for the main simulation, marked by the blue box in Figure 4-1. This main part involves the simulation of the turbulent spray combustion and the nanoparticle dynamics calculation realised by a Lagrangian Monte Carlo - Finite volume coupling.

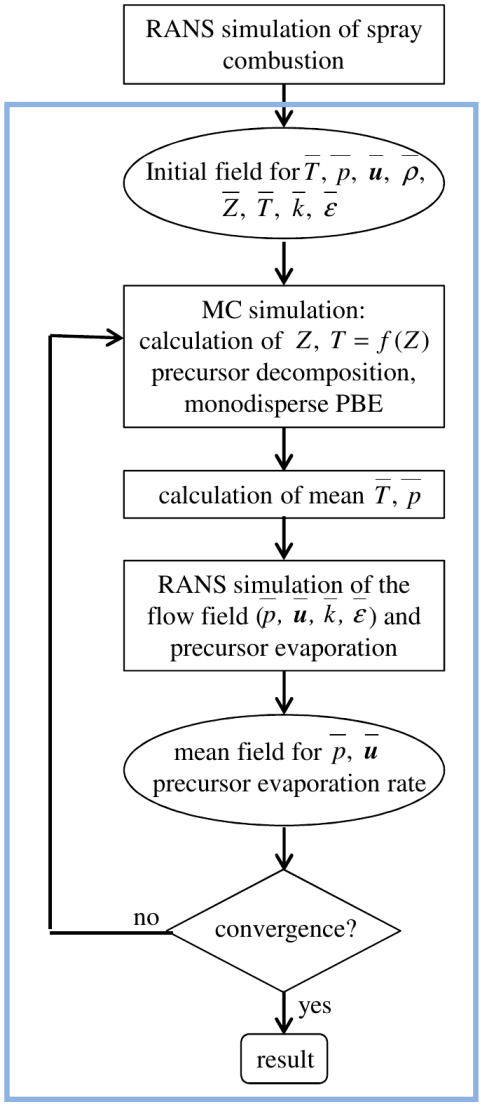

Figure 4-1: Schematic of the modelling approach for the simulation of the spray flame assisted synthesis process.

4.1. Initial RANS simulation of the spray combustion

The evaporation and the combustion of the fuel within the spray flame reactor are calculated with a RANS simulation. The turbulence is captured by the Re-Normalisation Group (RNG) k-ε approach, which is described in chapter 2.3.1.

The liquid spray droplets are modelled with a Lagrangian approach with a two-way coupling using an Euler-Lagrange approach, described in chapter 2.4.2. The phase change due to evaporation of the liquid droplets is considered by calculating the mass flow rate from the liquid to the gaseous phase by Equation 61:

$$\dot{m}_{evap} = \pi \, d_l \, Sh \, D_v \rho_s ln\left(1 + \frac{x_s - x_c}{1 - x_s}\right)$$

The precursor is dissolved within the liquid fuel. It is presumed that the vaporization characteristics of the precursor are the same as for the fuel and that the Ti-containing intermediate species do not interact with the flame kinetics. This assumption is restricted only to a small range of materials as for example TTIP, which is used in the present work, and should be handled with care [167, 168].

The Ranz-Marshall model is applied for Monte Carlo particle heat transfer using Equation 60 with the Nusselt number *Nu*:

$$Nu = 2 + 0.6Re^{0.5}Pr^{0.33}$$

The secondary break-up of the spray-droplets is modelled with the Pilch-Erdmann approach. This model provides a characteristic break-up time (Equation 57) for the spray droplets:

$$\tau_{bu} = t_{bu} \frac{d_l}{|\boldsymbol{U_{rel}}|} \sqrt{\frac{\rho_l}{\rho_g}}$$

and a final, stable droplet diameter (Equation 59):

$$d_{l,st} = We_{crit} \frac{\sigma}{\rho_g |\boldsymbol{U_{rel}}|^2}$$

The influence of the turbulence on the droplet trajectory is considered by the discrete random-walk dispersion model described in section 2.4.2.

The reactive flow is simulated by assuming infinitely fast chemistry (“mixed is burnt”) with the Eddy Break-Up model described in chapter 2.5.2 using a global one-step reaction mechanism.

The Reynolds averaged mixture fraction $\bar{Z}$ is determined from the Reynolds averaged mass fractions of the fuel $\bar{y}_F$ and the oxygen $\bar{y}_{O2}$, the fuel mass fraction in the fuel stream $\bar{y}_{F,0}$ and the oxygen mass fraction in the oxygen stream $\bar{y}_{O2,0}$ and the stoichiometric oxygen-fuel ratio

$s = \nu_{O_2} M_{O2}/M_F$, where ν_{O_2} is the stoichiometric reaction coefficient for oxygen and M_{O2} and M_F the molar mass for oxygen and fuel, respectively [27, 169]:

$$\bar{Z} = \frac{s\bar{y}_F - \bar{y}_{O2} + \bar{y}_{O2,0}}{s\bar{y}_{F,0} + \bar{y}_{O2,0}} \tag{115}$$

The chemical reactions of fuel and oxygen are presumed to be infinitely fast, so the chemical reaction finally reaches equilibrium. The temperature and the mass fractions of the fuel, oxygen, and the products can be expressed as functions of the mixture fraction. Equilibrium chemistry is assumed and provides the relation of temperature and mixture fraction for further calculations of the Lagrangian Monte Carlo particle properties.

For the transient three-dimensional simulations, a second-order central differencing scheme (see chapter 5.2.1) and the PISO (Pressure Implicit with Splitting of Operators) algorithm [170] for the coupling of pressure and velocity were used (see chapter 5.4).

This initial RANS simulation provides the Reynolds averaged mass fraction field, the relation between mixture fraction and temperature, and the initial pressure, density and velocity field as an input for further Monte Carlo simulations. The Monte Carlo - Finite Volume coupling is summarized in the boxes on the next side and explained in detail in the next subchapter.

4.2. The Monte Carlo-Finite Volume coupling approach

A. Lagrangian Monte Carlo calculation

It has to be stressed that the Monte Carlo method applied in this work is only a simplified method. The Monte Carlo particles only change their mixture fraction with the Eulerian field. This exchange is only one way, as the mixture fraction of the Eulerian field is kept constant. The precursor mass fraction is only carried by the Monte Carlo particles, which emerge due to fuel evaporation and is not exchanged by the Monte Carlo particles. It is obvious that this model has to be extended - it is only a first step towards the full closure of the turbulence-particle dynamic interaction.

The simplified Lagrangian PDF method uses the previously calculated Reynolds averaged composition and velocity field as an initial solution.

Each Monte Carlo particle evolves in physical and composition space as described in chapter 3.4.2. The thermochemical vector of the Monte Carlo particles comprises the independent scalar variables, i.e. the mixture fraction and the precursor mass fraction. The Monte Carlo particle temperature is a function of the mixture fraction assuming equilibrium chemistry.

The Monte Carlo particles are initialised at the gas inlets of the reactor according to the injected mass of the corresponding species. Additionally, they are injected at locations, where the liquid precursor and the fuel evaporate according to the mass of the gaseous species. The

Initialisation of the Finite Volume field for $\bar{Z}, \bar{T}, \bar{\rho}, \bar{\boldsymbol{u}}, \bar{p}, \bar{T}, \bar{k}, \bar{\varepsilon}$

A. Lagrangian Monte Carlo simulation:

1. Injection of Monte Carlo particles at inlet according to boundary conditions
2. Initialisation of Monte Carlo precursor and fuel particles due to evaporation rate:
   $n_p = \dot{m}\Delta t / M N_A$ (116)
3. Update of Monte Carlo particle mixture fraction (IEM):
   $\mathrm{Z}(t+\Delta t) = \mathrm{Z}(t) - \left[1 - \exp\left(-C_Y \frac{\bar{\epsilon}}{\bar{k}} \Delta t\right)\right] (\mathrm{Z}(t) - \bar{\mathrm{Z}}(t+\Delta t))$ (118)
4. Calculation of Monte Carlo particle temperature: *T = f(Z)*
5. Calculation of the precursor mass fraction for Monte Carlo particle with $y_{prec} > 0$:
   $\frac{dy_{prec}}{dt} = -A \exp\left(-\frac{E_A}{RT_P}\right) y_{prec,old}$ (119)
6. Calculation of the nanoparticle nucleation rate:
   $I = -\frac{dy_{prec}}{dt} \rho_{np} N_A / M_{np}$ (107)
7. Calculation of the PBE for Monte Carlo fuel and precursor particles:
   (a) Nanoparticle number concentration:
   $\frac{dN}{dt} = -\frac{1}{2}\beta N^2 + I$ (108)
   (b) Nanoparticle surface area concentration:
   $\frac{dA}{dt} = -\frac{1}{\tau}(A - N a_s) + I a_0$ (109)
   (c) Nanoparticle volume concentration:
   $\frac{dV}{dt} = I v_0$ (110)
   (d) Nanoparticle mean free path: $l = 8D_p/(c\pi)$ and average velocity: $c = \sqrt{8 k_B T/(\pi \rho_p v)}$
   (e) Collision radius:
   $r_c = \frac{3v}{a}\left(\frac{a^3}{36\pi v^2}\right)^{1/D_f}$ (104)
   (f) Transition parameter:
   $g = \frac{\left[(2r_c + l)^3 - \left(4{r_c}^2 + l^2\right)^{1.5}\right]}{6 l r_c} - 2r_c$ (103)
   (g) Diffusion coefficient:
   $D_p = \frac{k_B T}{6\pi\mu\, r_c}\left[\frac{5 + 4Kn + 6Kn^2 + 18Kn^3}{5 - Kn + (8+\pi)Kn^2}\right] \sim \frac{k_B T}{6\pi\mu\, r_c}$ (105)
   (h) Coagulation coefficient:
   $\beta = 8\pi D_p\, r_c \left[\frac{r_c}{2r_c + \sqrt{2}g} + \frac{\sqrt{2}D_p}{c r_c}\right]^{-1}$ (102)
   (i) Characteristic sintering time:
   $\tau = A T d_p^4 e^{\left[\frac{T_a}{T}\right]}$ (106)

B. Calculation of mean $\bar{T}$ and $\bar{\rho}$ from Monte Carlo particles:

1. Mean temperature: $\bar{T} = (\sum_{i=1}^{n} T_i)/n$
2. Density: $\bar{\rho} = \bar{p} M/(R\bar{T})$

Monte Carlo particle number n_p is calculated from the evaporated mass flow $\dot{m}$ (provided by the initial RANS simulation or by step C) with the molar mass M of the fuel or the precursor, the Avogadro's number N_A and the time step size Δt:

$$n_p = \dot{m}\Delta t / M N_A$$

C. RANS simulation for u, p and precursor evaporation:

1. Calculation of the evaporated precursor and fuel mass flow (precursor is solved in the liquid fuel and has the same vaporization characteristics as the fuel):
$$\dot{m}_{evap} = \pi\, d_l\, Sh\, D_v \rho_s ln\left(1 + \frac{x_s - x_c}{1 - x_s}\right) \quad (61)$$
2. Calculation of $\boldsymbol{u}$ and p with ρ from step B using the PISO algorithm:
   (a) Calculation of the Reynolds averaged momentum equation to compute the velocity field
   $$a_p \boldsymbol{u_P} = \boldsymbol{H}(\boldsymbol{u}) - \sum_N \boldsymbol{S}(p)_f \quad (143)$$
   (b) Prediction of the fluxes
   $$\boldsymbol{u_f} = \left(\frac{\boldsymbol{H}(\boldsymbol{u})}{a_p}\right)_f - \left(\frac{1}{a_p}\right)_f (\nabla p)_f \quad (144)$$
   (c) Construction and solution of the pressure equation
   $$\nabla \cdot \left(\frac{1}{\mathrm{a_p}} \nabla \mathrm{p}\right) = \nabla \cdot \left(\frac{\boldsymbol{H}(\boldsymbol{u})}{a_p}\right) = \sum_f \boldsymbol{S} \cdot \left(\frac{\boldsymbol{H}(\boldsymbol{u})}{a_p}\right)_f \quad (145)$$
   (d) Correction of the face flux $F = \mathbf{S} \cdot \boldsymbol{u_f}$
   (e) Calculation of the velocities due to the new pressure field
   $$\boldsymbol{u_p} = \frac{\boldsymbol{H}(\boldsymbol{u})}{a_p} - \frac{1}{a_p} \nabla p \quad (146)$$
   (f) Update of the boundary conditions
   (g) Repetition of (b)-(f) for a given number

D. Repeat of step A-C until convergence is reached

As already mentioned above, only Monte Carlo particles, which emerge due to fuel evaporation, carry precursor mass fraction and this mass fraction is not exchanged. Hence, the PBE are only calculated for these particles. Therefore, a particle ID is introduced to distinguish the Monte Carlo particles from the others as described subsequently.

Monte Carlo particles with different properties (mixture fraction, precursor mass fraction) are injected according to the type of species, which they represent. The inserted Monte Carlo particles all have a type ID to distinguish the different species, which they represent. With this type ID it can be traced if the Monte Carlo particle has emerged due to evaporation of fuel or precursor or has been injected at the reactor inlets. This assignment is needed to reduce the computational time: As nanoparticles develop due to precursor decomposition, the PBE only have to be solved for Monte Carlo particles, which represent the evaporated precursor.

Additionally, the type ID is needed for the post-processing of the nanoparticle properties as only the Monte Carlo particles emerged due to precursor evaporation carry information of the nanoparticle dynamics. However, all particles are equally weighted.

The initial mixture fraction of the Monte Carlo particles equals unity for the particles that represent the fuel and the precursor and zero for the other species. The mixture fraction for the Monte Carlo particles, which represent the gaseous precursor, can be set to one, due to the assumption that the precursor and the fuel have the same vaporization characteristics. The mixture fraction of the Monte Carlo particles evolves by IEM (see chapter 3.4.2) with the model constant $C_Y = 2$ [72]:

$$\frac{dZ}{dt} = -\frac{1}{2} C_Y \frac{\epsilon}{k} (Z - \bar{Z}) \tag{117}$$

The equation above can be transformed by an analytical integration from t to $t+\Delta t$, the mixture fraction for the new time step $t+\Delta t$ is calculated then [162] according to Equation 118.

$$Z(t + \Delta t) = Z(t) - \left[1 - exp\left(-C_Y \frac{\bar{\epsilon}}{\bar{k}} \Delta t\right)\right] (Z(t) - \bar{Z}(t + \Delta t)) \tag{118}$$

The turbulent kinetic energy $\bar{k}$ and dissipation rate $\bar{\epsilon}$ are Reynolds averaged values from the Finite Volume field, calculated according to equations 40 and 42 and determined at the position of each particle.

The initial precursor mass fraction of the Monte Carlo precursor particles equals the precursor mass fraction of the vaporized liquid. For the Monte Carlo particles representing other species, it is zero. The precursor decomposes depending on temperature. The change of the precursor mass fraction per time step is calculated with an Arrhenius approach with a simple one-step mechanism. The decomposition rate of the precursor is determined as introduced by Equation 119.

$$\frac{dy_{prec}}{dt} = -A\, exp\left(-\frac{E_A}{RT_P}\right) y_{prec,old} \tag{119}$$

Therefore, the precursor mass fraction of the Monte Carlo particles $y_{p,prec}$ decreases according to the Monte Carlo particle temperature T_p.

In addition to their position, velocity and thermo-chemical vector, the Monte Carlo particles carry variables for the calculation of the nanoparticle formation and growth. Due to the low diffusion rates of the nanoparticles, the nanoparticle Schmidt number is large (Sc ≥ 1000) and hence, the probability that nanoparticles with different histories interact (mix, coagulate or sinter) is very small. All nanoparticles within a Monte Carlo particle are assumed to be formed at one critical time and to grow simultaneously. Therefore, a monomodal size distribution can be applied and the monodisperse model can be used to calculate the nanoparticle dynamics for each Monte Carlo particle. In this work, the extended

monodisperse model by Kruis et al. [125] is applied, as described and justified in chapter 3.3.2. There are three variables that describe the nanoparticle dynamics: the nanoparticle number concentration *N*, the nanoparticle surface area concentration *A* and the nanoparticle volume concentration *V*. Additionally, the nucleation term *I*, the nanoparticle mean free path *l*, the nanoparticle velocity *c*, the coagulation coefficient β, the transition parameter *g*, the collision radius r_c, the diffusion coefficient D_p and the characteristic sintering time τ have to be determined as described in chapter 3.3.1.

In sum, the properties of a Monte Carlo particle, which evolves in time and space are defined by the composition vector of the particle $\boldsymbol{\varphi}$ with the equation below, the particle position $\boldsymbol{X} = (X_x, X_y, X_z)$, and the velocity $\boldsymbol{U} = (U_x, U_y, U_z)$. All particle properties taken together generate the state vector of a particle $\boldsymbol{\phi}(\boldsymbol{X}, \boldsymbol{U}, \boldsymbol{\varphi})$, with the composition vector $\boldsymbol{\varphi}$ shown below.

$$\boldsymbol{\varphi} = \left(ID, Z, T, \rho, age, N, V, A, I, y_{prec}, d_p, l, c, \beta, g, r_c, D_p, \tau\right)$$

The properties of the composition vector are explained in Table 4-1.

Table 4-1: Overview of the Monte Carlo particle composition vector

Properties of the composition vector:	
Z	mixture fraction
T	temperature
ρ	Monte Carlo particle density
age	Monte Carlo particle age, represents the nanoparticle residence time
ID	used to determine Monte Carlo particles for which the PBE are solved
N	nanoparticle number concentration
A	nanoparticle surface area concentration
V	nanoparticle volume concentration
I	nanoparticle nucleation rate
y_{prec}	precursor mass fraction
d_p	primary nanoparticle diameter
l	nanoparticle mean free path
c	nanoparticle velocity
β	nanoparticle collision frequency
g	nanoparticle transition parameter
r_c	nanoparticle collision radius
D_p	nanoparticle diffusion coefficient
τ	characteristic nanoparticle sintering time

The size distributions for the nanoparticle properties can be calculated from the Monte Carlo particle statistics (see chapter 3.4.2). Each Monte Carlo particle is a sample of the physical properties and the PDF can be constructed using Equation 111 for a large number of sampled Monte Carlo particles. The properties evolve with the Monte Carlo particles and can be accessed for every time step, which was stored during the simulation in every cell. Hence, an instantaneous size distribution is available for each time step in each grid cell. Boltzmann [171] has shown that for a random process the time average of a sequence of events is equal an ensemble average. This relation is called ergodicity. The properties can therefore be gathered over several time steps in a post-processing step and the distribution for each value can be calculated. The time averaged quantities were calculated by averaging locally over several particles and additionally over several time steps to obtain more samples.

B. Calculation of the mean temperature and density from the Monte Carlo particles

The Eulerian field is updated every time step by the mean values calculated from the Monte Carlo particle. The Eulerian temperature field is determined from the particle temperatures: for each cell, the mean temperature of the equally weighted particles $\bar{T}$ is calculated, where n_p is the number of particles:

$$\bar{T} = \frac{\sum_{i=1}^{n} T_i}{n_p} \tag{121}$$

The density of the Eulerian field is calculated from the temperature (interpolated from the particles) using the ideal gas law with the pressure $\bar{p}$, the mean molar mass $M = \sum_{i=1}^{n} y_i M_i$ of all species n and the gas constant R =8.314 J/(mol K):

$$\bar{\rho} = \frac{\bar{p} M}{R \bar{T}} \tag{122}$$

The mean quantities depend on the Monte Carlo particle properties and hence fluctuate widely. Therefore underrelaxation was applied for solving Equations 121 and 122 to achieve stability. Additionally, also the time step was chosen to be very small to enhance the stability of the simulation: a CFL number of 0.01 was set at the beginning of the simulation and the time step was increased during the run up to a CFL number of 0.2.

C. RANS simulation for velocity, pressure and the precursor evaporation

With the temperature and density field from the Monte Carlo particles, the velocity and pressure field are determined (by the PISO loop) and the evaporation of the spray and hence the precursor is recalculated depending on the new state. This is done according to the assumptions in step A: the gaseous mass fraction of the precursor can be computed from the amount of vaporized fuel according to the liquid mixture composition.

4.3.Limitations of the implemented model

The population balance model equations and the corresponding source and sink terms are calculated for the Monte Carlo particles. The hybrid Monte Carlo approach therefore provides statistics for the nanoparticle properties as each Monte Carlo particle acts as a small reactor itself. The Monte Carlo particles and hence the nanoparticle dynamics are affected by turbulence modelled by a discrete random walk, which is applied to each Monte Carlo particle. It has to be stressed that the model does not provide a fully two-way coupled interaction of the Monte Carlo particles and the flow field, as the mixture fraction of the Finite Volume field, with which the particles interact, is kept constant, as provided by the previous RANS simulation. Hence, the accuracy of the previous RANS calculation impinges on the accuracy of the presented approach. Additionally, the precursor mass fraction is only carried by Monte Carlo particles emerging from evaporated fuel. Therefore, an enhancement of the model involves a two-way coupling of the Monte Carlo particles and the Finite Volume field. Furthermore, the precursor mass fraction has to be exchanged by the Monte Carlo particles. Also switching to a more complex mixing model instead of the IEM approach has to be proven.

The presented Monte Carlo approach accounts for the influence of turbulent effects on the nanoparticle formation and growth, but does not solve the turbulence-chemistry interaction [71] of the spray flame. The turbulent combustion is still modeled by the EBU model.

Additionally, for a more precise modelling of the turbulent structures of the flow field, a LES method is preferred to the RANS method. A more complex and challenging modelling would be to switch to a full composition-velocity Lagrangian PDF [71] instead of using a hybrid method.

Further improvements of the model would combine the turbulence-chemistry interaction for the spray flame [172-175] and the effect of turbulence on the nanoparticle properties [70, 148, 149]. This enhancement requires the transportation of two mixture fraction PDFs [71, 176, 177] to solve the unclosed terms arising from the non-linear reactive source terms for the fuel combustion and the non-linear nanoparticle formation terms for the precursor decomposition, respectively. Furthermore, the combination and the interaction of both PDFs is an open question [150].

Additionally, for the modelling of the chemical reactions within the spray flame and the precursor decomposition, simple one-step mechanisms are used in this thesis. An enhanced model would require the use of detailed chemistry [178, 179] and flamelet look-up tables [180, 181] instead of the simple assumption of equilibrium chemistry for the relation of mixture fraction and temperature, used in this thesis.

The applied Kruis' model assumes a monodisperse nanoparticle distribution and hence cannot capture a real nanoparticle size distribution within a Monte Carlo particle. Sectional PDFs (as

bimodal) could occur within each Monte Carlo particle, if significant amounts of nanoparticles are formed at different times. However, the Kruis model implies a monotonous nanoparticle development in time within a Monte Carlo particle, which is certainly not always right. For further enhancement of the model, the accuracy of the simplified monodisperse PBE model has to be investigated. In the applied model, collisions of nanoparticles within different Monte Carlo particles are not considered; the PBEs are modelled independently for the Monte Carlo particles. An advanced model has to consider such interactions.

A detailed modelling of synthesis processes in turbulent spray flames is a complex and challenging task and requires a lot of further research. This thesis should therefore break the first ground and be a basis for further enhancements of this promising approach in the next years.

5. Numerical simulation

The Navier-Stokes equations describe the motion of a Newtonian fluid, either as conservation laws for mass, momentum and energy, or as transport equations of field quantities. They form a system of nonlinear partial differential equations of second order. Nonlinearity means, that the differential equations cannot be expressed as a linear combination of their unknown functions and the derivatives. The superposition principle is not applicable to nonlinear equations. The analytical solution of the Navier-Stokes equations is therefore not possible, except with strongly simplifying assumptions. Hence, for the Navier-Stokes equations only an approximate solution can be achieved numerically. For this numerical approximation, discretisation methods have to be introduced to express the differential equations as algebraic equations. Discretisation "converts" the continuum partial derivatives to discrete finite differences. The discretised equations can then be solved with a computer. For the solution of the Navier-Stokes equations, there are always three types of error due to approximation, which cause differences between the calculated results and the 'reality':

- The discretisation error: the discretisation methods involve approximations.
- The iteration error: the numerical solution is calculated iteratively, so the calculation time for an accurate solution is infinite, therefore a termination error always remains after stopping the iteration.
- The modelling error: due to the chosen models, the differential equations themselves might contain approximations, for example from the use of turbulence or combustion models.

The three most commonly used discretisation methods are the finite-difference method (FDM), the finite-volume method (FVM) and the finite-element method (FEM). For CFD calculations, the Finite Volume Method is mainly used due to its flexibility. For the FVM, the integral form of the conservation equation is applied. The simulation domain is divided into a finite number of control volumes, for which the field variables' spatial coordinates are associated either with cell nodes (node-centred) or the cells itself (cell-centred).

For all discretisation methods, the equations are discretised in space and for transient solutions also in time. Thus, the numerical calculation provides an approximate solution for discrete spatial and temporal positions.

The general form of a standard conservation equation for a flow property φ, which has to be discretised is:

$$\underbrace{\frac{\partial \rho \varphi}{\partial t}}_{\text{accumulation}} + \underbrace{\nabla \cdot (\rho \boldsymbol{u} \varphi)}_{\text{convection}} - \underbrace{\nabla \cdot (D \rho \nabla \varphi)}_{\text{diffusion}} = \underbrace{S_\varphi(\varphi)}_{\text{sources/sinks}} \tag{123}$$

In the next subchapter, the requirements for numerical methods are introduced, followed by the spatial and temporal discretisation methods for the above shown conservation equation in terms of the Finite Volume and the pressure-velocity coupling. The last topic in this chapter is a short general description of the OpenFOAM software package.

5.1. Requirements for a numerical simulation

For a physical simulation, a solution method has to fulfil the following criteria: for convergence a scheme must be consistent and stable [182]. For an infinitesimal fine grid ($\Delta x, \Delta y, \Delta z \rightarrow 0$) and small time steps ($\Delta t \rightarrow 0$), the discretised solution must become exact to ensure consistency: The difference between the discretised equations and the exact real equation system, which is called truncation error, must then become zero. A numerical solution method is stable, if the truncation errors decrease and if it provides a bounded solution. For stability studies, different approaches can be used, the most common one is the von Neumann's method [183], which is based on a Fourier decomposition of the numerical error. Convergence is ensured, if the solution of the discretised equations tends to the solution of the differential equations for an infinitesimal fine grid. For a steady state problem, the convergence can be checked by the residuum, which gives the truncation error. If a method is stable and consistent, it usually converges to a grid-independent solution [53].

5.2. Spatial discretisation

The basis of the spatial discretisation of the solution domain is a computational mesh. This numerical grid represents the solution domain in a discrete form; the domain is splitted into a finite number of small subdomains, for the Finite Volume into control volumes, which must not overlap. Computational meshes can be structured or unstructured. A structured or regular grid has *i-j-k* countable grid cells, which means that they consist of hexahedral elements that can be indicated exactly by their index *i, j* and *k,* for a Cartesian grid corresponding to the *x, y* and *z*-direction. An unstructured grid may be irregular, build of arbitrarily shaped elements and requires a list of the connectivity between the grid cells, which defines how vertices form the individual control volumes (grid cells).

All control volumes are bounded by flat faces. The number of faces depends on the type of the computational grid, for example a hexahedral mesh has six and a prism mesh has four faces bounding a control volume. The faces are classified into two groups: the internal faces, which connect two cells and the boundary faces at the boundary of the computational domain. The assignment of flow field quantities to vertices, faces or volumes depends on the methods implementation.

The basis of the Finite Volume is the integral form of the conservation equations (see chapter 2.1). This integral equation can be formulated for every cell. The spatial volume

integrals can be converted into surface integrals over the volume bounded surface using the Gauss' theorem.

5.2.1. Face interpolation

The calculation of the fluxes requires the determination of the value of φ and its gradient normal to the faces of the control volume. These values may also be required for the volume integrals of the source terms [53]. Therefore, the cell-centre values have to be interpolated to the face centres. The face value φ_F can be determined from the values of the neighbouring cells by interpolation, which can be realised with different schemes, namely upwind differencing, central differencing and blended differencing described below.

For the **upwind differencing** schemes, the face value φ_F is determined due to the direction of the flow, with *F* being the flux through the face *f*:

$$\varphi_f = \begin{cases} \varphi_P & \text{for F } \geq 0 \\ \varphi_N & \text{for F} < 0 \end{cases} \tag{124}$$

This means that the face value is equal the value of the centre of the cell of interest φ_P, if the flow directs out of the cell and it is equal the value of the cell centre of the neighbouring cell φ_N, if the flow directs into the cell.

This approach guarantees a boundedness of the solution, meaning it cannot cause numerical oscillations. However, it is only first order accurate [53] and induces numerical diffusion, especially in regions with large gradients. Therefore, this scheme cannot capture high gradients in the flow field. For a stable solution, the Courant-Friedrichs-Lewy condition has to be satisfied. This condition defines the maximum number of computational cells, through, which a flow quantity moves during a time step Δt. For an explicit (see chapter 5.3) upwind scheme, the CFL number must be less or equal one:

$$CFL = \left|\frac{\boldsymbol{u}\Delta t}{\Delta x}\right| \leq 1 \tag{125}$$

Here, $\boldsymbol{u}$ is velocity of the flow and Δx is the grid spacing.

The **central differencing** or linear interpolation is the approximation of the face value by a linear interpolation between the adjacent cell centres *P* and *N*:

$$\varphi_f = \varphi_P \lambda_x + \varphi_N (1 - \lambda_x) \tag{126}$$

The interpolation factor λ_x is the ratio of the distance between *N* and the centre of face *f* and the distance between the cell centres *P* and *N* through *f*:

$$\lambda_x = \frac{|x_f - x_N|}{|x_f - x_N| + |x_f - x_P|} \tag{127}$$

This scheme is second-order accurate, as for example demonstrated in the textbook by Ferziger and Peric [53], but it might cause numerical oscillations and therefore cannot guarantee the boundedness of the solution.

The **blended differencing** scheme combines the upwind differencing (UD) and the central differencing (CD) approach to benefit from the advantages of both schemes, thus preserving the boundedness and achieving a good accuracy. This is done by linear combinations of the upwind and the central differencing:

$$\varphi_f = (1-\gamma)\varphi_f(UD) + \gamma\varphi_f(CD) \tag{128}$$

The numerical diffusion is controlled with the blending factor $0 \leq \gamma \leq 1$. The blending coefficient can be constant for all faces or adaptable. An adaptable coefficient can be determined by different approaches as the Total Variation Diminishing (TVD) [184] or the Normalized Variable approach (NVA) [185, 186]. The blending factor can for example be calculated with the limited linear approach by Sweby [187], the Gamma differencing scheme [188], the van Leer [189], the superbee, the minmod scheme [190] or with other methods to couple stability and accuracy for numerical modelling.

5.2.2. Flux terms

The divergence $\nabla \cdot (\rho \boldsymbol{u}\varphi)$, which represents the convection of the conserved quantity, is discretised over the control volume by converting the volume integral into a surface integral using the Gauss theorem. It can then be expressed by the mass flux through the faces $F = (\rho \boldsymbol{u})_f \cdot \boldsymbol{S}$ [53, 188]:

$$\int_V \nabla \cdot (\rho \boldsymbol{u}\varphi) dV = \int_S (\rho \boldsymbol{u}\varphi) \cdot d\boldsymbol{S} \approx \sum_f (\rho \boldsymbol{u})_f \varphi_f \cdot \boldsymbol{S} = \sum_f F\varphi_f \tag{129}$$

In this equation, $d\boldsymbol{S}$ is an infinitesimal surface element with outward pointing normal on the control volume dV. The face value can be determined by different schemes (chapter 5.2.1).

The diffusion term $\nabla \cdot (D\rho\nabla\varphi)$ is discretised analogously to the convection term (the diffusivity is assumed to be a scalar) [188]:

$$\int_V \nabla \cdot (D\rho\nabla\varphi) dV = \int_S d\boldsymbol{S} \cdot (D\rho\nabla\varphi) \approx \sum_f (D\rho)_f (\boldsymbol{S} \cdot \nabla_f \varphi) \tag{130}$$

On orthogonal meshes, the vector through N and P and the vector $\boldsymbol{S}$ are parallel, the gradient $\nabla_f \varphi$ normal to the face can therefore be expressed by the ratio between the difference of the cell centre values φ_P and φ_N to the distance between the cell centres $|\boldsymbol{d}|$ [188]:

$$\nabla_f \varphi = \frac{\varphi_N - \varphi_P}{|\boldsymbol{d}|} \tag{131}$$

In most cases the mesh is not orthogonal and the gradient is therefore split in an orthogonal (*I*) and non-orthogonal (*II*) part [53] as:

$$\boldsymbol{S} \cdot \nabla_f \varphi = \underset{I}{\boldsymbol{j} \cdot \nabla_f \varphi} + \underset{II}{\boldsymbol{k} \cdot \nabla_f \varphi} \tag{132}$$

In this equation, the sum of the vectors $\boldsymbol{j}$ and $\boldsymbol{k}$ must be equal $\boldsymbol{S}$ and is determined by non-orthogonality approaches [53, 188].

For the solution of the partial differential equation, boundary conditions have to be determined to obtain a fully defined system. A computational mesh is bounded by the faces, which correspond to the boundaries of the physical domain. The conditions for the treatment of these faces are set by the appropriate boundary conditions. Boundary conditions can be divided into two types: the Dirichtlet condition for which a fixed value of the corresponding variable (such as pressure, temperature or velocity) is set and the von Neumann condition for which the gradient of the variable normal to the boundary has to be given.

5.3. Temporal discretisation

The temporal discretisation deals with the discretisation of the time integrals in the transport equation. Using the spatial discretisations, introduced in the previous subchapter, the transient transport equation can be expressed in the semi-discretised form [191]:

$$\int_t^{t+\Delta t} \left[\left(\frac{\partial \rho \varphi}{\partial t} \right)_p V_p + \sum_f F \varphi_f - \sum_f (D\rho)_f (\boldsymbol{S} \cdot \nabla_f \varphi) \right] dt = \int_t^{t+\Delta t} \left(Su V_p + Sp V_p \varphi_p \right) dt \tag{133}$$

The terms on the RHS are the linearized source terms. The source or sink term $S_\varphi(\varphi)$ can be a function of φ. To increase the numerical stability for steady flows and to allow the use of larger time steps and underrelaxation factors for transient runs, the source terms are linearised. Hence, the source term linearization is applied by splitting the source term into a linear *Sp* and a constant part *Su*:

$$S_f(\varphi) = Su + Sp\varphi \tag{134}$$

The parts *Su* and *Sp* may also depend on φ. The integration over the control volume is done as follows:

$$\int_V S_f(\varphi)\, dV = Su V_p + Sp V_p \varphi_p \tag{135}$$

The time is discretised through time steps Δt, at, which the centre values φ_p, the face values φ_F, and the gradients $\nabla\varphi$ are assumed to be constant [192]. The approaches for the time

discretisation differ in the way φ_p, φ_f and $\nabla\varphi$ are calculated: from the old values (explicit scheme), from the yet unknown new values (implicit scheme) or using both, with the trapezoidal rule (Crank-Nicolson).

The **explicit** method calculates the spatial terms from the values of the previous time step (the superscript *o* stands for "old") $\varphi^o = \varphi(t)$. The fully discretised transport equation for the Euler explicit method is written as follows:

$$\frac{{\rho_p}^n \varphi^n - {\rho_p}^o \varphi^o}{\Delta t} V_p + \sum_f F\varphi_f^o - \sum_f (D\rho)_f (\boldsymbol{S} \cdot \nabla_f \varphi^o) = SuV_p + SpV_p\varphi_p^o \tag{136}$$

This is the Euler explicit scheme, which is first order accurate. As this method is normally unstable, higher order explicit schemes such as the Runge-Kutta schemes are commonly applied. These schemes are stable and accurate. For explicit schemes, the CFL has to be less than unity. The CFL number on the face is defined as:

$$CFL = \frac{\boldsymbol{u_f} \cdot \boldsymbol{S}}{\boldsymbol{d} \cdot \boldsymbol{S}} \Delta t \tag{137}$$

For an **implicit** scheme, the new values are calculated from the current time step (the superscript *n* stands for "new") $\varphi^n = \varphi(t+\Delta t)$. Applying the Euler implicit method, the fully discretised transport equation is formulated according to Equation 138.

$$\frac{{\rho_p}^n \varphi^n - {\rho_p}^o \varphi^o}{\Delta t} V_p + \sum_f F\varphi_f^n - \sum_f (D\rho)_f (\boldsymbol{S} \cdot \nabla_f \varphi^n) = SuV_p + SpV_p\varphi_p^n \tag{138}$$

For a linear transport equation, this implicit time discretisation scheme is unconditionally stable, of first-order accuracy and guarantees the boundedness of the solution.

The **Crank-Nicolson method** [193] is of second-order accuracy in time and also unconditionally stable for the linear transport equation. The time derivative can be calculated from the value of φ from the previous (old) and the actual time step (new).

The temporal integral can be written as:

$$\int_t^{t+\Delta t} \varphi(t)dt = \frac{1}{2}(\varphi^o + \varphi^n)\,\Delta t \tag{139}$$

Therefore, for constant density and diffusivity, the transport equation discretised with the Crank-Nicolson method reads:

$$\begin{aligned}\frac{\rho_p^n\varphi_p^n-\rho_p^o\varphi_p^o}{\Delta t}&+\frac{1}{2}\sum_f F\varphi_f^n-\frac{1}{2}\sum_f(D\rho)_f\left(\boldsymbol{S}\cdot\nabla_f^n\varphi\right)\\&+\frac{1}{2}\sum_f F\varphi_f^o-\frac{1}{2}\sum_f(D\rho)_f\left(\boldsymbol{S}\cdot\nabla_f^o\varphi\right)\\&=SuV_p+\frac{1}{2}SpV_p\varphi_p^n+\frac{1}{2}SpV_p\varphi_p^o\end{aligned}\tag{140}$$

A general, linear algebraic equations for a control volume can be formulated as follows [53, 188], where a_P and a_N are coefficients that might be depended on φ and R_P represents the source term:

$$a_p\varphi_P^n+\sum_N a_N\varphi_N^n=\ R_P\tag{141}$$

The value of φ_P^n depends on the corresponding values of the neighbouring cells. A system of the linear algebraic equations for all cells can be expressed in a matrix form as:

$$[A][\varphi]=[R]\tag{142}$$

The sparse square matrix [A] has a_P as diagonal and a_N as off-diagonal coefficients.

5.4. Pressure-velocity coupling

The continuity equation and the momentum equations provide four equations for four unknowns; the three velocity components and the pressure, but the continuity equation does not contain the pressure explicitly. In the momentum equation, the pressure occurs in the source terms. Therefore, the pressure and the velocity are coupled, but cannot be solved in a straightforward manner: For the solution of the velocity field the pressure must be known and vice versa, so an initial guess of one of the fields must be made in order to start solving. Therefore, pressure-velocity coupling algorithms are used to determine equations for the pressure from the momentum and the continuity equations. A common method is the PISO algorithm.

The PISO algorithm is based on the SIMPLE (Semi-Implicit Method for Pressure-Linked equations) algorithm [192] with two additional correction steps, the neighbour and skewness correction. The neighbour correction describes the iterative method of the PISO algorithm: the SIMPLE correction steps are repeated several times within a PISO loop. This loop decreases the number of calculated time steps needed to ensure the consistency of the calculated velocities, fluxes and the momentum balance equation. The computational time per solver iteration increases slightly by using the PISO algorithm instead of the SIMPLE, but the overall computational time can be decreased, especially for transient cases. The skewness correction is also an iterative process: the pressure gradients are recalculated after the initial

pressure correction and the mass flux corrections are then updated using these pressure gradients. For skew meshes the skewness corrections helps to improve convergence.

The PISO algorithm involves a momentum predictor and a correction loop. For the velocity at the cell centre, the PISO algorithm proceeds as follows [188]:

(a) The first step is the momentum predictor step: the Reynolds averaged momentum equation is solved. Due to the unknown pressure gradient source term at this step, the pressure field is taken from the previous time step or the initial condition. This step provides an approximation of the velocity field:

$$a_p \boldsymbol{u_P} = \boldsymbol{H}(\boldsymbol{u}) - \sum_N \boldsymbol{S}(p)_f \tag{143}$$

with the transport term

$$\boldsymbol{H}(\boldsymbol{u}) = -\sum_N a_N \boldsymbol{u_N} + \frac{\boldsymbol{u^o}}{\Delta t}$$

(b) The fluxes are predicted according to Equation 144.

$$\boldsymbol{u_f} = \left(\frac{\boldsymbol{H}(\boldsymbol{u})}{a_p}\right)_f - \left(\frac{1}{a_p}\right)_f (\nabla p)_f \tag{144}$$

(c) The pressure solution step: the velocity field from (a) is used to assemble ***H(u)*** and the pressure equation is formulated. The solution of the pressure equation provides the new velocity field:

$$\nabla \cdot \left(\frac{1}{\mathrm{a_p}} \nabla \mathrm{p}\right) = \nabla \cdot \left(\frac{\boldsymbol{H}(\boldsymbol{u})}{a_p}\right) = \sum_f \boldsymbol{S} \cdot \left(\frac{\boldsymbol{H}(\boldsymbol{u})}{a_p}\right)_f \tag{145}$$

(d) The face flux $F = \mathbf{S} \cdot \boldsymbol{u_f}$ is calculated using Equation 144.

(e) The explicit velocity correction step: with the new pressure field, the velocity is recalculated according to the new pressure field in an explicit manner:

$$\boldsymbol{u_p} = \frac{\boldsymbol{H}(\boldsymbol{u})}{a_p} - \frac{1}{a_p} \nabla p \tag{146}$$

(f) The boundary conditions are updated.

The steps (b)-(f) are then repeated for the prescribed number of time steps.

5.5. OpenFOAM

The modelling of the spray flame process in this work was performed with OpenFOAM (**Open** source **F**ield **O**peration **A**nd **M**anipulation) [194], an open source software package under the GNU General Public License for the calculation of fluid dynamics, financial processes and multiphysics (e.g. heat transfer or electromagnetics), written in C++. The OpenFOAM functionalities are grouped into shared libraries and the executables are linked to the library functionalities. Therefore, OpenFOAM provides the possibility to implement new functionalities (new classes or solvers) without recompiling the whole program. The code structure is standardised and the user interface works through textual input files without a graphical user interface (GUI). OpenFOAM supports unstructured meshes and can run in parallel by using the message passing interface (MPI) standard. The design of OpenFOAM is described in detail by Jasak et al. [195]. Besides the solver applications, OpenFOAM also features utility applications for pre- and post-processing, for example mesh generators, data manipulation routines and post-processing interfaces for ParaView or EnSight. The base capabilities, which are offered by the OpenFOAM library, are for example, the transport models, the automatic parallelization, the Lagrangian particle tracking, the dynamic meshing, the discretisation of partial differential equations, the solution of reaction kinetics and thermophysical model, the solution of ordinary differential equations with different ODE solvers, or the solution of matrix equations with tensor and field operations.

The **libraries** in OpenFOAM consist of general and model libraries. The general library provides the general classes and associated functions, such as general operation, discretisation, solution, mesh manipulation, pre- and post-processing, particle tracking or parallelization tools. The model libraries contain the classes and functions for specific models, e.g. the thermophysical, turbulence or transport models [194].

The source code files for each **application** in OpenFOAM are stored in a directory with the name of the application. The top level source file has the application name with the .C extension and the source code parts for example for the solution of the momentum equation (UEqn.H) are integrated by header files. In a sub directory called *Make*, the files *options* and *files* are located. The *options* file contains the directory paths for locating header files and for linking the shared object libraries. The *files* file lists the source files and the name and the directory path of the executable. An application can be compiled by running the *wmake* script, which comes with OpenFOAM.

The syntax for tensor operations and partial differential equations, which is used within the solver applications, is straightforward. As an example, the differential equation

$$\frac{\partial \rho \boldsymbol{u}}{\partial t} + \nabla \cdot \varphi \boldsymbol{u} - \nabla \cdot \mu \nabla \boldsymbol{u} = -\nabla p$$

written in OpenFOAM syntax reads:

```
solve
(
     fvm::ddt(rho, U)
   + fvm::div(rho, U)
   - fvm::laplacian(mu, U)
     ==
   - fvc::grad(p)
);
```

In the above syntax `fvm::ddt` denotes the time derivative, `fvm::div` the flux term, `fvm::laplacian` the laplacian term and `fvc::grad` the gradient term. The expressions *fvm* and *fvc* determine, whether an implicit or explicit discretisation scheme is used for the corresponding term. The spatial discretisation scheme for each term can be chosen directly, the user does not have to discretise each term himself.

The directory structure of an OpenFOAM **case** contains at least a set of three directories, the *system*, the *constant* and a time directory, for example *0* [194].

The *system* directory contains at least the following files: the *controldict* file comprises the control parameters for the run, *fvSolution* sets the equation solver, tolerances and algorithm control and *fvSchemes* dictates the discretisation schemes. Additionally, there can be files to determine the decomposition method for parallelization (*decomposeParDict*), to map fields from previous runs (*mapFieldsDict*), to set fields (*setFieldsDict*), for meshing (*snappyHexMeshDict*) and many more. The *constant* directory includes all physical properties required for the run, for example for the transport, the thermophysical properties or for the particle tracking and the description of the mesh in the *polyMesh* directory. The time directories contain the data for the fields, such as velocity, temperature, pressure, meaning the data for the inner mesh cells and for the boundary conditions. The names of the time directories correspond to the simulated time when the data fields are written.

6. Modelling of synthesis processes without spray

Most nanoparticle synthesis reactors have a very straightforward design; they commonly consist of a tubular chamber and a source for heat production, such as an electric heating element, a burner or a microwave source. As a first step towards the modelling of the complex spray synthesis process introduced in chapter 7, other nanoparticle synthesis processes without spray injection were investigated. Due to the simple reactor setup and the minimal modelling effort, the simulation of a hot-wall reactor has broken the first ground in modelling synthesis processes. The findings of the hot-wall simulations have shown that despite the simple reactor design, the thermodynamic and fluid dynamical processes within the reactor are more tricky than commonly assumed. The simulations of a low-pressure microwave plasma synthesis process improved the understanding of the unsteady flow field during synthesis processes. They demonstrated how different injected gases mix and how the flow field and the synthesis process can be controlled by geometric modifications of the reactor setup. Finally, simulations of a premixed low-pressure flat flame reactor provided essential experience in modelling of synthesis processes, as also the nanoparticle dynamics were calculated. The findings of these simulations also helped experimentalists to get more design experience and to interpret their measurements.

Besides providing modelling experience and insight into the flow field and particle dynamics, the preliminary investigations detected the complexities and the resulting limits for experiments and common model assumptions for nanoparticle synthesis processes. They exposed the importance for conducting three-dimensional simulation to determine safe operating conditions and to close the gap between reactor experiments and one-dimensional simulations of the reactor kinetics and nanoparticle synthesis.

6.1. Hot-wall reactor

As an intermediate step towards the modelling of the spray flame synthesis, the flow field of a synthesis process within a hot-wall reactor was studied. The investigated hot-wall reactor was used to generate validation data for further studies on nanoparticle formation and growth. Hence, a steady flow field was advantageous to provide reproducible particle measurements. A stable reactor operation was identified with the help of flow simulations. Therefore, an optimum combination of operating conditions, reactor setup and measurement techniques had to be detected. For a certain parameter range, the flow within the reactor was investigated and possible weak spots in the reactor geometry and operation were identified. These previous reactor simulations generate essential experience in reactor modelling and helped to understand the flow field within the reactor setup and its changes due to modification of the reactor geometry and operating conditions.

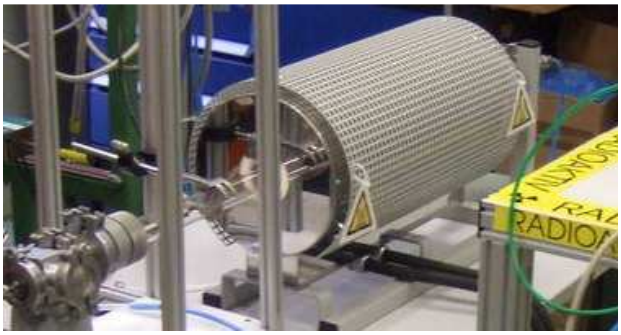

Figure 6-1: The hot-wall reactor initially aligned horizontally.

The reactor was initially aligned horizontally as illustrated in Figure 6-1 and consists of a quartz tube with an inner and outer diameter of 26 mm and 30 mm, respectively and a length of 815 mm. A sketch of the simulation domain is shown in Figure 6-2. The precursor and the carrier gas are induced through a pipe (d_{inner} = 10 mm, d_{outer} = 12 mm), which is mounted within the quartz tube. The gas is heated up to 1000° C by a heating around the quartz tube with a length of 580 mm.

The synthesized nanoparticles are sampled with a differential mobility analyser (DMA) through a pipe (d_{inner} = 4 mm, d_{outer} = 6 mm) at the end of the quartz tube and the rest gas leaves the tube through the sketched outlet.

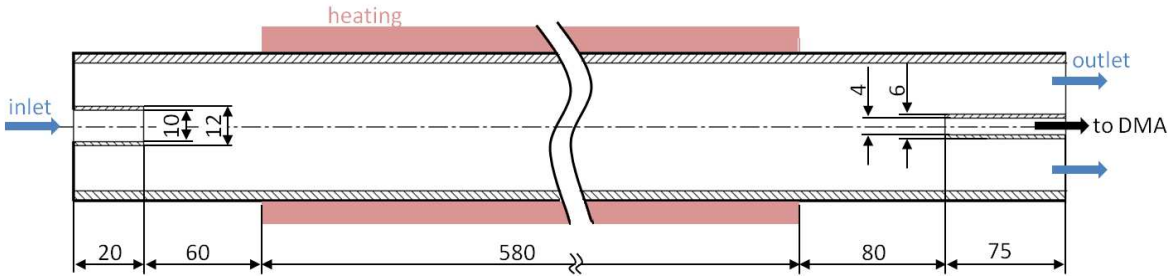

Figure 6-2: Sketch of the computational domain of the investigated hot-wall reactor.

The applied DMA restricts the carrier gas to N_2. For a proper reactor operation and for further studies of the reaction kinetics and particle dynamics, a homogenous temperature distribution and velocity field inside the reactor are desired. Because the reactor interior is not accessible for measurements, simulations were used to analyse the temperature and velocity field. Different carrier gas volume flows from 7 slm (standard litre per minute) to 15 slm were simulated, where in all cases the reactor flow was laminar with a Reynolds number < 1000 for the pipe flow (d = 10 mm) and a pressure of 1 bar. The flow was simulated with ANSYS CFX using a hexahedral grid with 150,000 nodes and an implicit second order central differencing scheme. The thermodynamic properties were given as polynomial fits in NASA format [198]. The temperature at the reactor walls was measured by a thermocouple and taken as boundary condition. The simulations have shown a very inhomogeneous temperature distribution for the horizontal reactor setup due to buoyancy. Figure 6-3 illustrates a contour plot of the

temperature on a longitudinal cross section of the reactor. To avoid these buoyancy effects, the reactor was rotated vertically.

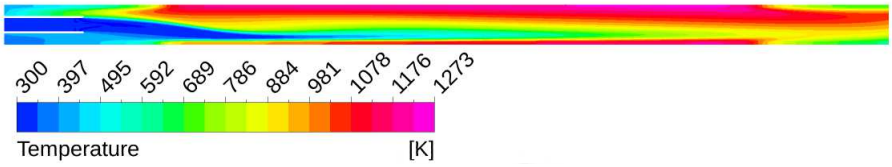

Figure 6-3: Temperature distribution within the horizontal hot-wall reactor.

For a vertical setup, a backflow at the reactor inlet was found, which is shown by the two-dimensional streamlines on the longitudinal cross section in Figure 6-4. Around the inlet pipe, recirculations were formed, which may lead to particle depositions at the tubes and hence to a reactor pollution. A simple solution was the insertion of an annular plate around the end of the inlet pipe to close the region around the inlet pipe and so to avoid the backflow. The inserted plate and the blocked part of the reactor are shown for the bottom part of the symmetric reactor in Figure 6-4.

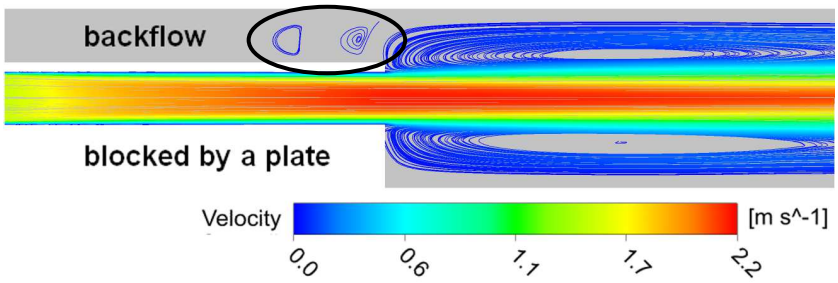

Figure 6-4: 2D velocity streamlines at the inlet of the hot-wall reactor.

For the adapted vertical reactor setup, the temperature distribution is shown for different volume flows in Figure 6-5. In all cases, a three-dimensional inhomogeneous temperature field was observed. For further investigations of the reaction kinetics and the particle dynamics with population balance equations, a hot-wall reactor would commonly be treated as a plug flow reactor. However, this model assumes that the thermodynamic conditions at the cross section of the pipe perpendicular to the reactor axis are homogeneous, meaning that the flow is one-dimensional. In Figure 6-5, it can be clearly seen that there is a temperature gradient perpendicular to the axis, which cannot be neglected. Therefore, the plug flow model is not applicable. Additionally, for high volume flows, the gas along the centreline is not heated properly, which is shown for a volume flow of 15 slm in Figure 6-5. This minor temperature may cause that the precursor is not converted completely and hence may lead to a lower particle production rate. These findings hold for N_2 as carrier gas; gases with a better heat conductivity can provide a more homogeneous temperature distribution.

However, the flow simulations have helped to improve the reactor setup and have shown that for further investigations lower inlet velocities (volume flows) are advantageous and that the plug flow model should be used with care.

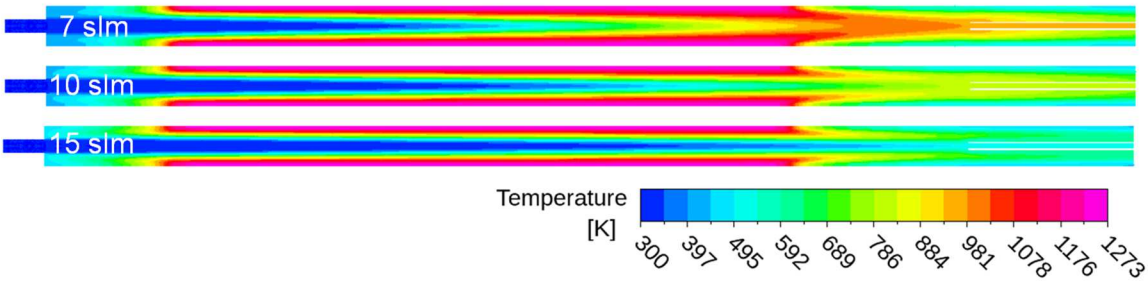

Figure 6-5: Temperature distribution within the hot-wall reactor for a vertical setup for different volume flows.

This work was a fundamental part of the AiF project IGF-ZUTECH ZN09466/08 for the design of a test reactor for investigations of particle size distributions. The calculated temperature and velocity fields were forwarded to Kruis and co-workers, who needed this data for further modelling of the particle dynamics. The work was presented at the Aerosol Technology 2014 conference (Karlsruhe) [200].

6.2. Low-pressure microwave plasma reactor

In nanoparticle synthesis reactors, a co-flow is used to shield the reactor walls from particle depositions, to direct the precursor gas jet and to quench the synthesis process. As the microwave reactor has operated very unstably and particles polluted the reactor during operation, the implementation of a swirl nozzle for the co-flow should help to enhance the flow field and hence the reactor performance. Therefore, a new co-flow nozzle was designed with the help of flow simulation to support the microwave plasma synthesis process.

These simulations of the microwave plasma reactor were an essential step towards the complex simulations of the spray-flame assisted process, as they yield experience in process modelling and a better understanding of the setup of nanoparticle reactors and the flow field within them. Additionally, the simulation results helped the experimentalists to get more design experience.

This chapter introduces the design method and the construction ideas for the nozzle and the final co-flow injector. A picture of the reactor is shown in Figure 6-6. It is oriented vertically and consists of a quartz tube with an inner diameter of 26 mm. The precursor is injected with the carrier gas through a tube, which is located at the bottom centre of the quartz tube, as sketched in Figure 6-7 and has an inner diameter of 6 mm and a length of 30 mm.

The simulated length was 250 mm, the axial position of the microwave source was located at about 95 mm above the inlet of the reactor bottom. The new co-flow nozzle should be located at the reactor bottom around the precursor inlet pipe as highlighted in grey in Figure 6-7.

For modelling the plasma, a volumetric heat source was used. This approach was published by Weise et al. and Skovorodko et al. [22, 196] for a low-pressure flat flame reactor and is described in detail in chapter 6.3.2. The volumetric shape and the heat release of the source were adjusted due to temperature measurements as provided by the experimentalists working at the reactor [197]. The applied microwave source featured a power of 2000 W and a frequency of 2.45 GHz. The corresponding volumetric heat source within the model was set by trial and error to fit the experimental measurements [197].

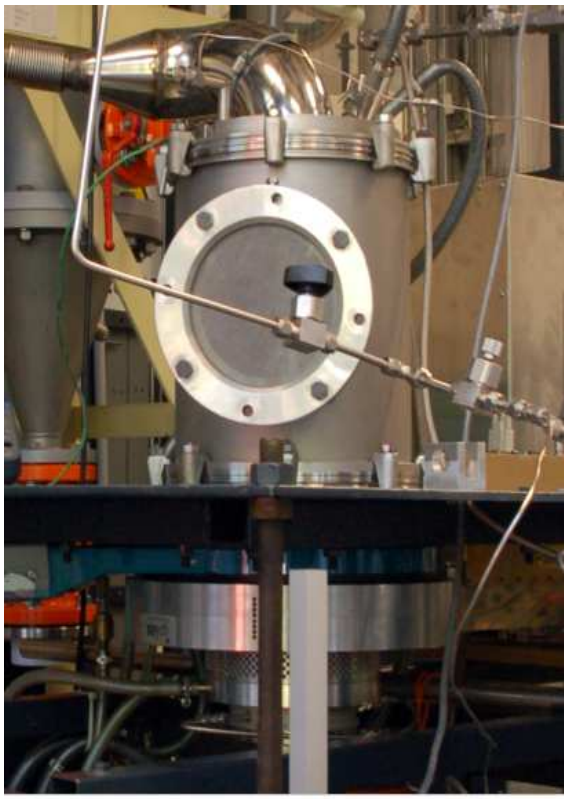

Figure 6-6: The microwave plasma reactor.

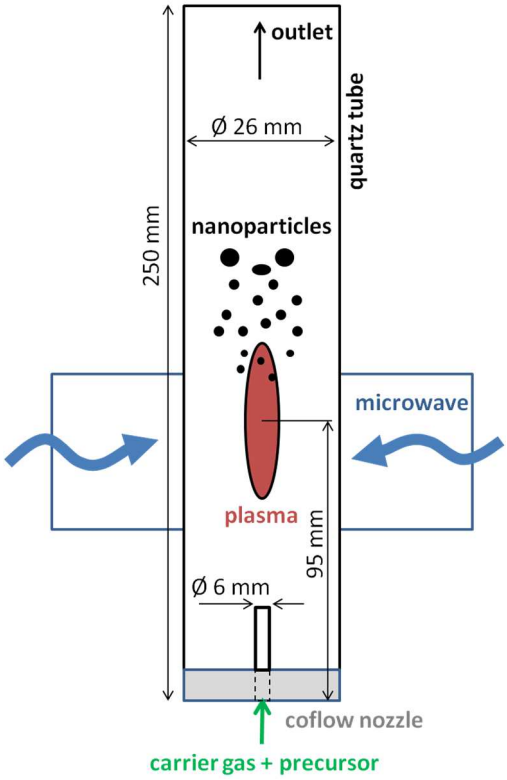

Figure 6-7: Sketch of the microwave plasma reactor.

The three-dimensional simulations were performed with Ansys CFX using a hexahedral grid and a second order central differencing scheme. A simplified implicit LES was conducted to capture the unsteady behaviour of the flow field. However, these rough calculations did not provide accurate predictions of the flow structure. The thermodynamic properties for each species of the mixture were given as polynomial fits in NASA format [198]. The mixture properties for viscosity, transport and heat conductivity were determined by the formulas by Wilke [199].

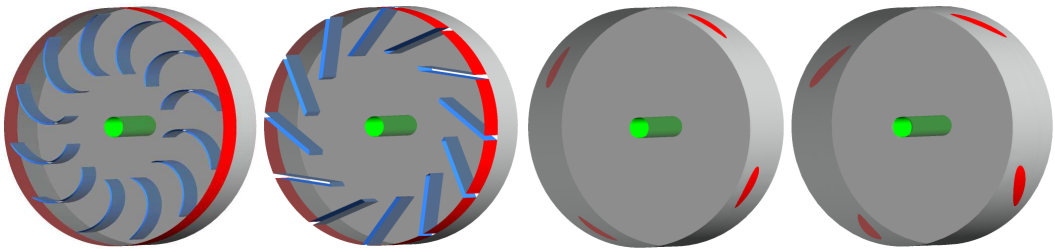

Figure 6-8: Computational domains for the nozzle concepts; from left to right: V01, V02, T04 and T04_45.

The requirements for the new nozzle features were as follows:

The nozzle should swirl the incoming sheath gas. The evolving swirl flow should stabilize the plasma by keeping it centred and avoid local flapping of the plasma. Additionally, the sheath gas should shield the reactor wall from particle depositions to keep the windows for optical access (the window in Figure 6-6 is closed) clean and prevent a pollution of the reactor. The swirl nozzle should lead to an axisymmetric, rotational symmetric flow and direct the central precursor stream. The precursor jet should feature a high velocity to penetrate the very viscous plasma “ball”.

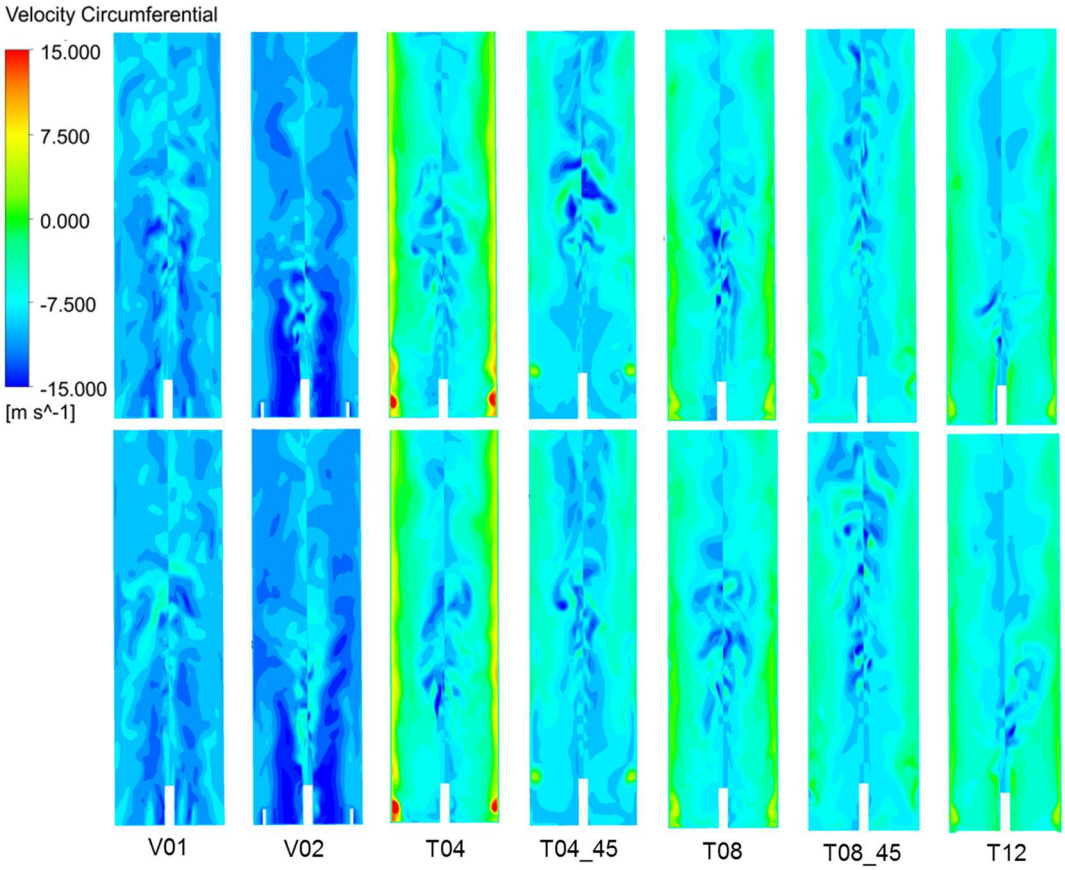

Figure 6-9: Instantaneous circumferential velocity within the reactor for the seven nozzle concepts at two time steps.

Two different approaches were pursued for the nozzle construction: the use of a guide wheel and the drilling of tangential inlet holes. Seven designs were tested for their performance: two different types of guide vanes, one with curved (V01) and one with straight vanes (V02). Additionally, cylindrical domains with the same diameter as the reactor quartz tube with four (T04), 8 (T08) and 12 (T12) tangential holes equally distributed over the circumference were designed. Two additional cases were modifications of the nozzles with the tangential holes, where the holes were additionally rotated 45° in axial direction (T04_45 and T08_45).

The three-dimensional domains of the nozzles V01, V02, T04, T04_45 are shown in Figure 6-8, where the nozzle inlet for the sheath gas is highlighted in red, the precursor inlet pipe in green and the blades in blue. Each component domain was added to the reactor domain (a pipe with a volumetric heat source), where the complete generated hexahedral mesh consisted of 800,000 - 1.1 million elements, depending on the nozzle type. The operating conditions, for which the nozzles were tested, were a pressure of 30 mbar, a carrier gas flow of 3.5 slm Ar and a sheath gas flow of 10 slm N_2, both with an inlet temperature of 300 K. The Reynolds number for the precursor flow at the inlet pipe and the mean axial flow through the quartz tube was less than 2000, hence, the flow within the reactor was mainly laminar, albeit the flow was found to be very unsteady.

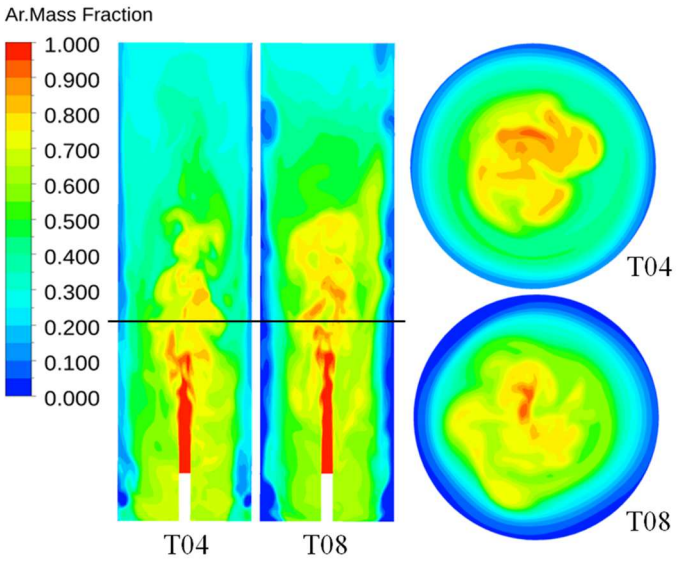

Figure 6-10: Instantaneous mass fraction of Ar within the reactor for the nozzle types T04 and T08.

Thus, seven transient, three-dimensional simulations were performed. For the rating of the constructions, the circumferential velocity within the quartz tube was illustrated to analyse the swirl provided by the nozzle.

The circumferential velocity should be high at the reactor walls and low near the centreline of the reactor. Hence, a shielding of the walls can be ensured and the precursor-carrier gas jet is directed and not disturbed by the sheath gas. The instantaneous circumferential velocity for the seven nozzle designs is illustrated in Figure 6-9 for two time steps of the transient simulation. The variants generating the best swirl flow (high circumferential velocity at the

walls and high jet velocity) are T04 and T08. For these two nozzles, the distribution of the carrier gas was investigated additionally to see the evolution of the carrier gas-precursor jet. The carrier gas (Ar) 'carrying' the precursor has to penetrate the high viscous plasma and should be kept away from the reactor walls by the co-flow gas. Hence, the mass fraction of argon should be high near the centreline of the reactor and low at the walls.

The argon mass fraction for T04 and T08 is shown in Figure 6-10 for one time step of the transient simulation. On the LHS the mass fraction is illustrated at the longitudinal cross sections and on the RHS on the cross sections at a height of 0.8 m, respectively (the locations of the right cross sections are shown by the black line in the left figures). Due to the higher circumferential velocity of variant T04, the carrier gas jet gets more spread. Hence, the variant T08 leads to a better shielding of the walls from the carrier gas and therefore was chosen to be the best design variant.

The nozzle T08 was constructed and assembled into the reactor. It has now been used for more than three years for different operating conditions, providing a stable reactor operation, a stabilized plasma and less particle depositions at the walls and the optical windows than before.

Figure 6-11: The new co-flow nozzle after operation, the path of the swirled sheath gas can be clearly seen.

Figure 6-12: Afterglow of silicon nanoparticle within the microwave plasma reactor.

The bottom wall of the disassembled swirl nozzle in Figure 6-11 shows dark depositions of the particles, where the clean streaks from the injected sheath gas illustrate the swirl of the co-flow. The reactor operating with the new nozzle for the production of silane nanoparticles is

shown in Figure 6-12. In this figure, the afterglow of silicon nanoparticles coming out of the quartz tube can be seen. The stream is stabilized and centred by the swirled co-flow due to the new nozzle.

The designed nozzle was constructed and has been built and assembled successfully to the reactor. It has been used for the last three years and was employed e.g. in the work by Sipkens et al. [201] and Wiggers et al. [202].

6.3. Premixed low-pressure flat flame reactor

In this chapter, the flow field inside a flat-flame reactor during the formation of carbon (soot) and iron oxide (from $Fe(CO)_5$) nanoparticles is analysed, and how it affects the measurements of nanoparticle size distributions. Besides the investigation of the flow field, the particle dynamics were calculated for the premixed low-pressure flat flame reactor. The work and the results in this section were already published by Weise et al. [22] and are reprinted with permission.

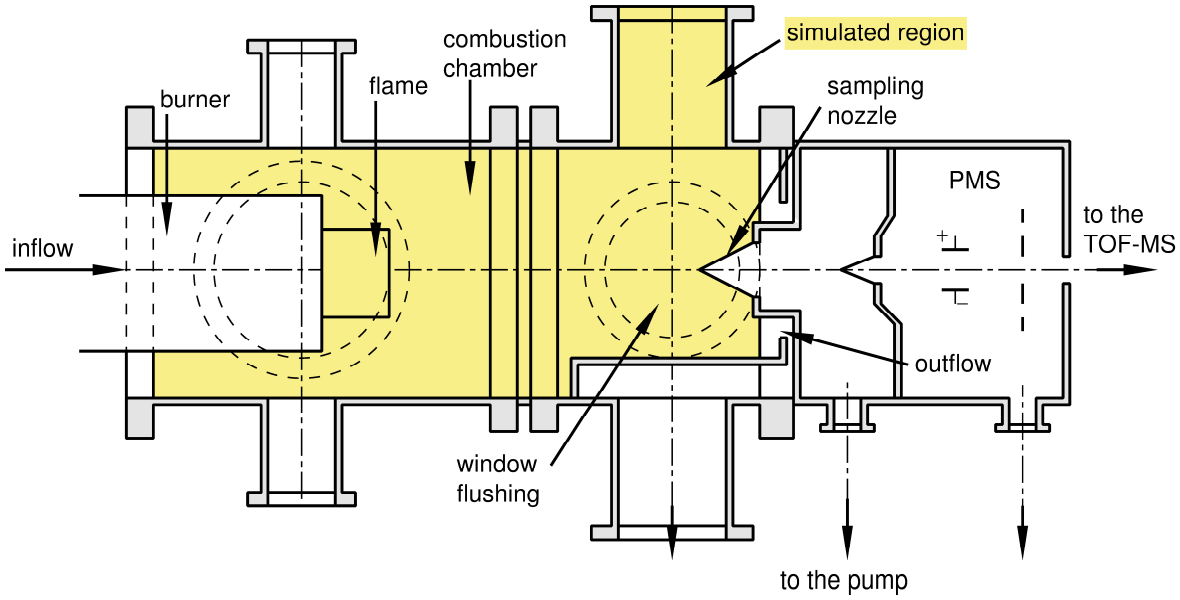

Figure 6-13: Experimental setup of the low-pressure flat flame reactor. The computational domain is highlighted in yellow.

As a step towards the complicated modelling of the processes of the spray assisted synthesis, a flat flame reactor was investigated in detail including particle formation and growth. These investigations helped to better understand the effect of the flow field on the particle dynamics and generated essential experience in particle dynamics modelling. The findings were used to improve the reactor setup and operation not only for the flat flame reactor, but for all flow reactor types used for gas-phase synthesis of nanoparticles including the spray flame reactor.

Premixed low-pressure flat flame reactors can be used to investigate the synthesis of nanoparticles. In the present work, the motivation for flow and particle simulations in this

reactor were inconsistencies, found for particle mass spectrometry (PMS) and laser induced fluorescence (LIF) measurements. The setup of the reactor is shown in Figure 6-13 and the flat flame of the reactor is illustrated in Figure 6-14.

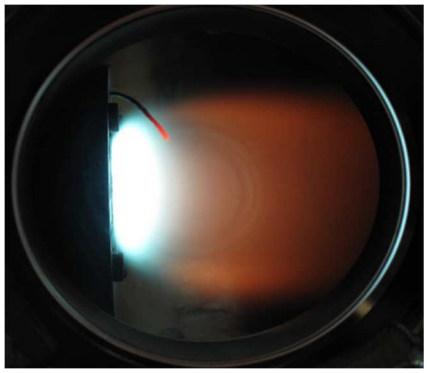

Figure 6-14: The flat flame of the premixed low-pressure flat flame reactor.

The simulations of the flat flame reactor were motivated by disagreements obtained in different experiments. PMS measurements have shown a striking, sudden increase in particle size at a critical burner distance and LIF measurements provided strong asymmetric temperature fields from a certain burner distance, respectively.

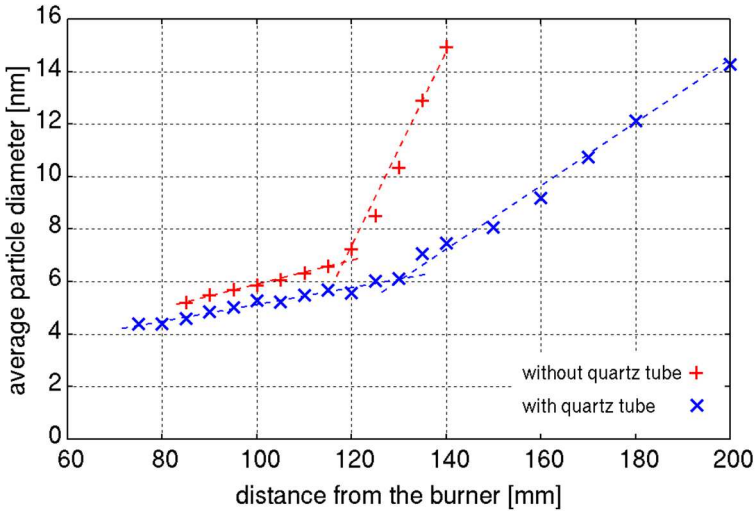

Figure 6-15: Average particle diameter measured by PMS as a function of the burner distance. Reprinted from [22] with permission.

The PMS experiments provided the mean diameter of iron oxide nanoparticles as a function of the distance from the burner. Therefore, the burner was moved to the respective position and the particles were collected via molecular beam sampling. The distance of the sampling nozzle from the burner defines the residence time of the particles inside the reaction chamber. The longer the residence time within the reactor becomes, the larger are the particle diameters due to growth, coagulation and agglomeration of the particles.

The particle size distributions are shown in Figure 6-15. Two profiles are shown for a setup with and without an insulated quartz tube. The quartz tube leads to smaller particle diameters due to its insulating effect; the heat losses of the flow are reduced and hence the temperature of the burned gases is higher, which results in slower growth of the particles and a faster coalescence process. The particle size increases linearly with the burner distance up to a certain burner position. At that distance, a sudden rise of the particle growth rate is observed, which can be delayed by using a quartz tube. The change of parameters that influence the particle size i.e. the gas temperature, the gas phase composition and the particle number concentration are small at the distances where the sudden particle size increase occurs, so the growth was suspected to result from an extended residence times of the particles inside the reactor due to buoyancy.

NO-LIF measurements [203] for the same burner setup but for slightly different operating conditions have shown an asymmetric temperature field, as it is illustrated in Figure 6-16 for a distance of 50 mm from the burner. The region of the maximum temperature is located off the burner axis due to the ascending hot gas stream. This observation confirmed the presumption that buoyancy has an essential effect on the flow fields within the reactor.

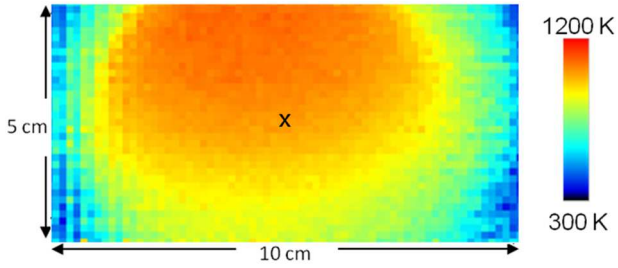

Figure 6-16: Two-dimensional temperature distribution at a distance from the burner of 50 mm measured with multi-line NO-LIF [203]. The cross indicates the location of the ceterline.

The assumption of buoyancy influencing the flow field was tested and confirmed by analysing the flow field for various burner positions. The symmetry of the flow within the reactor and the impact of buoyancy were analysed by three-dimensional simulations and one-dimensional particle dynamics along different streamlines.

6.3.1. Experimental setup

The reactor setup is sketched in Figure 6-13, the experimental technique was described in detail by Ifeacho and Roth [204, 205]. The reactor consists of three cylindrical chambers (combustion, expansion, and analysis chamber) with a diameter of 100 mm, which are differentially pumped to reduce the pressure from 15–30 mbar in the combustion chamber to a pressure of 10^{-5} mbar – 10^{-6} mbar in the analysis chamber. All chambers are oriented horizontally, resulting in a horizontal gas flow. The combustion chamber contains a water cooled matrix burner (d = 35 mm), optical windows (d = 52 mm), a vacuum pump

connection, and a sampling nozzle (d_{max} = 23 mm, l = 24.2 mm) that extracts the gas samples through a 500 µm orifice and forms a molecular beam travelling towards the PMS. The exhaust gas can leave the reactor through an annular gap (d_{inner} = 40 mm, d_{outer} = 56 mm) around the sampling nozzle. A quartz tube with an inner diameter of 84 mm can be mounted around the burner to shield the hot gas from the reactor walls. Measurements were performed with and without the quartz tube, and CFD was able to explain the beneficial effect of the quartz tube. The distance between the burner matrix and the sampling nozzle could be varied for the measurements with an accuracy of approximately 0.1 mm over the range of 0 mm – 400 mm. The distance from the burner is usually assumed to be a strictly monotonic function of the residence time, but experimental data lead to peculiar behaviour (Figure 6-15), raising doubts about this assumption. A three-dimensional simulation was hence attempted to better understand the phenomena that may cause this behaviour.

A premixed lean $Ar/O_2/H_2$ flame was stabilised on the sintered metal burner matrix. The individual gas flow rates were 400 standard cubic centimetres per minute (sccm) for H_2, 400 sccm for O_2, and 600 sccm for Ar seeded [206] with a volume fraction of 300 ppm $Fe(CO)_5$ at an operating pressure of 30 mbar. The simulations for the soot formation flame were carried out for the reactor fired with 500 sccm Ar, 500 sccm and 640 sccm C_2H_2 at a pressure of 25 mbar. Gases were extracted through a 500 µm orifice (nickel sampling nozzle) and the gas cone centre was further sampled through a second 500 µm orifice (nickel skimmer). The consequent rapid reduction in pressure impedes further reactions in the gas sample and results in the formation of a molecular beam, which passes between the two plates of the PMS capacitor. When an electrical field is applied to the electrodes, charged particles are deflected according to their mass-to-charge (m/z) ratios. Outside the electrical field the particles continue to move on straight trajectories and eventually impact two Faraday cups, as shown in Figure 6-13. The resulting current is amplified and measured as a function of the deflection voltage to give the PMS spectrum. Roth and Hospital [205] have shown that the PMS spectrum can be converted to the probability density function (PDF) of the particle mass under the assumption that only singly charged spherical particles contribute to the measured current. The particle velocity was measured with an electrical beam chopping method described by Roth [205].

In previous measurements [203] for the same reactor at slightly different operating conditions (different flow rate), the two-dimensional temperature distribution for an $Ar/O_2/H_2$ flame was measured with multi-line NO-LIF using the method described by Kronemayer [207]. The measurements were taken at a plane parallel to the burner matrix. The LIF-signal was detected by an image amplifying camera. The NO-LIF spectrum was calculated with a Levenberg-Marquat algorithm using the software LIFSim [208]. In the temperature range of 300 K to 2000 K, the temperature can be calculated with an error of 3 - 5 %, depending on the exact temperature range.

6.3.2. Flow simulations

The flow inside the reactor is laminar and characterized by low Mach (Ma < 0.015) and low Reynolds numbers (Re < 100, according to the reactor diameter) for all simulated operating conditions and geometry variations. The pressure features a constant low value of 30 mbar for all operating conditions. Buoyancy forces that result from fluid density gradients inside a

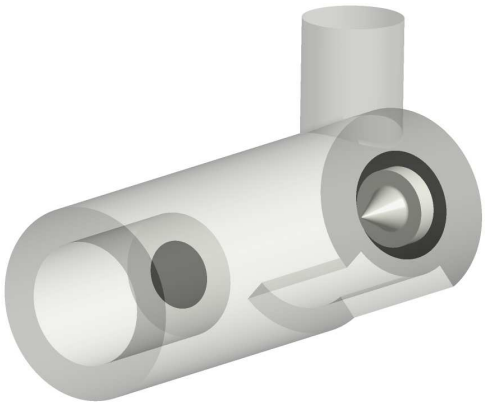

Figure 6-17: The 3D-CFD model of the reactor, showing the inlet and outlet highlighted in black. Reprinted from [22] with permission.

conservative force field are described by the volume force density as a source term in the momentum equation. The gravity term is calculated for the gas density depending on the composition and the temperature.

The reactor geometry variations result from changing the burner position relative to the sampling orifice and from the insertion of an additional quartz tube inside the reaction chamber. To perform the parameter studies for various geometry and operating conditions, a total of 25 simulations were needed. The calculation of the flow field inside the reactor requires the knowledge of the thermal heat release through chemical reactions, as a direct integration of the finite rate chemistry is impracticable for the large number of simulations to be performed for different geometries variants. For the analysis of the global buoyancy effect, the details of combustion are not relevant, only the heat source and hence dilation, density and viscosity affect the flow field that is studied in this work. Therefore, the simplification of the flame still permits to determine the flow field with its recirculation zones and flow instabilities [22, 196].

The size and quantity of the volumetric heat source were calculated from an undisturbed, adiabatic, one-dimensional, laminar flame model with detailed reaction kinetics. In case of the iron pentacarbonyl doped hydrogen/oxygen flame, the iron-oxide formation mechanism by Wlokas et al. [168] containing 27 reactions and 19 species was used. For the simulation of the acetylene flame, the reaction mechanism by Marinov et al. [209] was used, which contains 689 reactions of 155 species. The simulations of the one-dimensional flame were carried out with the chemical kinetics library Cantera [210]. The simulation of the one-dimensional flame

provided the temperature, species concentrations, transport and thermodynamic properties of the gas as a function of the flow path. The solution was used to determine the heat source (heat flux density) $\dot{Q}_c$ by evaluation of the steady state energy equation along the centreline:

$$\frac{d}{dx}(\rho u h) = \frac{d}{dx}\dot{q}_\lambda + \dot{Q}_c \tag{147}$$

In the above equation, ρ is the density, u the axial velocity, h the enthalpy and $\dot{q}_\lambda$ the diffusive heat transfer.

The equation is solved for $\dot{Q}_c$ using central finite differences. A similar approach was additionally published by Skovorodko et al. [196] for the estimation of the heat source in two-dimensional simulations of laminar flames.

The exhaust gas composition for the iron oxide synthesis and the sooting flame was determined by the mentioned one-dimensional calculations. Because the main product species remain nearly constant shortly after the flame, the calculated exhaust gas composition was constant in the simulations. The exhaust gas mixture was assumed to be an ideal mixture, where for each species the ideal gas model is valid. The thermodynamic properties of the pure species of the mixture were given as polynomial fits in NASA format [198]. The transport properties, the viscosity, and the heat conductivity of the mixture were calculated from the averaging formulas by Wilke [199]. The effect of particle transport on the flow field was neglected in all calculations due to the small particle sizes and concentrations.

Table 6-1: Operating parameters for measurements and simulations

	nanoparticle flame		**soot flame**
Parameters	Measurement	Simulation	Simulation
Pressure [mbar]	30	30	25
Composition (mass fraction)	$Ar/O_2/H_2$ (0.638/0.341/0.02)	$Ar/O_2/H_2O$ (0.638/0.17/0.192)	$Ar/CH_4/CO/CO_2/H_2$ (0.384/0.07/0.536/0.002/0.006)
Inflow velocity [m s^{-1}]	0.77	0.77, 1.54	standard 1.47, varied 0.4 – 2.4
Burner positions [mm]	50 – 200	50 – 200	
Geometry modification	quartz tube	quartz tube	quartz tube
Operation condition variants		He replaces Ar	
Flow direction	horizontal	horizontal, vertical	horizontal

Additionally, in case of the iron pentacarbonyl doped hydrogen/oxygen flame, a two-dimensional, rotationally symmetric model of the reactor geometry was simulated using a finite rate chemistry model and a reduced reaction mechanism [168]. In this calculation, the buoyancy was neglected, but the result was used to ensure the plausibility of the three-dimensional model, where the release of chemical energy was modelled as a volumetric heat source. Due to the low volume fraction of particles, the heat transfer by radiation could be

neglected in all simulations. With these simulations it was observed that radial diffusion does play a role for the investigated reactor setup due to the low Reynolds number and the low pressure.

The three-dimensional simulations were carried out with Ansys CFX using an implicit element-based finite volume method on an unstructured grid with the central differencing scheme chosen for the discretisation of the advection term. The simulated part of the reactor is sketched in Figure 6-13 and the three-dimensional volume of this domain is fully shown in Figure 6-17 for a burner position of 120 mm off the sampling probe. A three-dimensional mesh of hexahedral elements of 1 to 1.5 million nodes was generated for each geometry variant. The heat source that represents the flame was realized by a subdomain inside the main fluid volume. The outside of the reactor casing is cooled by natural convection that was represented by a constant heat transfer coefficient (α = 4 W/(K m^2)) for an ambient temperature of 300 K [211]. Heat conduction through the quartz tube was calculated coupled to the fluid flow solution. For the material properties of the quartz tube, its molar mass of 0.006 kg/mol, its density of 2201 kg/m^{-3} and its specific heat capacity of 1052 J/kg were used. Table 6-1 summarizes the investigated cases.

Additionally, one-dimensional simulations of the particle formation and growth along several streamlines within the reactor were performed to estimate the expected particle size at the sampling point. Therefore, the temperature and transport velocities were extracted as a function of the flow path from the three-dimensional simulations of the flow field. The particle formation and growth were calculated along these extracted paths in a post-processing step, which was possible due to the low volume fraction of the iron oxide particles (smaller than 10^{-6}). The iron oxide formation from iron pentacarbonyl in the low-pressure hydrogen/oxygen flame was described using the mechanism proposed by Wlokas et al. [168]. The particle growth through coagulation and coalescence was simulated using a method of moments with a locally-monodisperse size distribution for particle number concentration and diameter [125, 168]. (One should note that these simulations did not consider Brownian motion or potential flow unsteadiness.) Three one-dimensional, steady-state transport equations were solved using a fourth order Runge-Kutta method to calculate the particle formation and growth along the extracted streamlines: One transport equation for the monomer concentration n_0, one for the local particle number density N and one for the surface area A [125, 168]:

$$\frac{d}{ds}\left(u_s n_0 - D_0 \frac{d}{ds} n_0\right) = \mathrm{I} \tag{148}$$

$$\frac{d}{ds}\left(u_s N - D_p \frac{d}{ds} N\right) = \mathrm{I} - \frac{1}{2}\beta N^2 \tag{149}$$

$$\frac{d}{ds}\left(u_s A - D_p \frac{d}{ds} A\right) = I a_0 - \frac{A - A_{min}}{\tau} \tag{150}$$

In the above equations, u_s is the transport velocity along the streamline, D_0 and D_p are diffusion coefficients and β is the coagulation frequency [125]. The monomer concentration is calculated from the formation rate I of the Fe_2O_3 molecules. Hence, it is assumed that the particles are formed instantaneously. In Equation 150, a_0 is the surface area of a monomer and A_{min} the surface area of a completely fused (spherical) aggregate, which is the minimum surface area for a certain aggregate. The sintering time τ is calculated according to the particle diameter d_p, which is the ratio of the monomer volume and the particle surface area A in Equation 151. The constants for the following formula were estimated by Wlokas et al. [168] according to the data provided by Janzen and Roth [212].

$$\tau = 8 \cdot 10^{16}\, T\, d_p^4 e^{\left[-\frac{31.000}{T}\right]} \tag{151}$$

6.3.3. Results and discussion

To investigate the sudden increase of the measured particle sizes (Figure 6-15), the flow inside the reactor was calculated. The streamlines of the collected fluid sample are shown in Figure 6-18 for burner distances below and above the transition points. The illustrated streamlines were integrated backwards from the sampling point. Due to the very low inertia forces of the particles, the particles follow the flow; hence, the streamlines are a good representation of the particle trajectories, assuming that Brownian motion and potential flow unsteadiness can be neglected. The streamlines for burner positions of 100 mm and 120 mm are presented in Figure 6-18a and b, respectively for the setup without a quartz tube. For a distance of 100 mm from the burner (Figure 6-18a), the streamline reaches the sampling point directly, leading to a linear growth of the sampled particle residence time and size as a function of the burner distance. For a distance of 120 mm (Figure 6-18b), a long and twisted streamline is observed, therefore only fluid containing particles with an accordingly much increased particle residence time is sampled at the nozzle. Due to the large residence times, the particles can grow, coagulate and agglomerate leading to enlarged particle sizes. The inserted quartz tube directs the gas stream and so reduces the deflection as illustrated in Figure 6-18c and d for a burner position of 110 mm and 130 mm and shifts the point, from which recirculated gas is sampled by approximately 10 mm in axial direction – which agrees well with the point, from which bigger particles are observed (see Figure 6-15).

The buoyancy influence on the temperature field (burner position = 120 mm) is illustrated in Figure 6-19a for the cross section parallel to the burner axis and in Figure 6-19c for a cross section perpendicular to the burner axis at an axial position of 2 mm upstream of the sampling position that is located outside the main hot gas stream. The temperature distribution at the cross section parallel to the burner axis for a burner position of 50 mm is shown in Figure 6-19b. The flow is also asymmetric, but due to the smaller distance between burner and sampling point the deflection is lower and the main gas stream can reach the sampling

nozzle, as illustrated in Figure 6-19a and c. Due to the slightly different conditions, the temperature field differs from the measured temperature field (Figure 6-16) from the NO-LIF experiment. But the effect of buoyancy is comparable to our simulation results; the LIF measurements and the simulations agree on the strong buoyancy effect and the resulting asymmetric flow field.

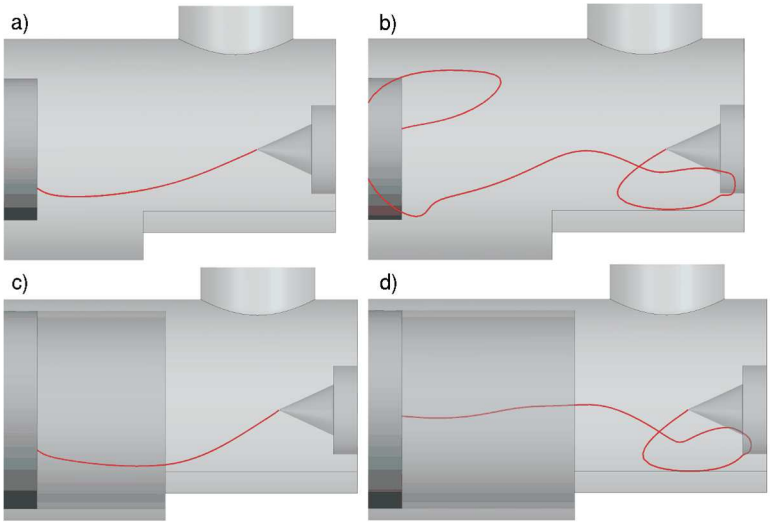

Figure 6-18: Examples of simulated streamline sampled at the nozzle for burner positions of a) 100 mm and b) 120 mm, and for burner positions with an inserted quartz tube of c) 110 mm and d) 130 mm. Reprinted from [22] with permission.

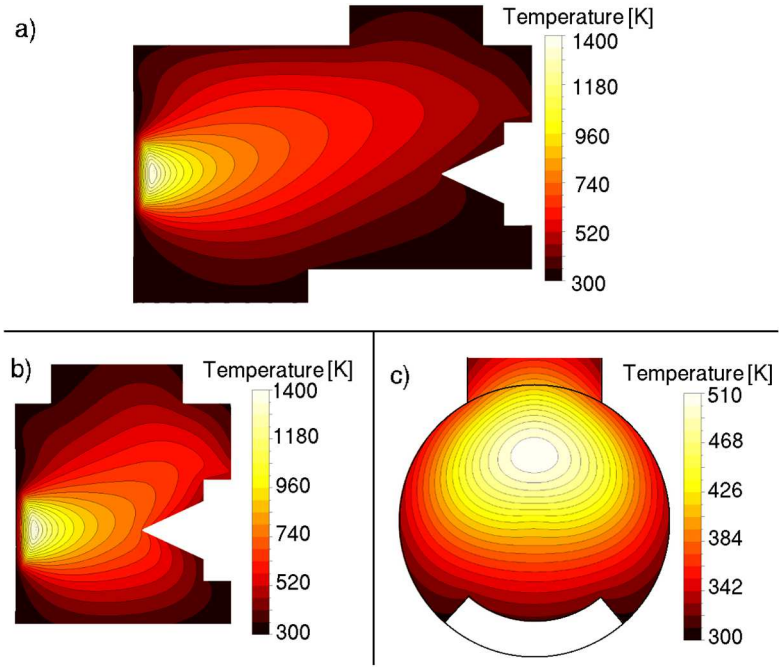

Figure 6-19: Simulated temperature distribution in a cross section parallel to the burner axis for a burner position of a) 120 mm b) 50 mm and c) axial cross section at 2 mm upstream of the sampling nozzle for a burner position of 120 mm. Reprinted from [22] with permission.

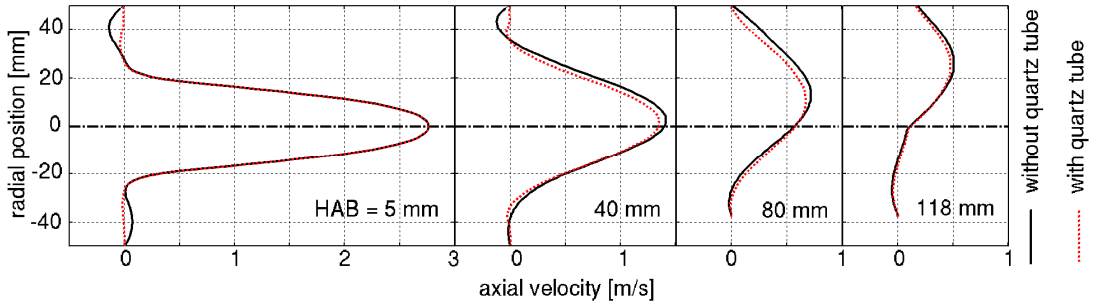

Figure 6-20: Simulated axial velocity distributions for different burner distances (5 mm, 40 mm, 80 mm and 118 mm) for a burner position of 120 mm. Reprinted from [22] with permission.

The axial velocity distributions at different distances from the burner of 5 mm, 40 mm, 80 mm, and 118 mm are shown for a burner position of 120 mm in Figure 6-20. With increasing burner distance, the maximum axial velocity is shifted in vertical direction; the influence of the quartz tube on the axial velocity distribution is negligible. To prevent the flow asymmetry, the burner must be moved closer to the sampling probe, so that meaningful data can only be obtained at relatively small distances from the burner.

The simulation results for iron oxide particle formation and growth are presented in Figure 6-21. Up to a burner distance of 110 mm, the simulated particle sizes correspond well with the results of the measurements performed in the reactor. Up to this sampling point, the particle paths from burner head to the sampling nozzle deviate only slightly from the path along the main reactor axis. Therefore, axis symmetric flow can be assumed for distances up to 110 mm from the burner (Figure 6-21).

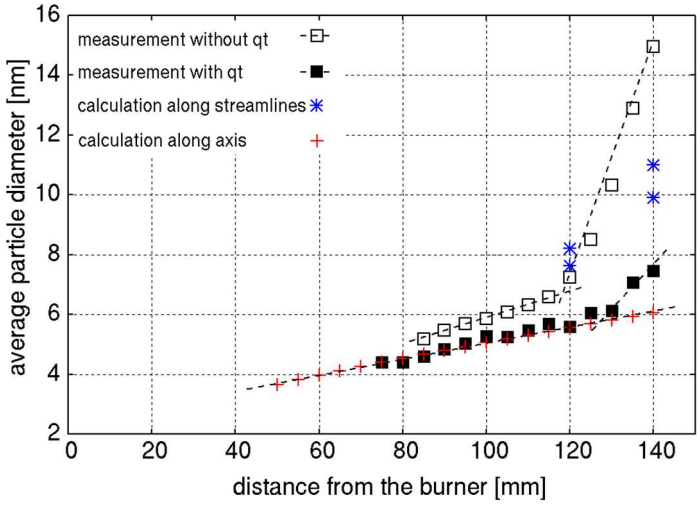

Figure 6-21: Measurement and calculation of the mean particle size. Measurements with (black filled) and without quartz tube (black). The particle sizes are calculated along the burner axis (red) and along two representative streamlines (blue) for a burner distance of 120 mm and 140 mm respectively. Reprinted from [22] with permission.

For sampling points above a distance of 110 mm from the burner, the particles follow flow paths through recirculation. The average particle diameter can be estimated from the same simulation approach, but the simulations can only be performed for a single streamline at a

time and are very sensitive to the precise path of the streamline inside the recirculation zone. Hence, the sizes of particles from the recirculation zone have a greater uncertainty than the sizes of particles that follow the straight path from the burner to the sampling nozzle.

For a distance of 120 mm from the burner, the particles follow a path with an average total length of 245 mm. The calculated particle diameter is 7.6 nm, which corresponds quite well with the measurements (7.24 nm). For sampling points further downstream, the range of path lengths and residence times spreads, leading to particle diameters in the range of 9.9 nm to 11 nm at burner distance of 140 mm (14.94 nm measured).

The simple model of particle dynamics, together with the CFD calculation of the three-dimensional flow field, was able to reproduce the kink in the measured average particle diameters, even if the absolute particle diameters still show a non-negligible deviation.

As the temperature and gas phase composition above a burner distance of 50 mm changes very slowly, the residence time remains the only plausible mechanism for the measured kink of the average particle diameter. From this study, it can be stated that for the development of particle formation models and their validation, only measurements of particles following the direct path from burner to the nozzle are usable and reproducible with desired certainty.

As seen in the shown cases, the analysis of the impact of buoyancy forces is essential to guarantee accurate results for nanoparticle synthesis and chemical investigations inside the reactor e.g. flame studies. The next paragraph describes an attempt to estimate whern buoyancy effects can be neglected and furthermore, how they can be reduced to provide direct advice for the experimentalists.

Methods to estimate and overcome buoyancy effects

To detect and avoid unwanted buoyancy effects, different modifications of the experimental setup have been tested. In Figure 6-22a-e, five methods are shown, for which the corresponding flow fields are presented. Some of these modifications are commonly used, but the principle of their operation and their efficiency are often not known or not well understood. The presented flow field for the different cases shows how the methods really work and the intensity of their buoyancy weakening effect. This flow analysis also helps to rate all modifications to support the experimentalists to find the best case for their purpose.

First, the simulated reactor was rotated by ±90° to face up- or downwards. The vertical setup ensures a symmetric flow field as illustrated for the iron oxide nanoparticle synthesis flame by the temperature distributions shown in Figure 6-22a and b. The upward orientation represents the ideal case due to the symmetric and directed flame, which is spreading at a lower rate than for the downward orientation. Due to the assembly and the fixture of the measurement devices or attributed to spatial circumstances, it is often not possible to rotate the reactor to a vertical position; so different procedures to minimize the buoyancy effect in a horizontal setup have to be found. The inflow velocity was increased to 2 m/s, resulting in a symmetric temperature

distribution with a negligible buoyancy effect similar to the ideal vertical case, as shown in Figure 6-22c. However, for kinetics studies a high velocity is not always suitable as for the desired long residence time the sampling distance would also have to be increased.

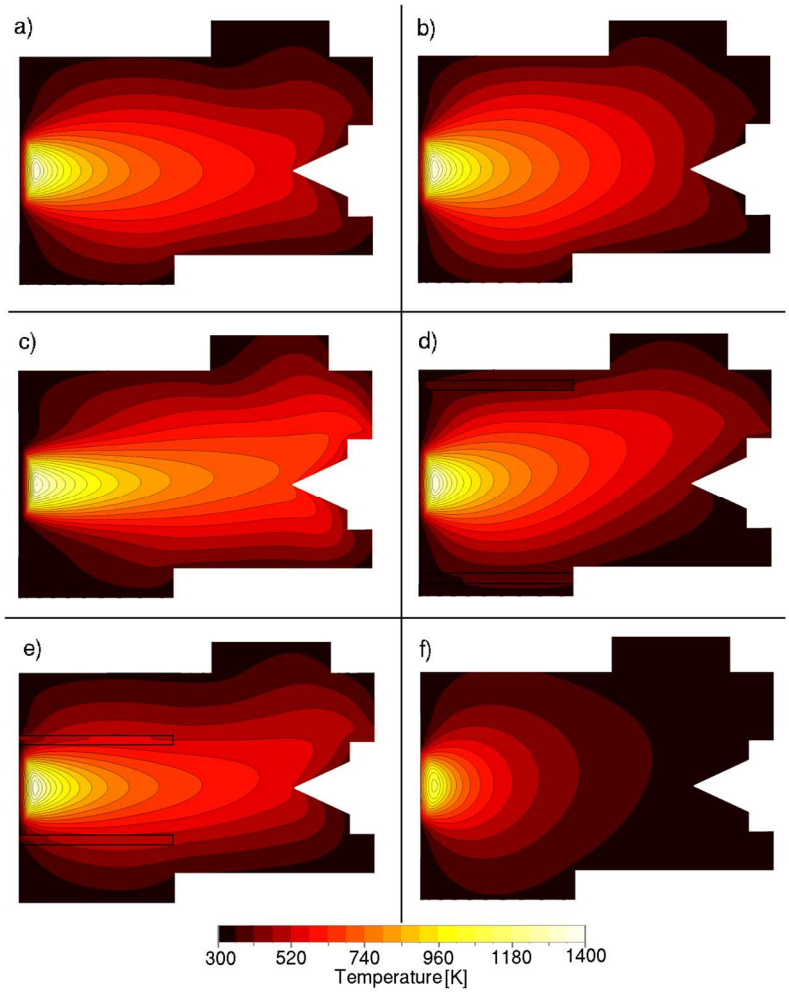

Figure 6-22: Simulated temperature distribution for burner position of 120 mm with a) bottom-up flow, b) top-down flow, c) increased (2 m/s) inlet velocity, d) added broad and e) narrow quartz tube, and f) helium replacing argon. Reprinted from [22] with permission.

A different approach to reduce the buoyancy effect places the mentioned quartz tube inside the reactor. This tube reduces the effective chamber diameter to redirect the hot gas stream and insulate the flow from the cold reactor casing and hence prevents cooling and recirculation of the gas. The relatively large tube diameter that was used in the experiments (0.84 × diameter of the reactor chamber) does not achieve a major improvement regarding the redirection. The thermal insulation effect of the tube is not visible in the temperature distribution (Figure 6-22d) and has a negligible impact for this burner distance. But for even larger burner distances, this insulation will have a wider influence and will be presented and discussed later for the sooting flame. The flow field for the inserted quartz tube in Figure 6-22d is still asymmetric. A tube with a smaller diameter (0.42 × diameter of the reactor chamber, 0.5 × diameter of the tube of the experiments) directs the hot gas in the axial direction and hence minimizes the deflection as it can be seen in Fig. 8e. Furthermore, the

buoyancy effect could be reduced by replacing the diluent gas argon by the same mass fraction of helium that has a smaller volumetric thermal expansion. The resulting temperature distribution for the iron oxide synthesis, illustrated in Figure 6-22f, is more symmetric than for the argon case (Figure 6-19a).

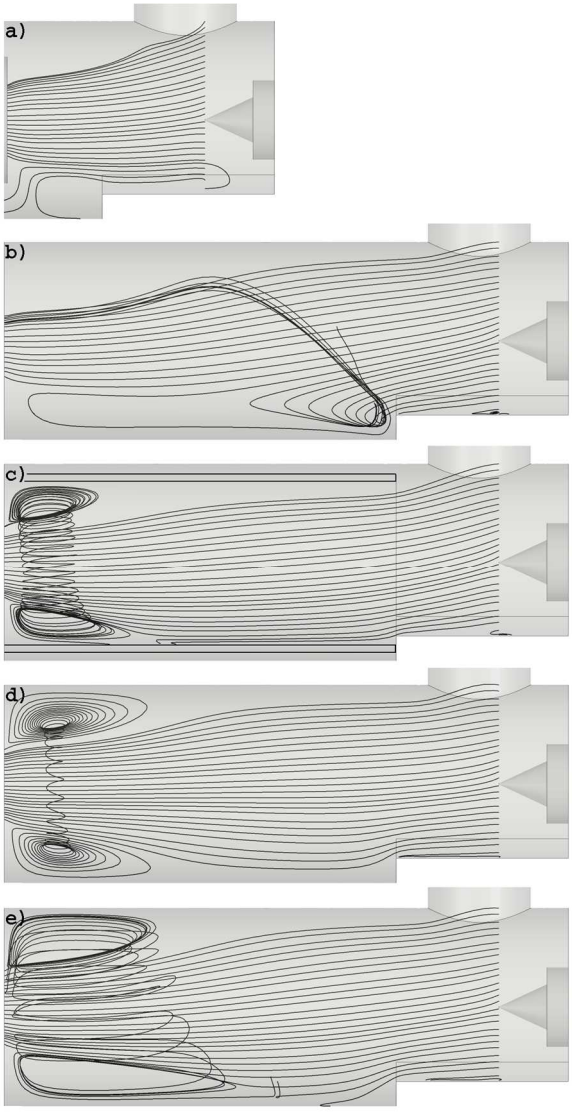

Figure 6-23: Simulated streamlines within the reactor chamber for burner positions of a) 100 mm, b) 250 mm, c) 250 mm with quartz tube, d) 250 mm with insulated reactor wall and e) 250 mm with a heated reactor wall of 400 K. Reprinted from [22] with permission.

Buoyancy effects can also be reduced by placing the burner closer to the sampling point – but at the cost of reducing the particle residence time.

The reactor windows can be flushed with argon, the effect of which was examined by comparing a simulation with and without flushing. No influence was found on the deflection of the main gas stream by buoyancy.

For the sooting flame, the flow field is illustrated for two burner positions by the 3D streamlines that end at the axial position of the sampling orifice in Figure 6-23a and b. The displayed streamlines are integrated backwards from the axial plane at the sampling nozzle.

Figure 6-23c shows the equivalent streamline plots for the case with the inserted quartz tube and Figure 6-23d and e with an insulated and heated reactor respectively.

For a small distance between burner and sampling probe, the flow can reach the sampling orifice directly so that 'new grown' particles can be detected. For larger distances, the flow is deflected as shown in Figure 6-23b, so that most of the hot gas leaves the reactor above the sampling orifice. The combustion products rise up to the top wall of the reactor, where they cool down and increase density, so that they drop again along the reactor side walls towards a recirculation zone at the bottom of the reactor, from which the fluid will finally reach the sampling point. For a burner position of 250 mm, with an inserted quartz tube, the gas cooling at the walls is reduced by the quartz tube: due to its relatively large diameter, the impact of the tube cannot be attributed to a redirection of the hot gas stream, as it is most commonly assumed, but to the thermal insulation, which avoids the cooling and sinking of the gases towards the bottom of the chamber. The similar improvement could be achieved by insulating or heating the reactor wall, shown in Figure 6-23d and Figure 6-23e respectively, albeit at a higher effort. For all cases shown in Figure 6-23, a recirculation exists right after the inlet, but the recirculation does not deflect the main gas stream and has no influence on the sampling.

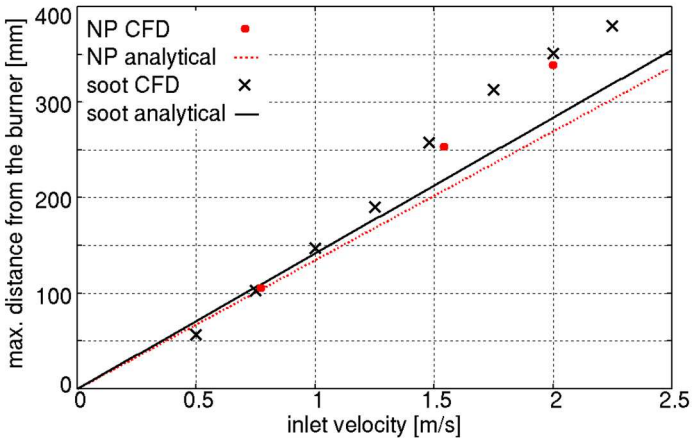

Figure 6-24: The analytically estimated and simulated maximum distance from the burner for sampling for meaningful PMS measurements of soot and iron oxide nanoparticles (NP). Reprinted from [22] with permission.

To avoid the detection of particles, which have experienced an extended residence time as a result of the deflected gas stream, the limiting conditions for the "meaningful" use of gas sampling and PMS must be determined. The maximum distance from the burner for the sampling location, for which buoyancy does not affect the measurements, was calculated for the sooting acetylene flame and the nanoparticle flame with the use of simulations and analytically. With the help of simulations, the maximum permissible distance from the burner was defined by determining the maximum range of the main gas stream on the middle axis of the reactor (radial position of the sampling nozzle). This maximum axial range is reached by the bottommost hot gas stream with a radial deflection of the value of the burner radius *r*. The time *t* for this radial deflection of the gas stream can be estimated analytically by a force

balance equation for the fluid. With that time, the maximum burner distance d_{bmax} can be expressed as a function of the axial velocity of the burnt gas u_b and the equation for the analytical approximation of d_{bmax} is:

$$d_{bmax} = \boldsymbol{u_b}\ t = \boldsymbol{u_b}\ [2\ r\ \rho_b\ /(\boldsymbol{g}\ (\rho_u - \rho_b))]^{1/2} \tag{152}$$

In the above equation, $\boldsymbol{g}$ is the gravitational coefficient and ρ_b the density of the burnt gas and ρ_u the density of the unburned gas, with

$$\rho_{u/b} \sim 1\ /[T\ (\sum_i\ y_i\ M_i)] \tag{153}$$

T is the temperature of the gas mixture, y_i the mass fraction of the species and M_i the species' molar mass.

The maximum burner distance is plotted for both methods as a function of the inlet velocity in Figure 6-24. Below an inlet velocity of 1 m/s, the simulated and calculated results correlate very well. For higher velocities, the simulation provides higher maximum burner distances due to the upper reactor wall limiting the deflection of the hot gas stream, which was not considered in the analytical calculation. The measured particles reach the sampling point up to the corresponding maximum burner distance on a direct path, which ensures appropriate particle detection. Due to the relationship of inlet velocity and permitted distance from the burner, a maximum residence time can be computed. In the present setup, particle growth can only be examined up to a residence time of 0.114 s to 0.178 s. Similar constraints apply and can be estimated analytically for all measurements in horizontal flat flame reactors.

It is stressed that the observations from this preliminary study can be transferred to other flame reactor experiments that are used for soot formation studies, nanoparticle synthesis, determination of reaction rates and other topics of flame investigation.

Due to this study, all reactors within the NETZ building were adjusted vertically. Additionally, this work has led to publications in Combustion Theory and Modelling [22] and to several contributions to different conferences.

7. Modelling of the spray synthesis process

The modelling of a spray flame synthesis process was performed for a laboratory-scale spray flame reactor (Tethis S.p.A.), which is used by many groups to investigate the production process of high specific metal-oxidic nanomaterials, including the groups of Peukert at the FAU Erlangen [213, 214], Pratsinis at the ETH Zurich [9, 14, 215] and at the University of Duisburg-Essen by the group of Schulz and Wiggers [216-218]. In this work, the synthesis of TiO_2 is examined. TiO_2 nanoparticles are used for many applications and have a worldwide annual consumption of more than three million tons [219]. A commonly used precursor for titania synthesis is $TiCl_4$, for which chlorine and hydrogen chloride arise and have to be treated. Therefore, an alternative is the liquid precursor titanium tetraisopropoxide (TTIP), which can be used, due to its good solubility in alcohols, in a spray-flame assisted synthesis process. The nanoparticle properties are affected by three main processes: a) the break-up of the liquid jet from the spray nozzle, b) the combustion, of the spray and in the pilot flame and c) the formation and growth of the nanoparticles. The properties of the spray defined as droplet size distribution, velocity, spray angle and break-up height influence the flame propagation and the spray combustion. Therefore, these characteristics had to be determined initially. There are many studies, which deal with liquid jet break-up processes and spray formation [46, 220], for low gas velocities around the jet and neglect nonlinear effects of liquid distortion, turbulent effects and the influence of the shear layer between the liquid and the gaseous phase. For high liquid velocities, many studies do exist, but they are mostly for spray formation under engine conditions, where the pressure and the Reynolds and Weber numbers are much higher than in the investigated nozzle. Droplet dynamics for a flame spray process for the synthesis of ZrO_2 from zirconium n-propoxide were already measured by Heine et al. [221] for a similar reactor setup. They have measured the droplet velocity distribution along the centreline by phase Doppler anemometry (PDA). However, due to the different material system, different operating conditions and slightly different nozzle setup, the measurement results are not comparable to the nozzle investigated in this thesis. Due to the missing experimental data for the used reactor nozzle, the spray properties are unknown and cannot be estimated analytically. Therefore, the spray characteristics of the primary liquid jet break-up were determined by Volume of Fluid (VOF) simulations and experiments to provide the boundary conditions, which are needed for further modelling of the combustion and nanoparticle formation process.

In this chapter, the experimental reactor setup is introduced, which is followed by a description of the physical processes within the reactor. For these processes, the modelling approach and the determination of the boundary conditions are explained and the results are shown and discussed. Some parts of this chapter have already been published by Weise et al. [217] and are reprinted with permission.

7.1. Experimental setup

The reactor setup (Tethis S.p.A.) is modified by an additional cylindrical stainless steel housing (d = 265 mm, l = 280 mm), which enables the pressure to be controlled between 200 mbar and 2000 mbar and avoids polluting the laboratory through nanoparticle exposition. Figure 7-1 shows the assembly drawing of the reactor housing. The reactor inlet and the three main processes within the reactor; spray breakup, turbulent combustion and nanoparticle formation, are sketched in Figure 7-2. The main processes are illustrated one by one for clarity, but they may interact and appear simultaneously.

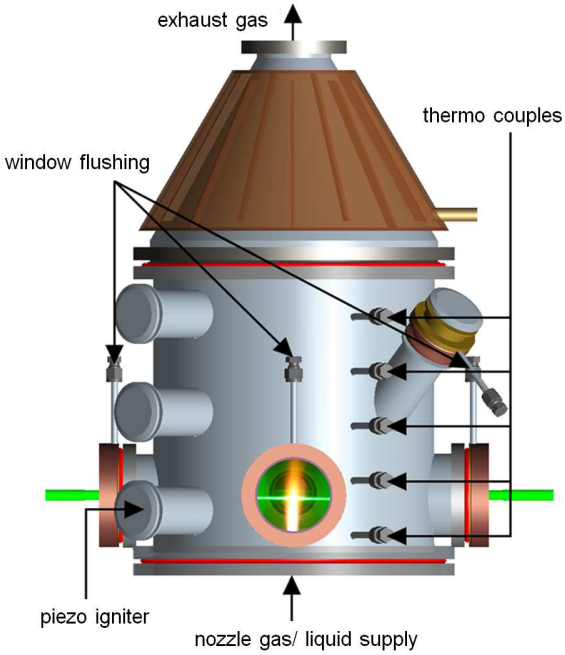

Figure 7-1: CAD drawing of the reactor housing [222].

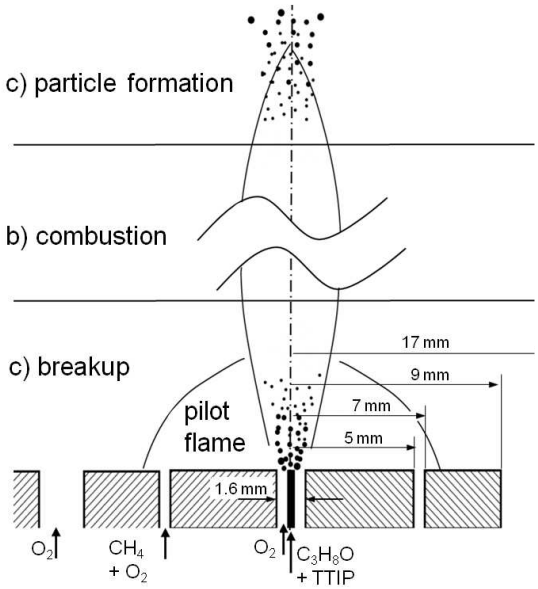

Figure 7-2: Reactor inlet and process steps within the reactor. Reprinted from [217] with permission.

The liquid precursor TTIP is dissolved in the liquid fuel isopropyl alcohol (C_3H_8O) and is injected through a hollow needle with an inner diameter of 0.3 mm and outer diameter of 0.7 mm, respectively. An annular gap with a diameter of 1.6 mm supplied the oxygen dispersion gas. The dispersion gas atomizes the liquid jet causing it to break up and form a spray. The described nozzle is an external mix two-fluid nozzle. Its design aims to cool the incoming liquid to prevent premature formation of nanoparticles at the injector and hence to avoid clogging of the nozzle. The reactor operated at 1 bar and an amount of 5 ml/min C_3H_8O with 0.5 ml TTIP per litre C_3H_8O was inserted through the nozzle. The oxygen dispersion gas flow was 5 standard litres per minute (slm).

Within the reactor, the liquid isopropyl alcohol droplets of the spray evaporate and form a gaseous fuel. This fuel mixes with the oxygen from the spray nozzle and is ignited by a pilot flame. Hence, TiO_2 molecules are formed from the thermal decomposition of TTIP. The pilot

flame, used for the ignition and stabilization of the spray flame, is a premixed methane-oxygen flame. For the pilot flame, 0.5 slm methane and 1.2 slm O_2 are inserted through an annular gap that has an inner and outer diameter of 10 mm and 10.4 mm, respectively.

Within the spray flame, nanoparticles are formed from TiO_2 molecules through nucleation. These particles then increase in size due to surface growth, coagulation, and agglomeration.

Additionally, a co-flow of O_2 is inserted through an annular sintered matrix at the bottom of the reactor. This matrix has an inner and outer diameter of 18 mm and 34 mm, respectively. The co-flow provides additional oxygen for the combustion processes and shields the reactor walls and the optical windows from particle deposition. The reactor was operated with a co-flow of 4 slm. A quenching gas was also inserted to control the reaction processes and to avoid condensation of water, which is formed during the combustion process on the reactor walls. The quenching gas was 150 slm nitrogen.

As already mentioned above, the unknown spray properties were determined using VOF simulations and experiments. For the experimental part, shadowgraphy imaging was conducted by the Schulz' group (by Jan Menser) to determine the spray cone angle and the mean droplet velocity. Additionally, the shadowgraphs also served to check the findings of the VOF simulations. The cone of the spreading liquid jet near the nozzle and the originating spray were illustrated by shadowgraphy imaging. Therefore, a short-pulsed LED lighted up the near-nozzle zone to freeze the motion of the liquid and droplets. This was done with a high-power LED, which illuminated a diffuser screen with sequences of red-green-blue (RGB) pulses, with 2 µs duration respectively, at 20 µs intervals. The spray projected a shadow onto the coloured diffuser screen, which was captured by a consumer camera (Nikon D5100). The three colours of the LED pulses were assigned to the colour channels of the camera sensor. The droplet velocity was calculated by particle tracking velocimetry (PTV), where a cross correlation of the droplet shift between the three RGB-channels provided the droplet velocity field. The same camera was used to determine the spray angle. For a better contrast, the spray was illuminated sideways with a white LED flashlight with an exposure time of 1/1250 s (ISO 3200, F/10).

Flame imaging was done for a qualitative cross check of the simulation results and to show the shape of the turbulent flame. Snapshots with a short exposure time (1 µs) were taken with an image-intensified camera to provide insight into the instantaneous combustion and flow field of these flames, and to provide an estimate of fluctuation levels. A mean of all snapshots showed the Reynolds averaged shape of the flame.

7.2. Modelling

The synthesis process is affected by the spray formation and the turbulent combustion process. Therefore, a modelling is quite challenging as the coupling of these processes has to be considered. In the next three subchapters, the strategy for the determination of the boundary conditions and the simulation approaches are described.

The primary break-up process of the emanating liquid fuel and precursor jet was calculated using a Volume of Fluid method (VOF). For the simulation of the turbulent combustion and the nanoparticle synthesis four different simulation methods were employed, which are summarized in Table 7-1. The PaSR01 case applied the PaSR method for the combustion modelling and solved the PBE model directly with an Euler-Euler approach. In this case, CH_4 was used for the pilot fuel and C_3H_8O for the spray. This modelling approach was also used for sensitivity studies to investigate the influence of the droplet characteristics on the flame and the final nanoparticle size distributions.

Table 7-1: Overview of the combustion and PBE simulations and the models used

	Fuels	**Combustion modelling**	**Calculation of the PBE**	**Turbulence - PBE closure?**
PaSR01	CH_4, C_3H_8O	PaSR model	Euler	no
PaSR02	C_3H_8O	PaSR model	Euler	no
EBU	C_3H_8O	EBU model	Euler	no
MC	C_3H_8O	EBU model	Lagrangian Monte Carlo particles	yes, Lagrangian PDF

Additionally, the PaSR model was used to calculate the reactor operating with C_3H_8O as pilot fuel instead of CH_4 (PaSR02) to investigate the influence of the pilot gas fuel on the flame and the nanoparticle characteristics. This case was performed as a validation to warrant that the substitution of the pilot fuel with C_3H_8O does not affect the spray flame and hence the particle characteristics for further simulations with the EBU model.

The EBU case used also an Eulerian approach for the modelling of the PBE, but with the EBU concept for the combustion simulation. For this case, the population balance model was solved as a post-processing step. For the MC case, the combustion was also modelled with the EBU concept, but for the modelling of the PBE a simplified hybrid Lagrangian Monte Carlo method was applied (see chapter 4) to consider the turbulence-particle dynamics interaction.

For a cross check of the simulation, the results were compared to the shadowgraphy imaging of the spray and luminescence imaging of the flame. All methods are subsequently discussed in detail.

7.2.1. Break-up and spray formation

The VOF method is used to model the primary break-up of the liquid jet emanating from the spray nozzle within the investigated spray flame reactor. The simulations provided the diameter distribution of the droplets that evolve through primary break-up as boundary conditions for further calculations.

The VOF simulations were performed to estimate the mean break-up height and the droplet diameter. The cylindrical calculation domain for the VOF simulations had a diameter and a height of 4 mm. Three simulations were performed: one with laminar inflow conditions, one with additional grid adaption for the liquid-gas interface and one with pseudo turbulent inlet conditions and grid adaption. The grid adaption featured a local grid spacing of 0.015 mm. The total physical time that was simulated was 10 ms. After 3 ms, the primary break-up process was established and the size distribution for the droplets could be estimated.

It must be mentioned that the performed VOF simulation is not a direct numerical simulation (DNS). A DNS of the break-up process for such high Reynolds numbers requires more computational effort and also more accurate modelling as for example done by Desjardins et al. [223] with VOF-level set hybrid schemes. Another approach for a precise simulation of the break-up would additionally require a coupling of VOF and Lagrangian particle tracking to ensure full mass conservation [224] or other advanced methods as outlined in 2.4.2, albeit with higher modelling efforts. The VOF simulations in this work should only provide an estimation of the droplet diameter distribution as boundary conditions for the nozzle. Therefore, the sensitivity of the further simulations (combustion and nanoparticle formation) on the estimated droplet diameter distribution is validated by a parameter study. Additionally, the influence of pseudo transient turbulent inflow conditions on the droplet size distribution was tested.

Similar to the shadowgraphy approach, the VOF simulations delivered a good estimation for the nozzle boundary conditions. However, for the spray angle and the droplet velocity a parameter study was also done to ensure that the spray flame and the nanoparticle formation process are insensitive to potential errors and deviations in the spray properties. Additionally, the influence of the droplet dispersion on the flame and the nanoparticle properties was analysed.

7.2.2. Turbulent combustion

The flow within the reactor is mainly laminar, only the oxygen gas stream of the spray nozzle has a Reynolds number of 5000 due to the small inlet diameter. The cylindrical three-dimensional simulation domain had a height of 150 mm and a diameter of 40 mm. The spatial discretisation was realised with a hexahedral mesh with 330,000 elements, which was generated using the OpenFOAM mesh generator snappyHexMesh.

The very small gap (0.2 mm) of the pilot and dispersion gas inlets would require a very fine grid resolution. The small grid spacing together with the high local velocities of the pilot and dispersion gas result in small time steps due to the CFL condition. Small time steps lead to long calculation times and hence to high computational costs. Therefore, the calculation domain was translated by 2.5 mm above the nozzle, where, due to the spreading of the gas stream, wider annular inlet gaps and lower velocities could be realised. Additionally, at this height above the nozzle, the required spray boundary conditions were applied from the VOF simulations and the shadowgraphs.

The transient simulations were performed using a second-order central differencing scheme, implicit time discretisation and the PISO algorithm for the coupling of pressure and velocity (see chapter 5). The spray was modelled with an Euler-Lagrange approach with a two-way coupling of gas and liquid phase as described in chapter 2.4.2.

The simulation of the combustion of the evaporated fuel and precursor and the pilot gas was realised with two different approaches: with the Partially Stirred Reactor concept (for the cases PaSR01 and PaSR02) and with the Eddy Break-Up model (for the cases EBU and MC), as shown in Table 7-1. Both models are explained in chapter 2.5.2 and 2.5.3, respectively. The model constant C_R and C_R' (Equation 74) are set to 0.6 and 15, respectively.

The reaction process of the premixed methane combustion was calculated with the one-step reaction mechanism by Westbrook and Dryer [225] for the PaSR01 simulation. For the EBU simulation, isopropyl alcohol was used for the pilot gas mixture instead of methane, because the model can only handle one fuel species. The amount of isopropyl alcohol in the pilot gas mixture was therefore adjusted to yield the spray flame shape and temperature. This was validated performing an additional PaSR simulation using C_3H_8O as pilot fuel and comparing the results with the case PaSR01. For the combustion of isopropyl alcohol, a mechanism was applied using the formalism described by Westbrook and Dryer [225] in analogy to ethanol combustion. The reaction rates were determined from the irreversible Arrhenius approach $k_f = A\,T\,exp[-T_A/T]$. The pre-exponential factor A and the activation temperature T_a are shown in Table 7-2 for all reactions.

Table 7-2: Reaction mechanisms

Reaction	**A[s^{-1}]**	**T_A[K]**
$C_3H_8OH + 4.5\ O_2 = 3\ CO_2 + 4\ H_2$	1e14	500
$CH_4 + 2\ O_2 = CO_2 + 2\ H_2O$	2.199e8	2516
$C_{12}H_{28}O_4Ti = 2\ H_2O + 4\ C_3H_6 + TiO_2$	3.96e5	8487

7.2.3. Nanoparticle dynamics

The TiO2 nanoparticle formation and growth was calculated using a modified monodisperse model by Kruis et al. [125] as described in chapter 3.3.2 for all three cases.

For the reaction of TTIP, there are mainly three routes for the transformation to TiO2: hydrolysis, thermal decomposition and surface growth [124]. Since the hydrolysis reaction path [226] was developed for moderate temperatures (673 K), Tsantilis et al. recommended that this reaction "should be treated with caution" [124]. Hence, for the present high temperature conditions (~2300 K), this uncertain reaction was neglected. Tsantilis et al. [124] have also shown that the conversion of TTIP to TiO_2 is not influenced by surface growth and dominated by thermal decomposition, which is therefore considered as the main route for the formation of TiO_2 particles in this work. The thermal decomposition of TTIP was calculated with the one-step mechanism by Okuyama et al. [227], shown in Table 7-2.

For the approaches PaSR02 and EBU, the PBEs are modelled with an Eulerian method with Reynolds averaged values of temperature and nucleation source term. In the transport equations for the particle number, surface area and volume concentration, an additional convection and diffusion term is added on the LHS to account for the nanoparticle motion due to diffusion and convection. The equation for the particle number concentration N then reads (the equations for A and V are adjusted analogously):

$$\frac{\partial N}{\partial t} + \nabla \cdot \left(N\bar{\boldsymbol{u}} - D_p \bar{\boldsymbol{u}}\right) - = -\frac{1}{2}\beta N^2 + I$$

The diffusion coefficient D_p is calculated from Equation 105 and $\bar{\boldsymbol{u}}$ is the Reynolds averaged velocity.

For the method PaSR01, the PBEs are modelled coupled with the spray combustion, where the TTIP decomposition is also calculated with the PaSR concept. For the EBU simulation, the particle dynamics are calculated in a post-processing step, because the EBU model can only handle one fuel species. The temperature, pressure, velocity and density fields are taken from the previous spray combustion simulation and kept constant, because the conversion of TTIP does not affect the flow field within the reactor. In the post-processing step, the TTIP decomposition is then calculated with an Arrhenius approach and the PBEs are solved with an Eulerian approach.

For the MC approach, the instantaneous temperature and nucleation source term are calculated with a simplified hybrid Lagrangian Monte Carlo approach. The PBEs are solved for the Monte Carlo particles, which can themselves be considered as small homogeneous reactors. Each Monte Carlo particle is a parcel, which represents a certain amount of gaseous molecules. It again must be stressed that Monte Carlo method applied in this work is only a simplified method. The Monte Carlo particles only change their mixture fraction one-way with a constant Eulerian field. The precursor mass fraction is only carried by the Monte Carlo

particles, which emerge due to fuel evaporation and is not exchanged by the Monte Carlo particles. This model is only a first step towards the full closure of the turbulence-particle dynamic interaction. The full approach was already described in detail in chapter 4.

7.3. Results

7.3.1. Break-up and spray formation

The droplet diameter distribution was determined by the VOF simulation results at a height of 2.5 mm above the nozzle, because the simulations and the experiment show that the primary break-up of the jet was established beyond this distance. The LHS in the snaphots in Figure 7-3 shows the analysis plane with the cross section of the passing droplets for one time step. The RHS in each figure illustrates the corresponding isovolume of the liquid-gas volume ratio of 0.5 and the location of the analysis plane for the same time step as for the analysis plane.

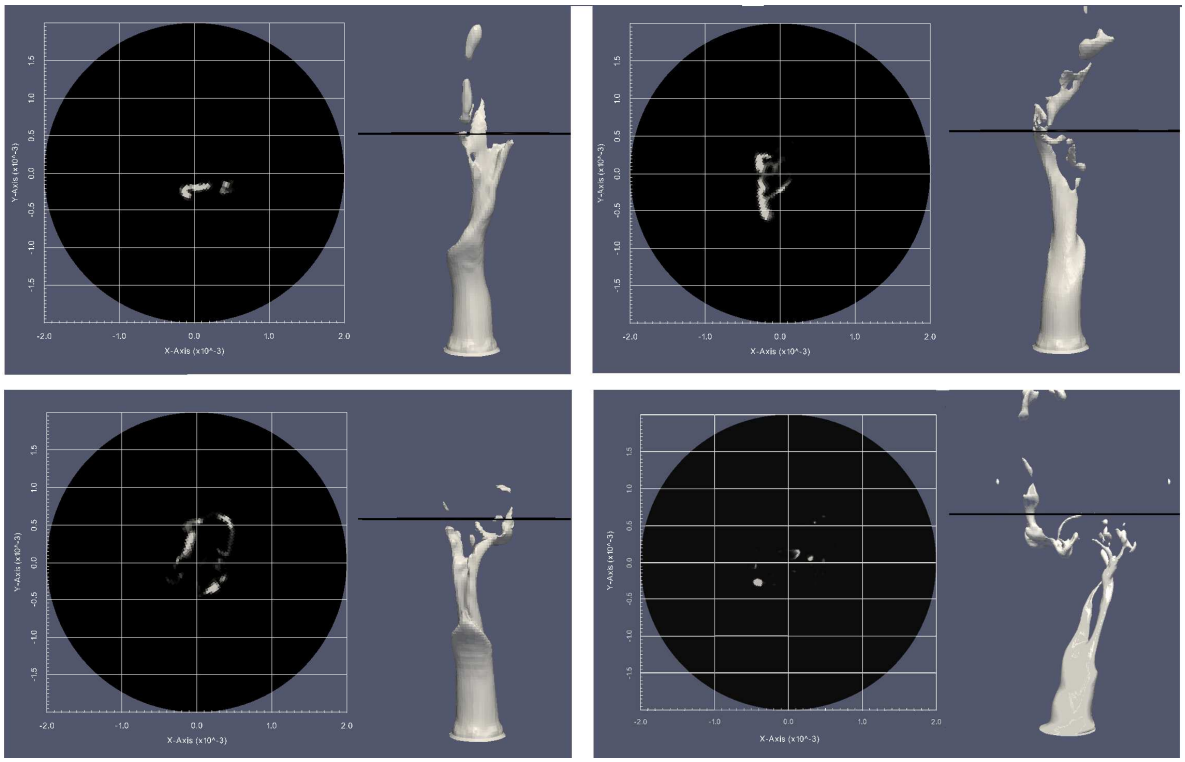

Figure 7-3: Analysis plane for the determination of the droplet diameter distribution (left) and the liquid phase with the location of the analysis plane (right) for different time steps.

The droplet diameters were determined for three cases: for laminar inflow conditions with and without a dynamically refined grid, and pseudo turbulent transient inflow conditions with grid adaption. The droplet size distribution was adjusted to the cumulative Rosin-Rammler distribution [228], which features the parameters d_{mean} = 80 µm and n = 1.8 (for the dynamical grid refinement):

$$R_{CFD} = 1 - exp\left[-\left(\frac{d}{d_{mean}}\right)^{n}\right] \tag{154}$$

Figure 7-4 shows the cumulative Rosin-Rammler distribution for all three cases. It can be seen that the artificial turbulent inflow conditions have a negligible influence on the droplet diameter distribution. The dynamically refined grid for the turbulent inlet conditions provides a slightly different distribution, but the mean droplet size is hardly affected. For the examination of the sensitivity of the flame and the nanoparticle formation on the initial droplet diameter distribution, further simulations were done for the smallest (d_{mean} = 80 µm, n = 1.8) and the largest (d_{mean} = 120 µm, n = 1.2) size distributions.

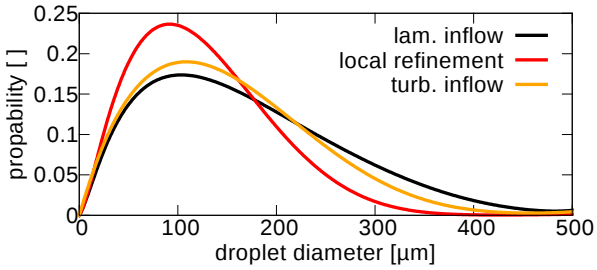

Figure 7-4: Simulated (VOF) droplet diameter distribution 2.5 mm above the nozzle for laminar inflow with and without local refinement and for artificial inlet turbulence. Reprinted from [217] with permission.

One sequence of the shadowgraphs for the RGB-pulses is shown in Figure 7-5. The mean droplet velocity was determined at the same distance from the nozzle as the droplet diameters (2.5 mm downstream). The flight distances of the droplets were measured between many snapshots resulting in a mean droplet velocity of 20 m/s.

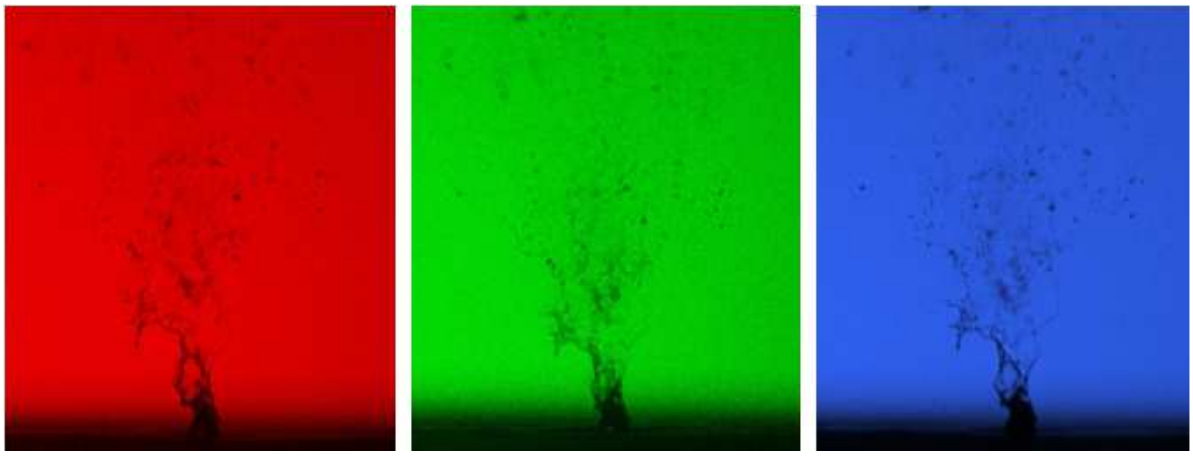

Figure 7-5: Shadowgraphs by high-power LED with a sequence of red, green and blue pulses (20 µs interval).

For a cross-check of the simulation, the colours of the shadow pictures were inverted and these results were layered. This image is compared to a corresponding rendering of the simulated primary break-up in Figure 7-6. The experiment (Figure 7-6a) shows finer

structures than the simulated (Figure 7-6b) jet break-up. However, the simulation and the experimental results agree well in the break-up process: The jet sways away from the centreline due to the high velocity of the annular dispersion gas flow, it breaks up into filaments and further into droplets. Both show a similar break-up height and the same displacement and sway amplitude of the liquid droplets.

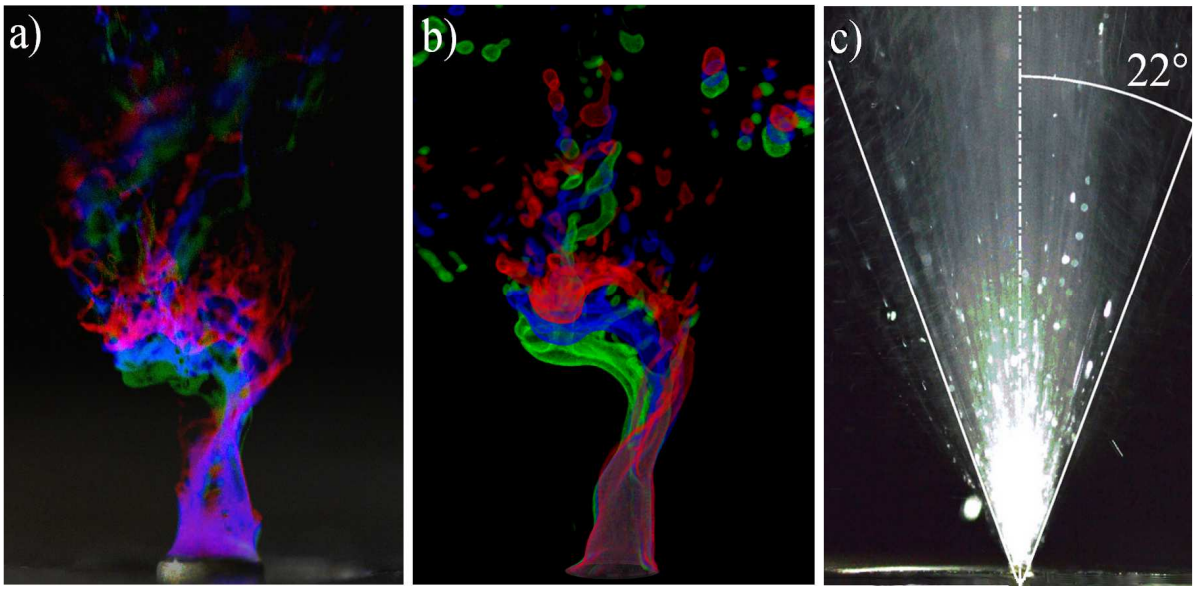

Figure 7-6: Liquid jet break-up for a) RGB-shadowgraphy imaging and b) corresponding rendering of the simulation; the interval between the colours is 20 µs and c) determination of the spray angle from imaging (size 15.5 x 20 mm, exposure time 0.8 ms). Reprinted from [217] with permission.

The experiments also provided the spray angle: The image with the white LED illumination, illustrated in Figure 7-6c, shows a spray angle, which was measured to be 22°.

For the sensitivity analysis, additional simulations (with the PaSR01 approach) were done for a mean droplet velocity of 10 m/s, a spray angle of 15° and without droplet dispersion. An overview of the droplet characteristics used for the parameter studies is summarized in Table 7-3.

Table 7-3: Droplet characteristics for the reactor simulations.

case	**Rosin Rammler parameters** (d_{mean} [µm] , n [-])	**average velocity [m/s]**	**spray angle**	**dispersion**
standard	80, 1.8	20	22°	yes
large d	120, 1.2	20	22°	yes
low vel.	80, 1.8	10	22°	yes
15° angle	80, 1.8	20	15°	yes
no dispers	80, 1.8	20	22°	no

7.3.2. Turbulent combustion

This chapter presents the results for the four simulations shown in Table 7-1. The results of the case PaSR01 were already published by Weise et al. [217] and reprinted with permission.

PaSR01

The spray flame luminescence image (exposure time 0.4 µs, in Figure 7-7a) shows the instantaneous partially turbulent structure of the flame. The mean image in Figure 7-7b shows the time-averaged flame shape. The simulated temperature field of the flame is illustrated in Figure 7-7c on the longitudinal cross section of the reactor. The high pilot flame temperature results from the combustion with pure oxygen. The experimental images and the simulation result show qualitatively the same flame shape.

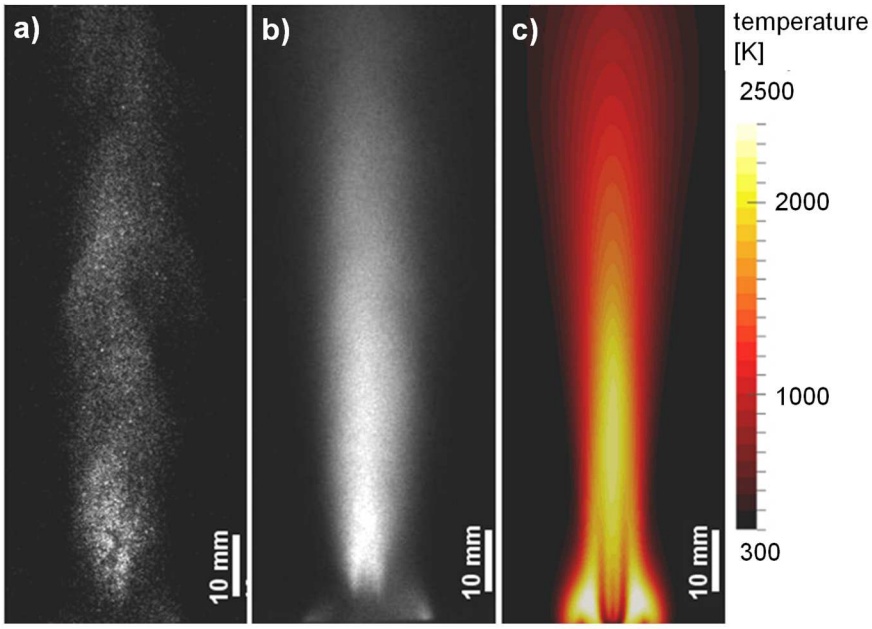

Figure 7-7: Photography and simulation of the flame a) snapshot with 400 ns exposure time, b) mean of the snapshots, and c) simulated temperature field. Reprinted from [217] with permission.

The axial gas phase velocity along the centreline is shown in Figure 7-8a for the standard case (dispersion, 22° spray angle, small droplets, mean droplet velocity of 20 m/s). The axial velocity drop directly after the liquid injection is caused by the slower droplets. The temperature along the centreline is illustrated for all spray boundary settings in Figure 7-8a, where the influence of the droplet characteristics on the temperature is negligible, only the case without dispersion shows a slightly higher temperature at a height above the nozzle of about 0.1 m due to less distribution of the fuel. The mass fractions of the evaporated precursor TTIP, the gaseous TiO_2 and the solvent C_3H_8O are plotted in Figure 7-8b, c and d, respectively along the centreline and show that the results are only slightly affected by changes in the spray inlet conditions. For all cases, the liquid precursor and the isopropyl

alcohol are evaporated immediately due to the high pilot flame temperature; the maximum mass fractions of TTIP and C_3H_8O are located at an axial position of about 5 mm. The gaseous fuel gets ignited by the pilot methane flame and the precursor decomposes to TiO_2 leading to an increase of TiO_2 in the gas phase and a decrease of TTIP. Larger droplets (d_{mean} = 120 µm) have a slightly lower evaporation rate. The variation of the spray angle (15°) shows no effect on the mass fractions. Neglecting the dispersion results in marginal higher mass fractions along the centreline, due to less spreading of the droplets. A lower droplet velocity of 10 m/s leads to a minimally earlier and faster evaporation and formation of TiO_2.

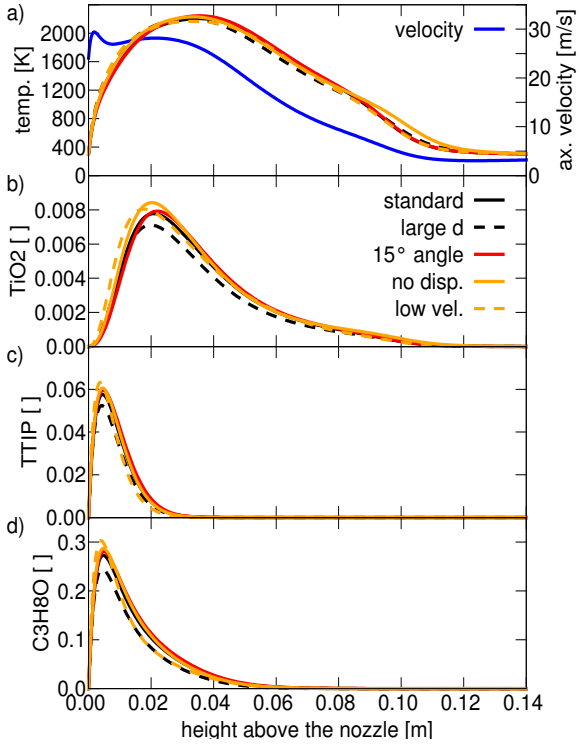

Figure 7-8: Simulation results along the centreline, showing a) axial gas phase velocity and temperature, and gaseous mass fractions for different spray droplet properties (standard case, large droplets, 15° spray angle, no dispersion model and droplet velocity of 10 m/s) of b) TTIP, c) TiO_2 and d) C_3H_8O.

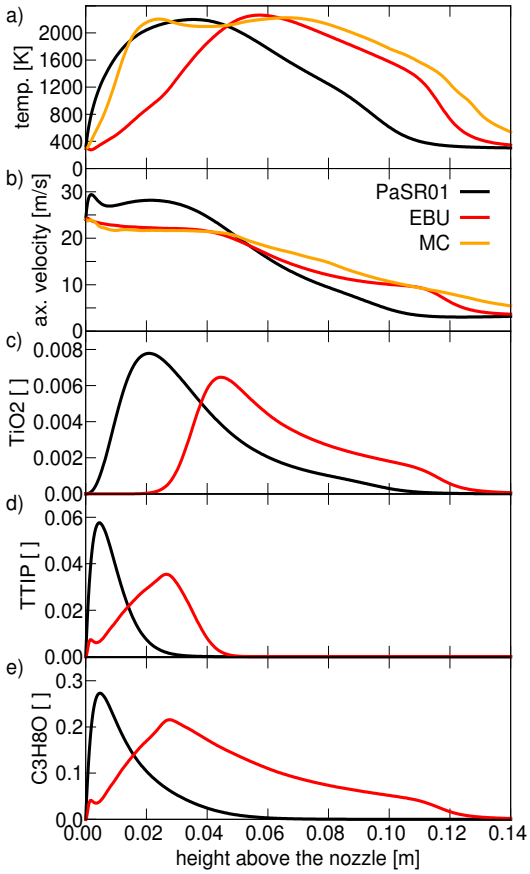

Figure 7-9: Simulation results along the centreline, showing a) temperature, b) axial gas phase velocity, and gaseous mass fractions of c) TTIP, d) TiO_2 and e) C_3H_8O for the PaSR und the EBU model.

PaSR02

This simulation was performed for validation of the further EBU simulations, to show that the substitution of the pilot fuel CH_4 by C_3H_8O does not affect the actual spray flame and hence the nanoparticle size distribution.

The contour plots of the temperature distribution on the longitudinal cross section are illustrated in Figure 7-10 for a methane-oxygen (a) and an isopropyl alcohol-oxygen (b) pilot flame. Although the maximum temperature for the methane pilot flame is slightly higher (~ 100 K), the actual spray flame has the same shape and temperature for both pilot flames.

EBU

The contour plot of the temperature distribution simulated with the EBU model is illustrated in Figure 7-10c. This model predicts a longer and slightly wider flame shape and the spray combustion is located further downstream. The temperature at the spray inlet is lower than in the PaSR simulations, as can be seen in Figure 7-10, due to a lower pilot flame temperature and a narrower pilot flame shape. This is also illustrated by the temperature distribution along the centreline shown in Figure 7-9a: The temperature is less at low heights above the nozzle and is found to increase slowly up to a position of 0.058 m. Further downstream, the flow decelerates slowly (Figure 7-9b) and hence shows larger values at high heights above the nozzle than the PaSR results. Gaseous TiO_2 is produced further downstream with the EBU model, where the total amount of TiO_2 along the centreline is less than for the PaSR model as illustrated in Figure 7-9c.

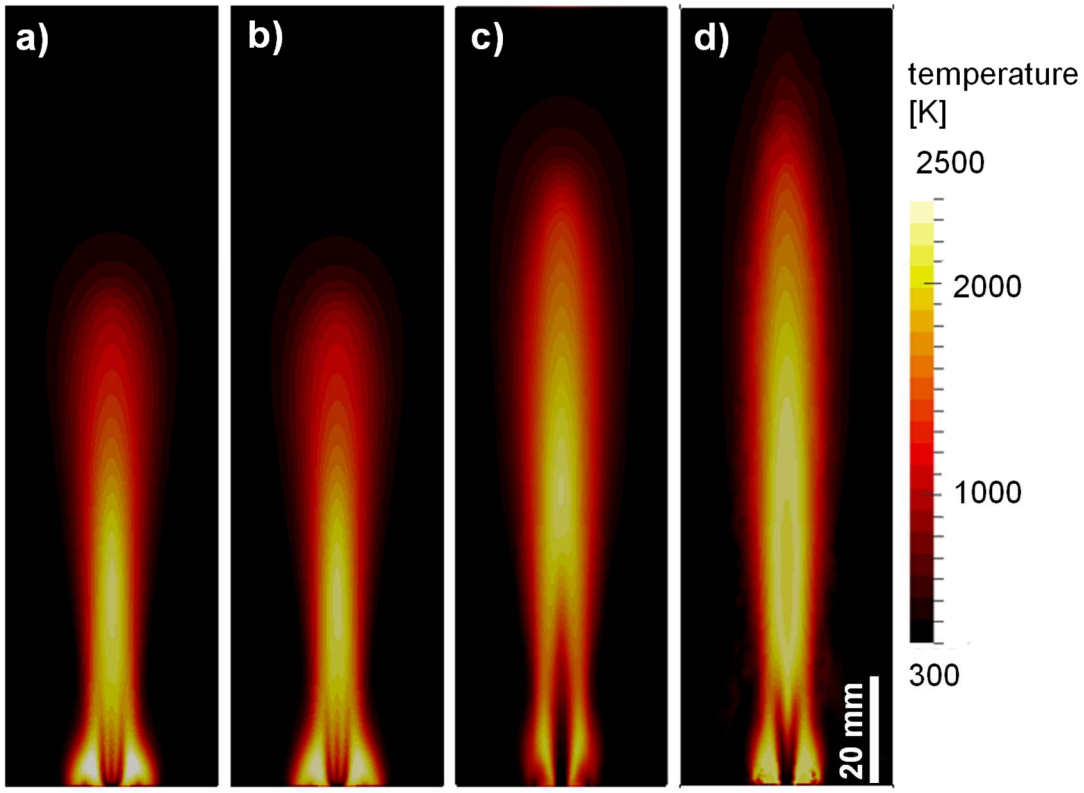

Figure 7-10: Contour plot of the simulated temperature distribution on the longitudinal cross section for a) the PaSR model with a pilot flame with methane and for a pilot flame with an isopropyl alcohol oxygen mixture for the b) PaSR model, c) EBU model and the d) simulation with the Monte Carlo PDF approach showing the time averaged result (area shown: 0.04 x 0.15 m).

The spray droplets are evaporated further downstream (Figure 7-9d, e) and hence, the spray combustion is shifted to higher heights above the nozzle. The injected gas stream widens and the velocity along the centreline drops. At lower heights above the nozzle (up to 0.05 m) the velocity decreases slowly due to the increasing temperature, whilst further downstream the decreasing temperature leads to a faster velocity drop. As the droplets are evaporated completely further downstream for the EBU model, they are spread more widely, which results in the slightly wider flame shape. For the PaSR model, the isopropyl alcohol (Figure 7-9e) and the TTIP (Figure 7-9d) are evaporated faster and are fully burnt at 50 mm and 30 mm above the nozzle, respectively. For the EBU model, the maxima of the gaseous fuel and precursor are located at 30 mm above the nozzle and the isopropyl alcohol and TTIP are completely burnt at 130 mm and 50 mm above the nozzle, respectively, as seen in Figure 7-9d and e. The small peak near the nozzle for the isopropyl alcohol and TTIP distribution in Figure 7-9d and e is caused by the pilot flame.

MC

For the Monte Carlo simulation, the relation between the mixture fraction and the temperature has to be determined. The temperature is plotted as a function of the mixture fraction in Figure 7-11 assuming equilibrium chemistry. This relation was used to calculate the Monte Carlo particle temperature according to the particles' mixture fraction calculated by IEM with the Eulerian field.

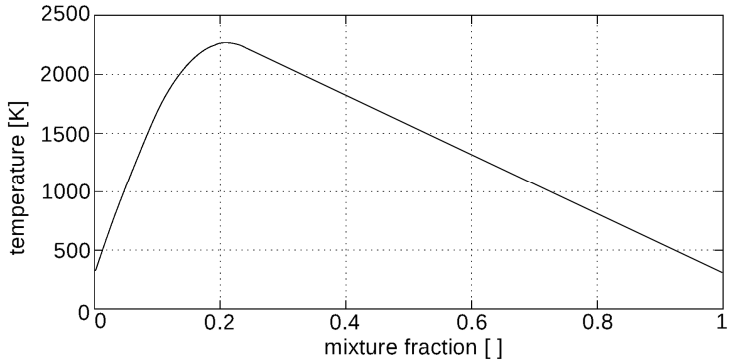

Figure 7-11: Relation between temperature *T* and mixture fraction *Z* for the spray flame, assuming equilibrium chemistry.

A contour plot of the mean temperature field (Equation 121) of the Eulerian field is shown at the longitudinal cross section in Figure 7-10d. The predicted spray flame features the longest flame shape of the four simulations, where at the centreline a slightly cooler spot can be observed. The pilot flame shape is similar to the pilot flame which results from the PaSR model simulations. The temperature and velocity along the centreline are illustrated in Figure 7-9a and b respectively. The temperature steeply increases up to a maximum of about 2200 K along the centreline. At a height above the nozzle of about 0.025 m the temperature drops slightly, because the hot pilot gases might not reach that region. Additionally, this

decrease might be attributed to the evaporation of fuel droplets, which initially provide a local mixture fraction of one. An instantaneous plot of the Monte Carlo particles' mixture fraction is shown in Figure 7-12, where the Monte Carlo particle sizes are scaled according to their mixture fraction. It can be observed that in the slightly cooler region (0.025 m - 0.06 m) many Lagrangian particles feature high mixture fractions and hence represent just evaporated cool fuel.

The predicted velocity of the Eulerian field is similar to the velocity predicted by the EBU approach with a more linear decrease from a position of 50 mm above the nozzle.

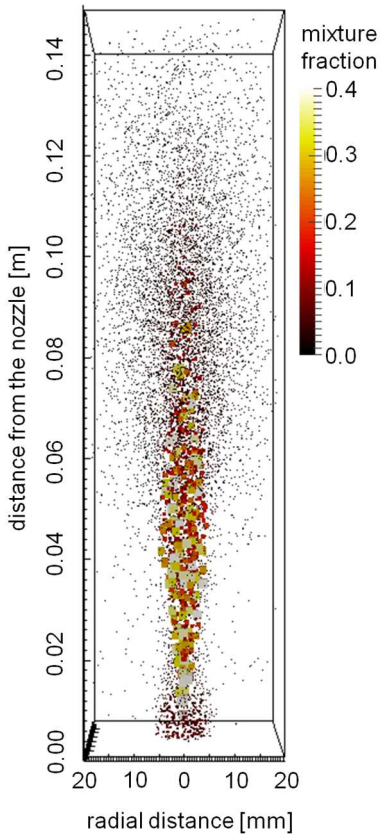

Figure 7-12: Mixture fraction of the Monte Carlo particles, particle size is scaled according to the mixture fraction.

Rough measurements [229] have shown that not all spray droplets evaporate immediately right after the nozzle. The results predicted by the EBU model are therefore more realistic than provided by the PaSR model. In first NO-LIF measurements [229], the length of the spray flame was also observed to be longer than calculated by the PaSR model and better captured by the EBU and the Monte Carlo model. The pilot flame shape provided by the PaSR and the Monte Carlo model matches better the experimental data. The Monte Carlo model provides the best results in comparison with first experimental observations [229] and is therefore the most promising tool. However, the predicted temperature correlates well with experimental observations for all three models.

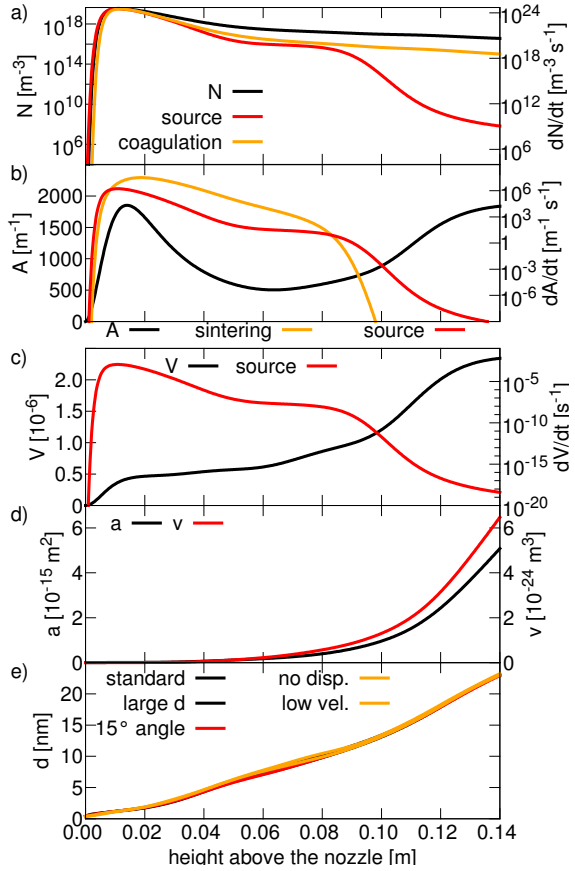

Figure 7-13: Simulation (PaSR01) results along the centreline, showing a) particle number concentration *N*, source and coagulation term, b) surface area concentration *A*, source and sintering term, c) volume concentration *V* and source d) surface area *a* and volume *v* of an aggregate and e) primary particle diameter *d* for different spray droplet properties (standard case, large droplets, 15° spray angle, no dispersion model and droplet velocity of 10 m/s).

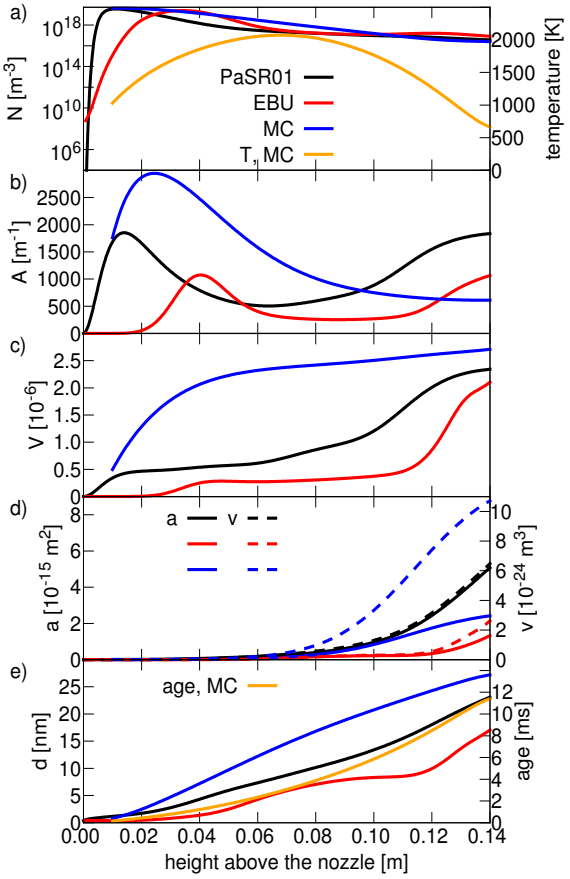

Figure 7-14: Simulation results along the centreline, showing a) particle number concentration *N*, b) surface area concentration *A*, c) volume concentration *V*, d) surface area *a* and volume *v* of an aggregate and e) primary particle diameter *d* for the Euler-Euler simulation with the PaSR and the EBU model and for the MC simulation. For the latter additionally the temperature and the nanoparticle residence time (age) within the reactor is plotted in a) and d), respectively.

7.3.3. Nanoparticle dynamics

The nanoparticle characteristics are presented in this subchapter for the three different simulation approaches PaSR01, EBU and MC.

PaSR01

The nanoparticle dynamics were predicted in a three-dimensional calculation by solving the simplified population balance equations coupled to the spray combustion. The nanoparticle distribution and growth are shown in Figure 7-13a-e along the centreline. The nanoparticle number concentration is shown in Figure 7-13a and additionally its source and coagulation term to illustrate the processes involved. The nanoparticles are formed by nucleation of TiO_2 molecules (Figure 7-13a: source) and coagulate, so that their number decreases (Figure 7-13a:

coagulation). The temperature determines the coagulation process: for high temperatures, a steep decrease of the nanoparticle number concentration can be observed while further downstream, at lower temperatures, the particle number concentration reaches a constant value.

The surface area concentration of the nanoparticles and the source and sintering term are shown in Figure 7-13b. At high temperature, the nanoparticles sinter so that the surface area concentration decreases. Further downstream, at lower temperature, the surface area increases due to less sintering and the dominating formation of new particles.

The nanoparticle volume concentration and its source term are shown in Figure 7-13c. The volume concentration increases along the centreline with a very steep increase at low heights above the nozzle.

The aggregate surface area and the aggregate volume (_ 7-13d) grow with increasing height above the burner due to coagulation.

The primary nanoparticle diameter is presented in Figure 7-13e for different droplet properties. It can be seen that the investigated droplet size, the spray angle, the mean droplet velocity and the dispersion of the droplets have no effect on the particle sizes and morphologies. The TiO_2 monomer diameter is the smallest diameter and the nanoparticles increase up to a maximum diameter of about 23 nm.

EBU

The nanoparticle properties for the simulation with the EBU model are shown in Figure 7-14 in comparison to the PaSR simulations. The particle number concentration plotted in Figure 7-14a increases more slowly than for the PaSR model, which is due to the slower decomposition of the precursor as discussed for Figure 7-9c. The number concentration reaches its maximum value further downstream at about 0.025 m above the nozzle, which is attributed to the further downstream production of TiO_2 molecules (Figure 7-9c). The maximum particle number concentration along the centreline is about 30 % less for the PaSR simulation, which is due to the lower production rate of TiO_2 molecules (Figure 7-9c). At higher heights above the nozzle ($\geq$ 0.1 m) the number concentration predicted by the EBU model is slightly higher than for the PaSR model due to less particle coagulation.

The maximum surface area concentration shown in Figure 7-14b is also lower than using the PaSR model, which is also attributed to the later and lower TiO_2 production rate along the centreline. The first peak of the surface area concentration is shifted to higher height above the nozzle for the EBU model, where for both models the first peak is reached at a temperature of about 1800 K (Figure 7-9a). The second increase of the surface area concentration starts at a height above the nozzle, where the temperature reaches a value of about 1400 K for both simulations; for the PaSR model at about 0.11 m and for the EBU model at 0.07 m above the nozzle.

The volume concentration along the centreline (Figure 7-14c) also features lower values than found for the PaSR model. Both distributions show a steep increase at low heights above the nozzle, which is shifted further downstream for the EBU model. The steeper growth starting at a height of about 0.115 m is attributed to the local higher production rate than calculated for the PaSR model.

The growth of the aggregate surface area and volume illustrated in Figure 7-14d starts at higher heights above the nozzle than for the PaSR model. Hence, particle aggregates with a smaller surface area and volume are predicted, which is also due to the further downstream and less production of TiO_2 molecules (Figure 7-9c). The same behaviour can be observed for the primary particle diameter; the EBU model predicts smaller diameters along the centreline, which is plotted in Figure 7-14e.

MC

For the analysis of the nanoparticle properties, Monte Carlo particles were gathered for a physical time of about 0.1 s at about 200 time steps, which lead to 63 million sampled Lagrangian particles. The particle sample consists of Monte Carlo particles, which evolve from the evaporated precursor and for which the simplified population balance equations were solved. These Monte Carlo particles could be identified by the type ID that each particle was assigned. The sampling starts at a height of 0.001 m above the nozzle, as from this position a sufficient amount of emerged Monte Carlo particles is available for the derivation of suitable particle statistics.

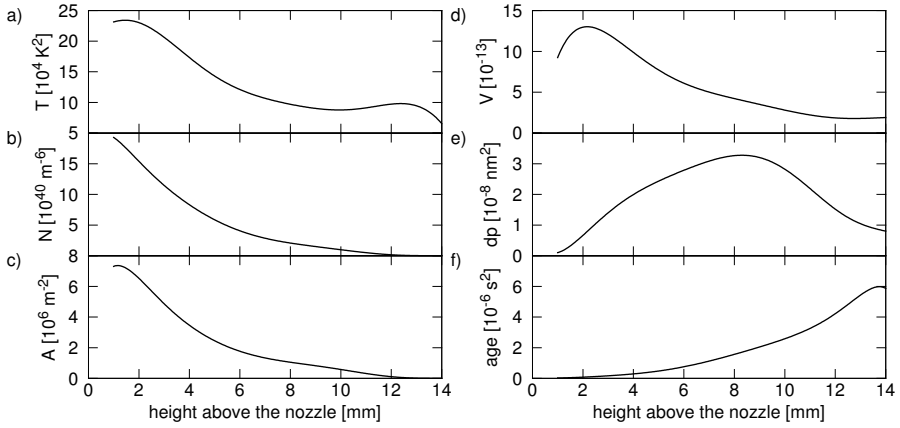

Figure 7-15: Monte Carlo simulation results showing the variance of the nanoparticle properties near the centreline: a) temperature, b) particle number concentration, c) surface area concentration, d) volume concentration, e) primary particle diameter, and f) particle residence time.

The Monte Carlo particles were evaluated at different heights above the nozzle, where each sampling volume was a cylinder with a diameter of 1 mm (around the centreline) and a height of 1 mm, which results in a mean number of 15,000 sampled particles for each height. The

means of the nanoparticle properties (temperature, particle number, surface area and volume concentration, primary particle diameter and residence time) along the centreline are plotted in Figure 7-14. The mean particle temperature shown in Figure 7-14a corresponds to the mean temperature distribution of the Eulerian field (Figure 7-9), apart from the region of a height between 0.01 and 0.06 m above the nozzle, which features an overall lower temperature. However, the temperature close to the nozzle (< 0.01 m above the nozzle) shows a slightly higher temperature. The illustrated nanoparticle temperature in Figure 7-14 represents the temperature of the evaporated precursor particles, which emerge in the spray flame zone. Therefore, for the calculation of the mean temperature, the heat release of the pilot flame particles and the cold co-flow particles, such as the dispersion gas particles, are not considered, which are responsible for the hot region at a height between 0.01 and 0.06 m and for the cold region < 0.01 m above the nozzle, respectively.

The nanoparticle number concentration (Figure 7-14a) reaches its maximum at a height of about 0.005 m above the nozzle. The number concentration decreases exponentially along the centreline due to coagulation and is in the same range as predicted by the previous simulations. Due to the higher temperature of the nanoparticles close to the nozzle, the nanoparticles observe a larger nucleation rate and hence, the number concentration increases much faster than observed for the other modelling approaches.

The surface area concentration illustrated in Figure 7-14b increases due to the formation of new nanoparticles up to its maximum at a height above the nozzle of 0.025 m. Due to higher nucleation rates, this maximum is larger than predicted by the other models. Further downstream, the surface area concentration decreases due to sintering. The Monte Carlo approach does not feature a second increase of the surface area concentration as it was found for the other simulation approaches. This is attributed to the longer spray flame and hence longer hot zone along the centreline, where sintering is the dominating processes. The second increase would therefore be shifted to higher heights above the nozzle, outside the simulation domain.

The volume concentration, which is plotted in Figure 7-14c, shows a steep increase at low heights above the nozzle due to high nucleation rates. From a height of about 0.05 m above the nozzle, the gradient is lower as fewer particles are produced further downstream. The maximum volume concentration is slightly higher than for the other approaches due to the high nucleation rate at low heights above the nozzle.

The aggregate surface area and volume are plotted in Figure 7-14d. Due to the large nucleation rate as already described above, the aggregate volume is larger than predicted by the other modelling approaches. Due to the longer spray flame and the sintering process being the dominating process from a height of 0.025 m above the nozzle, the surface area of the aggregates is only slightly higher than predicted by the EBU approach and smaller than calculated with the PaSR model.

The primary nanoparticle diameter (Figure 7-14e) grows along the centreline and reaches a maximum value of about 27 nm at the outlet, which is slightly higher as predicted by the other simulation due to larger nucleation and coagulation rates. In Figure 7-14e, the age of the Monte Carlo particles and hence of the nanoparticles, which corresponds to their residence time, is additionally plotted. As the velocity decreases along the centreline (Figure 7-9) the gradient of the residence time increases along the centreline.

The variance of the particle properties discussed above is shown in Figure 7-15 along the centreline. The variance of the temperature (Figure 7-15a), the nanoparticle number concentration (Figure 7-15b), the surface area concentration (Figure 7-15c), and the volume concentration (Figure 7-15d) decreases with increasing height above the nozzle. The primary nanoparticle diameter (Figure 7-15e) features its largest variance at a height of about 0.08 m above the nozzle. The variance of the age of the particles (Figure 7-15f) increases downstream. For a better understanding of the distribution of the different particle properties, the discrete probability density function has been analysed for each variable at different heights above the nozzle: For seven heights above the nozzle, discrete probability density functions were evaluated with an interval of 0.02 m along the centreline for the particle properties illustrated in Figure 7-14 and discussed subsequently. Each sampling volume was a cylinder with a diameter of 1 mm (around the centreline) and a height of 1 mm.

The statistics for the temperature are shown on the LHS in Figure 7-16. At a low height above the nozzle of 0.02 m the particle temperature varies between 300 K and 2200 K; the minimum and maximum temperature within the reactor. This zone is the bottom of the spray flame (Figure 7-10): some Monte Carlo particles belong to the hot fluid, where the particles feature a mixture fraction around 0.2 (Figure 7-11) and some to the cold fluid, where the particles represent pure fuel or oxidiser. With increasing height above the nozzle, the temperature increases up to a position of 0.06 m as more Monte Carlo particles are counted among the hot spray flame zone (the discrete PDFs are clipped at 0.25). Further downstream, the particle temperature decreases and for an axial positions of 0.14 m, where the top of the spray flame region is reached (Figure 7-10)), no particles with maximum temperature are counted anymore.

The statistics for the primary nanoparticle diameter are illustrated in the midst of Figure 7-16 (PDFs clipped at 0.25). For a height of 0.02 m above the nozzle, most of the shown Monte Carlo particles have just emerged and feature a nanoparticle diameter smaller than 5 nm. The nanoparticle size increases along the centreline. For lower heights above the nozzle, two peaks can be observed. New particles are formed that feature a small diameter, which causes the left peak. This left peak decreases with increasing height due to the decreasing amount of emerging particles, which becomes negligible from a position > 0.1 m. From an axial position of 0.04 m older particles with larger sizes due to coagulation coexist leading to the second peaks that increase with increasing height. At the maximum height above the nozzle, nanoparticles with a diameter of about 27 nm have the highest probability, which is slightly

higher as predicted by the other models (Figure 7-14). The applied Monte Carlo model features a bimodal particle size distribution, illustrated in Figure 7-16. This bimodal characteristic is caused by different particle histories due to turbulent effects. Although a Monte Carlo particle can only feature a monodisperse nanoparticle size distribution, a real size distribution (Figure 7-16) can be captured in each computational cell, because it contains a large number of Monte Carlo particles, which all act as a small reactor themselves.

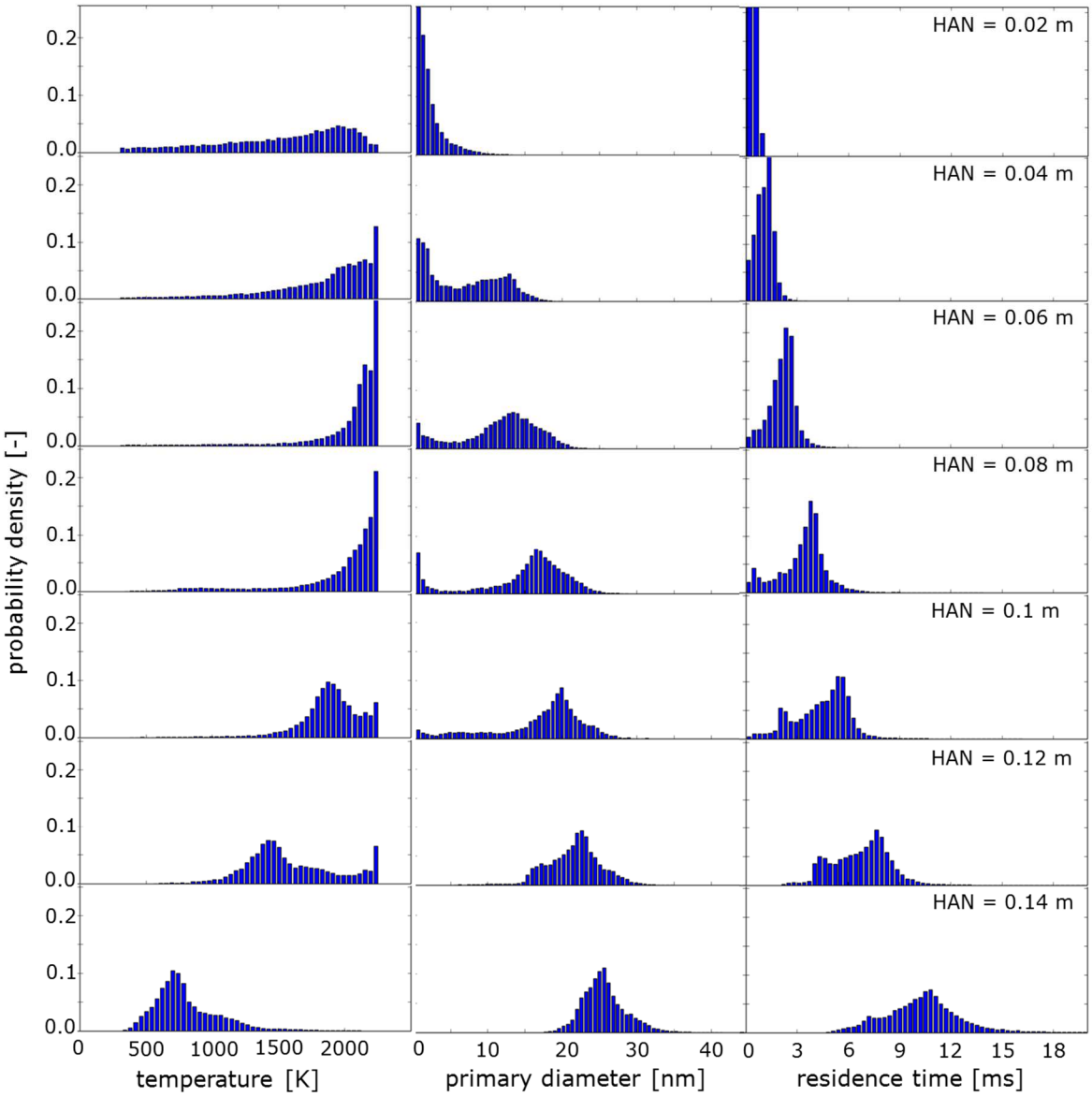

Figure 7-16: Monte Carlo simulation results showing the temperature (left), the primary diameter (middle) and the residence time (right) statistics for the nanoparticles at the centreline for different heights above the nozzle (HAN).

It must be stressed that the Monte Carlo particles do not exchange their precursor mass fraction. Additionally, the nanoparticle properties are not exchanged and therefore different particle sizes cannot interact. The observed PDFs are therefore caused by different Monte Carlo trajectories due to turbulence.

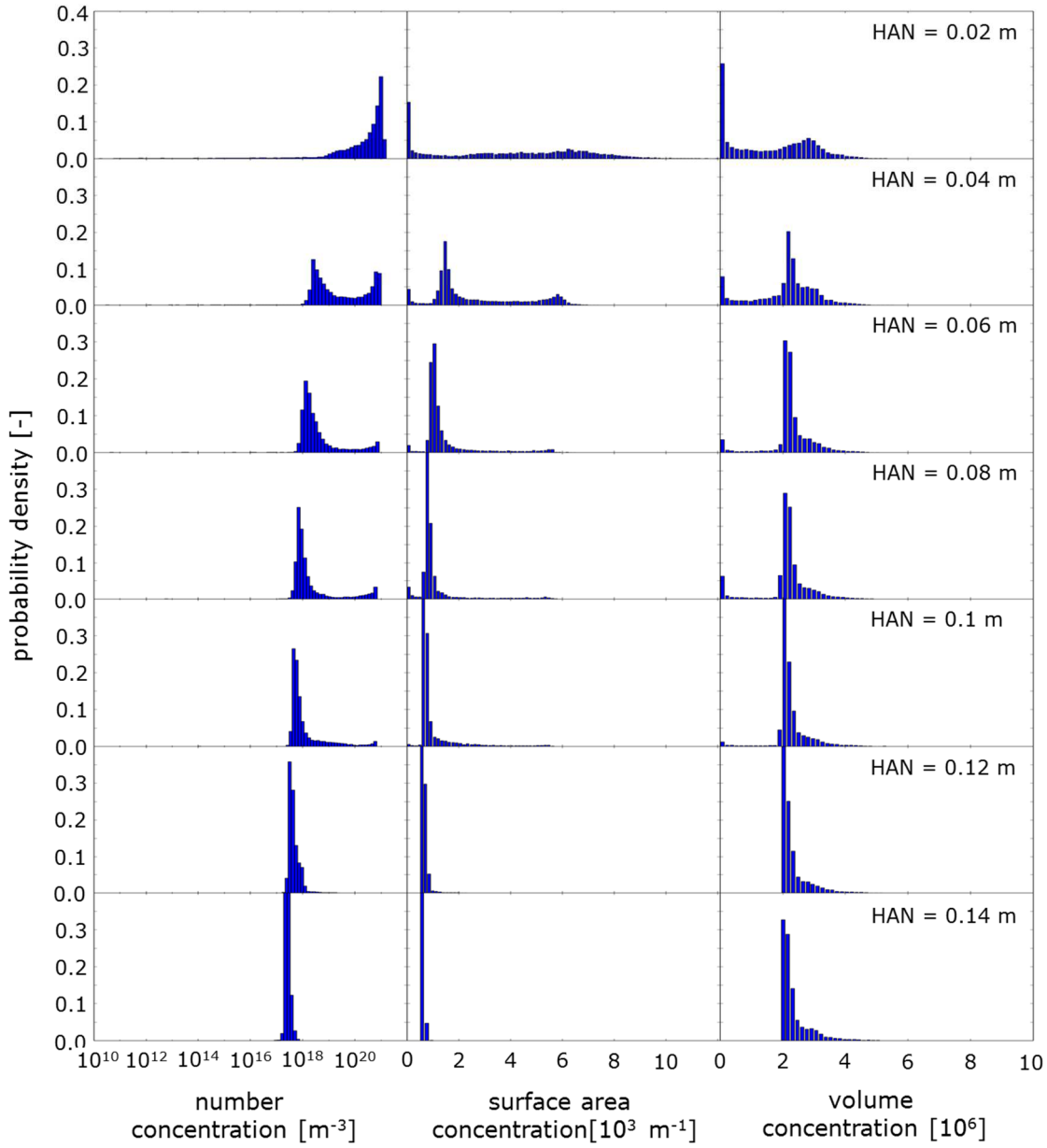

Figure 7-17: Monte Carlo simulation results showing the statistics of the particle number (left), surface area (middle) and volume (right) concentration for the nanoparticles at the centreline for different heights above the nozzle (HAN).

The afore-mentioned bimodal size distribution for the primary nanoparticle diameter was already observed in different experiments and simulations. For TiO_2 synthesis processes, bimodal characteristics were published by Tsantilis et al. [1], Landgrebe et al. [230] and Spicer et al. [231] and were assumed to result from the coexistence of comparable nucleation and coagulation modes. As opposed to this, the bimodal distribution in this PhD work is due to different particle histories only, as discussed above. Usually, complex models, such as bimodal [137] or sectional models [230, 231] are applied and solved, to capture the bimodal distribution due to similar nucleation coagulation modes. However, for a turbulent reactor operation it is impossible to determine for experimental results whether a bimodal distribution is caused by similar nucleation and coagulation modes (as stated in the mentioned publications [1, 230, 231]) or by turbulent effects as presented in this thesis. Hence, the Monte

Carlo approach introduced in this thesis provides a simple technique to predict the bimodal size characteristic observed for TiO_2 nanoparticles synthesized from the gas-phase (although due to a different phenomenon).

In Figure 7-16 on the RHS, the age of the Monte Carlo particles is shown, which corresponds to the residence time of the nanoparticles within the reactor. Up to a height above the nozzle of 0.02 m the nanoparticles have a short residence time (< 1 ms) within the reactor, because they are recently formed. The residence time grows with increasing height above the nozzle. At low heights above the nozzle, new particles emerge in addition to already existing particles, which induces the different peaks for the nanoparticle diameter statistics, which were shown above. Further downstream, the amount of newly formed particles is negligible, where from a position of 0.12 m no new particles arise.

The discrete probability density functions for the nanoparticle number concentration are illustrated on the LHS of Figure 7-17. For a height above the nozzle of 0.02 m, nanoparticle number concentrations of different order of magnitude are observed and the overall largest concentrations can be found. Further downstream, the coagulation process is dominating and the nanoparticle number concentration decreases. Between an axial position of 0.04 m and 0.1 m two peaks are shown for the number concentration. At these heights, new particles still emerge due to the evaporation and decomposition of the precursor. Hence, 'new born' particles and older particles coexist in one cell, which both feature different number concentrations. These different particle histories cause different nanoparticle characteristics, where the older particles have a smaller number concentration due to coagulation. Further downstream, the precursor has completely evaporated and decomposed and hence no new particles emerge. Therefore, with increasing height the range of the number concentration decreases, where at a height of 0.14 m all number concentrations feature the same order of magnitude (PDFs are clipped at 0.4).

The discrete probability density functions for the nanoparticle surface area concentration are presented in the midst column of Figure 7-17 (PDFs are clipped at 0.4). At a height of 0.02 m above the nozzle, a large amount of nanoparticles feature a maximum surface area concentration of 250 m^{-1}, whereas the surface area concentration of the other nanoparticle are spreaded from 250 m^{-1} to 10000 m^{-1}. The overall surface area concentration increases up to a height of about 0.04 m. Further downstream, the overall concentration decreases due to sintering. The different peaks for the axial positions between 0.04 and 0.1 m are attributed to the different histories of the sampled Monte Carlo particles as already discussed above for the afore-mentioned nanoparticle properties. As already observed for the number concentration, the range of the surface area concentration becomes narrower with increasing height.

The discrete probability density functions for the volume concentration at different heights above the nozzle are shown on the RHS of Figure 7-17 (PDFs are clipped at 0.4). At a height of 0.02 m, most particles have a maximum volume concentration of $1.1 \cdot 10^{-7}$. With increasing

height, the volume concentration grows due to nanoparticle nucleation. Also for the volume concentration, two peaks can be found at low heights above the nozzle due to the different particle histories caused by turbulence.

As the primary nanoparticle diameter is determined by the particle history and temperature, the relation of the nanoparticle diameter and the temperature and residence time are illustrated by the scatter plots shown in Figure 7-18. The plots show the residence time along the x-ordinate and the primary nanoparticle diameter along the y-ordinate, respectively. The points are coloured by the particle temperature.

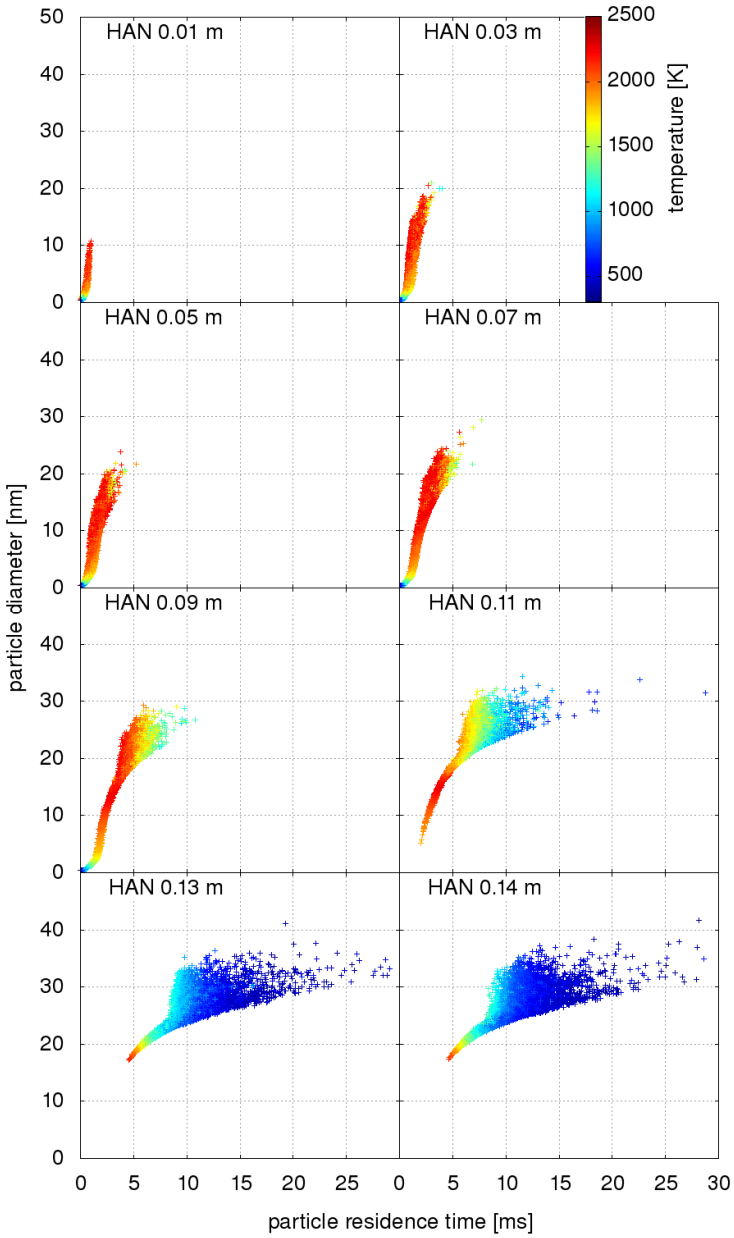

Figure 7-18: Scatter plot of the primary nanoparticle diameter in relation to the residence time of the nanoparticles coloured by the particle temperature. The Monte Carlo particles are sampled at the centreline for different heights above the nozzle (HAN).

For low heights above the nozzle (0.01 m), a particle growth with increasing residence time can be observed in Figure 7-18, where also the temperature increases with the age of the particles. It can be seen that the particles are heated up very fast (~ 2 ms until the maximum temperature is reached) and cool down much slower. Particles with low residence times and temperatures show small diameters with a narrow range. For larger residence times and temperatures, coagulation leads to bigger particles, which differ in size according to the progression of the coagulation process. As the coagulation increases with increasing temperature, a kink in the particle growth rate can be observed for a residence time of about 1 ms - 2 ms at lower heights above the nozzle (≤ 0.09 m), where the particles temperature reaches a value about 1500 K. Further downstream, from a certain residence time, the temperature does not increase with the age of the particles; some old particles also feature low temperatures. Due to turbulent dispersion and fluid recirculation, these particles come from colder zones outside the spray flame. From a position of about 0.07 m, the overall temperature along the centreline (Figure 7-14a) decreases and hence the particles cool down and the overall growth rate decreases. With increasing height, the scatter of the particles for larger residence times grows, as particles with the same residence time feature a broader variety of trajectories. Particles, which are located in hot regions, are more likely to coagulate and hence grow faster. Particles travelling through cold regions experience less coagulation, but due to their longer residence time, they have more time to grow. The size distribution is spanned by two boundaries: The left boundary illustrates particles, which reach the sampling point on a direct patch, hence, which travel along or near the centreline. Their sizes steeply increase with their residence time due to the hot temperature, which they experience. At the bottom right boundary the coolest and smallest nanoparticles can be found, which come from colder regions outside the spray flame. Therefore, the growth of these nanoparticles is much slower due to less coagulation. According to their history, particles experience different coagulation and precursor decomposition rate, which both dictate the final nanoparticle size. Therefore, no straight bounds are observed for the shown particle size distributions.

The nanoparticle number concentrations in relation to the particle temperature and the particle residence time are illustrated in Figure 7-19 for different heights above the nozzle. Up to a height above the nozzle of about 0.08 m the range of the number concentration spans from the minimum to the maximum nanoparticle number concentration for each position. It can be seen that the maximum number concentration is reached at a temperature of 1500 K. Below this temperature, the number concentration is uniform; it is an exponential function of the temperature. For this temperature range, nucleation is the dominant process. The formation rate of nanoparticles (nucleation rate) was assumed to be equal the production rate of TiO_2 molecules, which was calculated by an Arrhenius approach and hence as an exponential function of the temperature. Above a temperature of 1500 K, the number concentration decreases due to coagulation, which becomes the dominant process. For axial positions between 0.02 m and 0.06 m, the number concentration scatters at temperatures above 1500 K.

In this region, particles with different histories can be observed. Nanoparticles with a low residence time (~ 1 ms) have experienced less coagulation than particles with a longer residence time, but can be heated up very fast and hence feature a higher number concentration for the same temperature than older particles. When the particles cool down, the gradient of the number concentration decreases, as coagulation declines, but still dominates the process. Above an axial position of 0.08 m, the number concentration decreases more uniformly with less scattering. At this region, the hot particles all have a residence time of about 2.5 ms and experienced similar coagulation. The number concentration finally tends to a value of about $2 \cdot 10^{17}$ m^{-3}. For all heights above the nozzle, particles with temperatures in the range of the global minimum and maximum (300 K and 2250 K) can be found.

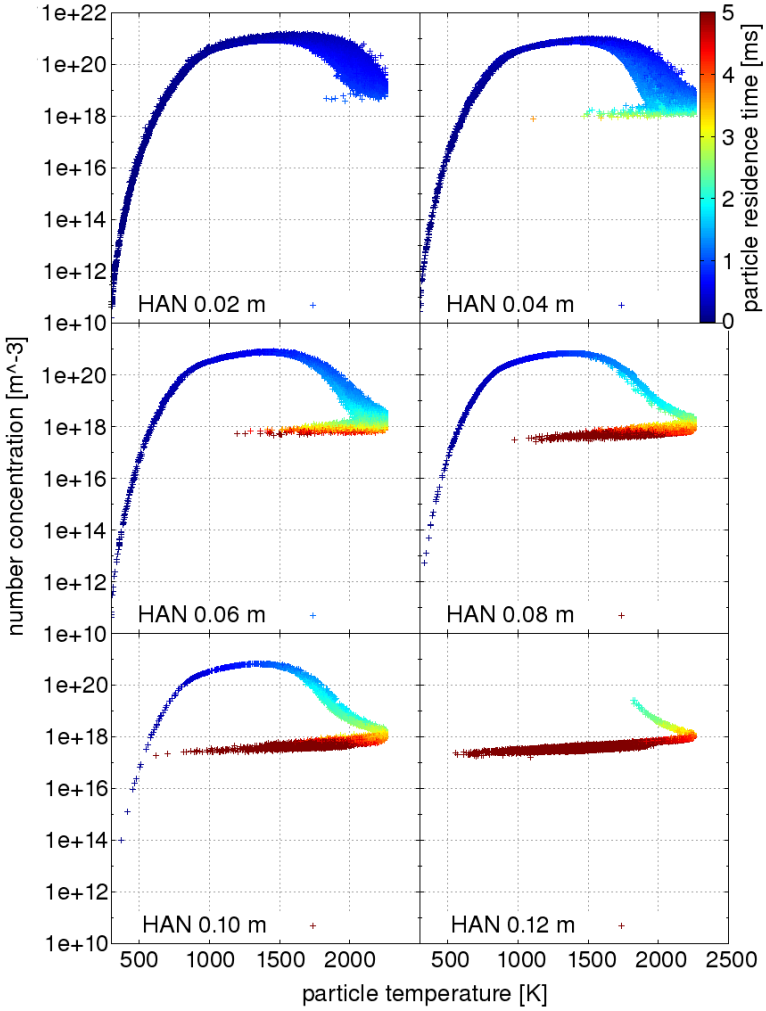

Figure 7-19: Scatter plot of the particle number concentration in relation to the particle temperature coloured by the residence time of the nanoparticles. The Monte Carlo particles are sampled at the centreline for different heights above the nozzle (HAN).

As the surface area concentration depends on temperature and nanoparticle diameter (see Equation 106), the nanoparticle surface area concentration is plotted in relation to the temperature and coloured by the nanoparticle diameter in Figure 7-20 for six different heights above the nozzle. For all heights above the nozzle, it can be seen, that sintering becomes dominant for nanoparticles > 2 nm and a temperature of about 1700 K. For smaller and cooler

nanoparticles, nucleation dominates. At a height of 0.02 m above the nozzle, for nanoparticles up to a diameter of 2 nm the surface area concentration increases up to the largest area surface concentration of about $1.3 \cdot 10^4$ m^{-1}. From a temperature of about 1700 K the surface area concentration scatters, as small nanoparticles (< 2 nm), for which nucleation dominates, coexist with larger nanoparticles, for which sintering is the dominant process. The larger and hotter the particles the more they sinter. For an axial position of 0.04 m, the maximum surface area concentration has decreased by nearly 50 % compared to a position of 0.02 m due to sintering. From this position, no nanoparticles with a diameter smaller than 2 nm and a temperature above 1700 K exist. Therefore, above a temperature of 1700 K sintering is the ruling process for all particles and the scatter above this temperature (caused by the hot small particles) decreases with increasing height. When the particles cool down, the surface area concentration remains constant; all nanoparticles tend to have a final surface area concentration of about 800 m^{-1}.

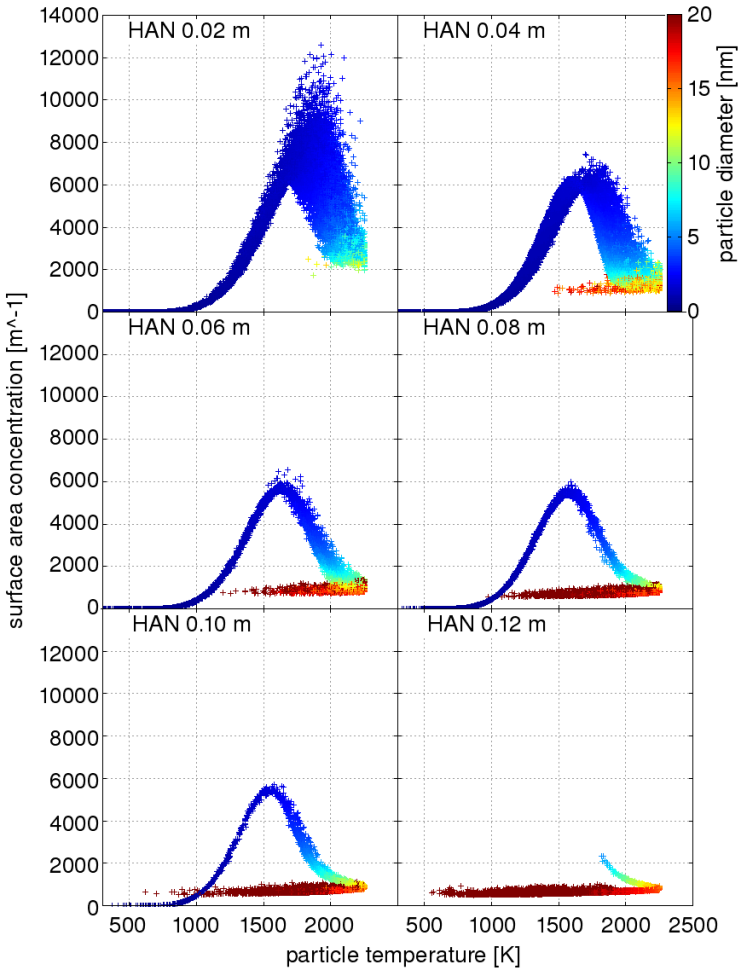

Figure 7-20: Scatter plot of the particle surface area concentration in relation to the particle temperature coloured by the primary nanoparticle diameter. The Monte Carlo particles are sampled at the centreline for different heights above the nozzle (HAN).

7.4. Discussion

The VOF simulation and the experiment showed a good qualitative and even quantitative agreement and provided the spray properties for subsequent spray combustion simulations. The shape of the turbulent flame was captured by visual light scattering and simulation results were found to be in (qualitative) agreement with the experimental evidence. The simulations and experiments have shed light on the break-up process and the spray combustion in the reactor. This was the first detailed investigation of this spray nozzle, which is somewhat surprising given the high popularity of the investigated spray flame reactor.

The different simulation approaches give an insight into the interacting complex processes inside the spray flame reactor, where the Eulerian PBE approach and the hybrid Monte Carlo approach have two different objectives: The Euler-Euler frameworks are particularly suited to conduct parameter studies in such reactors, to analyse the effect on the nanoparticle properties caused by changes in the mass flow, precursor concentration, or precursor composition. The Monte Carlo simulation is more complex, but provides statistics for the nanoparticle properties for each individual computational cell and could show that the Monte Carlo particles feature a variety of trajectories at the same time and location. Whereas in the Euler-Euler RANS simulations the precursor was predicted to decompose rapidly and all nanoparticles emerge at the same time at a low height above the nozzle, the Monte Carlo simulation showed that nanoparticles also arise at high heights above the nozzle and that newly formed and older nanoparticles coexist at the same time and feature different properties. Additionally, the Monte Carlo method featured the age of the Monte Carlo particles and hence the nanoparticles' residence time. Therefore, the dynamic of the different processes (e.g. nanoparticle growth) could be analysed. Although a Monte Carlo particle has a monodisperse nanoparticle distribution, the collection of different Monte Carlo particles provides a real nanoparticle size distribution. The Monte Carlo model predicted a bimodal nanoparticle size distribution, which has also been observed in previous experiments. In the experiments, the bimodal characteristic was assumed to result from comparable nucleation and coagulation modes, but in this thesis it is caused by turbulent phenomena. However, for a reactor, which features a turbulent flow, it is impossible to determine, if a measured bimodal distribution is due to similar nucleation and coagulation modes or caused by turbulence. Hence, the Monte Carlo approach represents a simple technique to model the bimodal size distribution for TiO_2 nanoparticles from the gas-phase only due to turbulence. The mean nanoparticle properties predicted by the Monte Carlo simulations were in the same range as for the Euler-Euler approaches.

A parameter study has shown the nanoparticle formation to be insensitive to small variations of the initial droplet size distribution, the spray angle, the mean droplet velocity and the droplet dispersion. This means that accurate simulations of the system are feasible and that the reactor behaves generally robust to small changes in its operation parameters. This robustness

is a prerequisite for the application of more elaborated ex situ and in situ diagnostics, which would be required to develop more sophisticated particle formation models.

With the results shown in this work, many things have become clearer as afore-mentioned, but still more questions have arised. The research in the field of nanoparticle synthesis, especially in spray flame reactors, is still in its infancy, as many phenomena are not fully understood, yet. Therefore, many further simulations and detailed experiments are needed. The simplified Monte Carlo modelling approach, introduced in this thesis, already provides "good" results, but still has room for further improvements and validation. Firstly, the simplified model has to be extended to a full Monte Carlo model considering a two-way coupling between Monte Carlo particles and Eulerian field. Further modelling would require a more precise resolution of the turbulent flow field by using a LES and a two-way coupling of the Monte Carlo particles and the flow field or a full velocity-composition PDF (not a hybrid method). Additionally, the turbulence-chemistry interaction has to be solved, for example by introducing a second joint PDF. Further improvements would also require detailed chemistry, flamelet tables and a more complex mixing model. Also more accurate population balance models to capture polydisperse distributions within each Monte Carlo particle might be advantageous and considering the collision of nanoparticles within different Monte Carlo particles. Additionally, appropriate experiments are needed for validation. These experiments have to provide instantaneous measurements and statistics of the species, the velocities and the temperature of the flow, the spray droplets and the nanoparticles and nanoparticle sizes, numbers, volumes and surface areas.

However, the introduced modelling approach has broken the first ground for further studies.

8. Conclusions and outlook

This thesis presents numerical simulations for the investigation of nanoparticle synthesis processes with focus on the modelling of a spray-flame assisted synthesis used for the production of titania nanoparticles from titanium tetraisopropoxide (TTIP).

Previous simulations for different reactor types, which are applied at the Institute of Combustion and Gasdynamics, have provided modelling experience and have helped to understand the flow field and the physical processes within synthesis reactors. Additionally, the studies have shown the importance of conducting simulations for suitable designing of synthesis reactors. Simulations in a hot-wall reactor were used to determine appropriate conditions for a stable reactor operation with high production rates. Weak spots in the reactor design in terms of the fluid flow could be detected. A subsequent optimization of the reactor geometry helped to avoid recirculation zones and particle depositions at reactor components. Furthermore, limits for commonly used one-dimensional models for these reactor types, denoted as plug flow models, were exposed and discussed. The simulations have shown that even in such simple symmetric geometries the flow might be quite complex and needs investigation. For another reactor type, a low-pressure microwave plasma reactor, a CFD study was used for designing a new coflow nozzle. The fluid flow within the reactor for various nozzle concepts was predicted by simulation the best nozzle was evaluated regarding the precursor jet direction, the stabilization of the plasma and the shielding of the reactor walls from the produced particles. The constructed nozzle was implemented into the reactor and has now been successfully used for more than three years providing a stable reactor operation and high production rates. Simulations of a horizontal low-pressure flat flame reactor have pointed out limitations for nanoparticle synthesis experiments due to buoyancy effects. The flow fields of iron oxide nanoparticle synthesis in an $Ar/O_2/H_2$ flame and of carbon nanoparticle synthesis in a sooting acetylene flame were examined for this reactor type. Additionally, measurements conducted by the Schulz' group determined the mean iron oxide nanoparticle size from particle mass spectrometry (PMS) as a function of the distance from the burner. A sudden rise of the particle growth rate was measured by the experimentalists at a critical distance from the burner, which could be explained by the calculated flow field. Due to buoyancy effects, the flow can become asymmetric and unwanted recirculation zones are formed. Therefore, the buoyancy effects limit the operating range of the experimental setup, which requires a one-dimensional symmetric flame to permit a meaningful interpretation of the measured data. Hence, different methods and modifications were analysed by CFD in order to determine a maximum burner distance for the sampling point and to overcome the asymmetry. The maximum burner distance was derived from simulations and estimated analytically as a function of the inlet velocity and the burner diameter, leading to a maximum residence time. To overcome asymmetry, one-dimensional

calculations of the particle dynamics along different streamlines were performed. The calculation results confirmed that buoyancy has an essential effect and correspond well with the experimental findings. Experience gained by these particle dynamics calculations was further used for modelling of the more complex spray-flame assisted synthesis. The previous studies have shown the potential of three-dimensional CFD simulations for closing the gap between reactor experiments and one-dimensional simulations of reaction kinetics. Reactor simulations can be used for designing new reactor and will be the basis for a reactor scale-up from pilot to industrial scale.

The main part of this thesis concerns the three-dimensional simulation of a spray-flame assisted synthesis process with different modelling approaches using OpenFOAM. The nanoparticle synthesis within this reactor involved various simultaneously and potentially interacting physical processes, which made modelling challenging. The processes can roughly be divided into three main parts: a) the liquid jet break-up, b) the turbulent combustion, and c) the nanoparticle formation and growth. Since the jet break-up process and hence the spray properties within the reactor were completely unknown, Volume of Fluid (VOF) simulations were performed to determine the break-up mode. These simulations together with shadowgraphy imaging performed by Jan Menser provided the spray boundary conditions (droplet diameter distribution, velocity and spray angle) required for further simulation. The findings from the VOF simulations correlated well with the shadowgraphy and provided insight into the primary break-up process.

A first, ground-breaking complete three-dimensional reactor simulation was an Euler-Euler simulation, whereby the combustion was modelled with the Partially Stirred Reactor (PaSR) approach and the simplified population balance equations (PBE) were solved in the Eulerian frame coupled to the flow. In order to calculate the precursor evaporation and the particle nucleation rate necessary to solve the simplified PBE, a new solver was written and new libraries were implemented in OpenFOAM. The predicted shape of the spray flame showed a good qualitative agreement with corresponding shadowgraphs. Additionally, a parameter study was performed to analyse the sensitivity of the spray properties for the nanoparticle characteristics. It was found that a slight variation of the droplet properties has a negligible effect on the particle formation. This fact indicates a robust reactor operation and feasible accurate simulations of the processes. Besides the analysis of the main particle properties (number, surface area and volume concentration and diameter), the particular processes responsible for the particle formation and evolution were investigated and visualized. These were the nucleation, coagulation and sintering processes.

For the second approach, the combustion was modelled with the well-known Eddy Break-Up (EBU) model to cross-check the results generated with the more unknown PaSR model. Therefore, new routines were implemented in OpenFOAM to calculate the EBU reaction rate and the corresponding nanoparticle source terms. The precursor decomposition and the PBE were calculated in the Eulerian frame as a post-processing step, because the EBU model can

only handle the reaction of one fuel species reaction. The EBU model predicted a slightly slower precursor evaporation and decomposition at higher heights above the nozzle than the PaSR model. Hence, the spray flame was shifted downstream. Due to the delayed and slower production of the particles, they featured a smaller size than observed for the PaSR model. The Euler-Euler RANS simulation approaches represent a suitable framework for parameter studies. The short computational time make these approaches a practical tool for geometry and operating conditions optimization as well as for the design of new reactor components.

The main task of this work was the implementation of a simplified hybrid Lagrangian Monte Carlo model in OpenFOAM, which accounts for the interaction of turbulence and particle dynamics. For this approach, Lagrangian particles were used to determine statistics for the nanoparticle properties. The Monte Carlo particles act as small reactors themselves, for which the precursor decomposition was solved and the PBE were modelled. The particles interacted by temperature exchange with the mean. Each Monte Carlo particle carries a mixture fraction, which changes by exchange with a mean mixture fraction field from a previous RANS simulation. For this modelling approach, a new particle class was implemented into OpenFOAM to solve the Monte Carlo particle evolution and the nanoparticle dynamics. New libraries for the modelling of the PBE for the Monte Carlo particle were created and a new solver was set up to solve for example the Monte Carlo particle formation, injection and the coupling with the Eulerian field.

The mean temperature field provided by the Monte Carlo method has featured a longer spray flame than the Euler-Euler approaches. The mean nanoparticle properties were in the range of previous simulation results, but the nanoparticle statistics showed a broad sample space. With the Monte Carlo approach the age of each Monte Carlo particle could be addressed. This age corresponds to the residence time of the nanoparticles, which influences the nanoparticle characteristics. In consequence, the impact of residence time and temperature on the nanoparticle size distribution could be analysed in detail. The residence time provided the dynamics of the different processes, for example how fast a nanoparticle grows. Although a Monte Carlo particle has a monodisperse nanoparticle distribution, the collection of different Monte Carlo particles provides a real nanoparticle size distribution. With the Monte Carlo method, particle statistics could be derived for each individual computational cell. The Monte Carlo simulation could illustrate that nanoparticles with different histories and properties can be found at the same location and time; meaning, that nanoparticles with different trajectories coexist at the same time and location. The Monte Carlo model predicted a bimodal size distribution due to turbulent effects. For TiO_2 nanoparticle synthesis, bimodal distributions were already observed in previous studies [1, 230, 231] and assumed to result from similar coagulation and nucleation modes. However, for a turbulent reactor process, it is impossible to determine whether a measured bimodal nanoparticle size distribution results from similar nucleation and coagulation modes or from turbulent phenomena.

For the improvement of the presented simulation approaches, experimental data is needed, for example to set the model constants more properly. Since simplified models were used to describe the physics for all simulation approaches, further experimental analysis is also required for validation. Suitable experiments consist of detailed instantaneous measurements and statistics of at least temperature, species concentrations, velocities, and particle population data. According to the findings of these experiments, the presented frameworks could be enhanced and the need of the use of more complex models and techniques, which are addressed subsequently, can be evaluated.

As the Monte Carlo particles interact with the constant mean mixture fraction field of a previous RANS simulation, the accuracy of the Monte Carlo results depend on the accuracy of the previous simulation. A further advancement of the presented model would therefore require a two-way coupled interaction of the Monte Carlo particles and the Finite Volume field to fully solve the particle-turbulence interaction. An additional improvement of the introduced model would be a more precise resolution of the flow field by a LES or a full velocity-composition PDF (not a hybrid method). The applied method only solves the interaction of turbulence and nanoparticle dynamics, but not the turbulence-chemistry interaction for the spray flame, which would require the use of a second joint PDF. Further advancements would also be the usage of detailed chemistry, flamelet tables and a more complex mixing model. Additionally, a more precise PBE model has to be considered and with it the collision of nanoparticles of different Monte Carlo particles.

For a reactor scale-up from pilot to industrial scale, a deep understanding of the physical processes within the reactor is obligatory. This thesis has shown that three-dimensional CFD simulations can provide this necessary insight into the reactor processes and provided frameworks with different complexities for future investigations.

9. References

[1] S. Tsantilis, S. E. Pratsinis, AIChE J. 46 (2000) 407-415.

[2] F. Iskander, Adv. Pow. Techn. 20 (2009) 283-292.

[3] F. E. Kruis, H. Fissan, A. Peled, J. Aerosol Sci. 29 (1998) 511-535.

[4] V. Polshettiwar and T. Asefa (Eds.), *Nanocatalysis: Synthesis and Applications*, John Wiley & Sons, New York, 2013.

[5] A. Roucoux, J. Schulz, H. Patin, Chemical Reviews 10 (2002) 3757–3778.

[6] A. Bitar, N. M. Ahmad, H. Fessi, A. Elaissari, Drug Discovery Today 17 (2012) 1147-1154.

[7] Q. A. Pankhurst, J. Connolly, S. K. Jones, J. Dobson, J. Phys. D: Appl. Phys.36 (2003) 167–181.

[8] C. R. Lowe, Current Opinion in Structural Biology 10 (2000) 428-434.

[9] *The future of nano-biology: regenerating tissue and artificial proteins*, available at http://www.zdnet.com (December 2014).

[10] H. K. Kammler, L. Mädler, S. E. Pratsinis, Chem. Eng. Technol. 24 (2001) 583-596.

[11] H. Wiggers, R. Starke, P. Roth, Chem. Eng. Technol. 24 (2001) 261-264.

[12] H. R. Orthner, P. Roth, Mat. Chem. Phys. 78 (2002) 453-458.

[13] J. Knipping, H. Wiggers, B. F. Kock, T. Huelser, B. Rellinghaus, P. Roth, Nanotechnol. 15 (2004) 1665-1670.

[14] A. Kowalik, P. Ifeacho, H. Wiggers, C. Schulz, P. Roth, *TiO2 nanoparticle formation in a premixed flame and a plasma reactor: Comparison between experiment and numerical simulation*, European Combustion Meeting, Chania, Greece, 2007.

[15] J. Knipping, H. Wiggers, B. Rellinghaus, P. Roth, D. Konjhodzic, C. Meier, J. Nanosci. Nanotechnol. 4 (2004) 1039-1044.

[16] P. Ifeacho, T. Huelser, H. Wiggers, C. Schulz, P. Roth, Proc. Combust. Inst. 31 (2007) 1805-1812.

[17] P. Roth, A. Hospital, J. Aerosl Sci. 1 (1994) 61-73.

[18] J. H. Braun, J. Coat. Technol. 69 (1997) 59–72.

[19] P. Roth, Proc. Combust. Inst. 31 (2007) 1773-1788.

[20] L. Maedler, H. K. Kammler, R. Mueller, S. E. Pratsinis, J. Aerosol Sci. 33 (2002) 369–389.

[21] S. E. Pratsinis, Prog. Energy Comb. Sci. 24 (1998) 197–219.

[22] C. Weise, A. Faccinetto, S. Kluge, T. Kasper, H. Wiggers, C. Schulz, I. Wlokas, A. Kempf, Comb. Th. Model. 17 (2013) 504-521.

[23] K. Wegner, S. E. Pratsinis, *Innovative Processing of Films and Nanocrystalline Powders*, (K. L. Choy, editor) Imperial College Press, London, 2002.

[24] E. L. Cussler, *Diffusion - Mass Transfer in Fluid Systems*, Cambridge University Press, Cambridge/New York, 1997.

[25] J. Hirschfelder, C.F. Curtiss, R.B. Bird, *Molecular Theory of Gases and Liquids*, John Wiley & Sons, New York, 1954.

[26] W. P. Jones, R. P. Lindstedt, Combust. Flame 73 (1988) 233-249.

[27] R. W. Bilger, Proc. Combust. Inst. 22 (1989) 475–488.

[28] O. Reynolds, Phil. Trans. R. Soc. London, 174 (1883) 935-982.

[29] S. B. Pope, *Turbulent flows*, Cambridge University Press Cambridge/New York, 2000.

[30] R. S. Cant, E. Mastorakos, *An Introduction to Turbulent Reacting Flow*s, Imperial College Press, London, 2008.

[31] E. G. Moody, L. R. Collins, Aerosol Sci. Technol.37 (2003) 403-424.

[32] D. Moxey und D. Barkley, Proc. Natl. Acad. Sci (NY) 107, 8091 (2010).

[33] J. Rotta, Ing. Arch. 24, 258 (1956).

[34] H. Schade, E. Kunz, *Strömungslehre*, 2. Aufl., de Gruyter, Berlin, New York, 1989.

[35] O. Reynolds, *On the Dynamical Theory of Incompressible Viscous Fluids and the Determination of the Criterion*, Phil. Trans. R. Soc. London, 186 (1895) 123-164.

[36] B. E. Launder, G. J. Reece, W. Rodi, J. Fluid Mech. 3 (1975) 537-566.

[37] W. P. Jones, B. E. Launder, Int. J. Heat Mass Transfer, 15 (1972) 301-314.

[38] B. E. Launder, B. I. Sharma, Letters Heat Mass Transfer, 1 (1974) 131-138.

[39] B. E. Launder and D. B. Spalding, *Lectures in Mathematical Models of Turbulence*. Academic Press, London, England. 1972.

[40] V. Yakhot, S. A. Orszag, S. Thangam, T. B. Gatski C. G. Speziale, Phys. Fluids A, 4 (1992) 1510-1520.

[41] C. E. Brennen, *Fundamentals of Multiphase Flow*. Cambridge University Press, Cambridge/New York, 2005.

[42] N.Ashgriz, *Handbook of Atomization and Sprays*, Springer-Verlag, Berlin-New York, USA, 2011.

[43] P. Marmottant, E. Villermaux, J. Fluid Mech. 498 (2004) 73-111.

[44] L. Rayleigh, Proc. R. Soc. London, 29 (1987) 71–97.

[45] C. Z. Weber, Math. Mech. 11 (1931) 136–54.

[46] G. I. Taylor, In The Scientific Papers of G.I. Taylor, ed. GK Batchelor, 3 (1962) 244–54.

[47] S. P. Lin, R. D. Reitz, Annu. Rev. Fluid Mech. 30 (1998) 85 -105.

[48] C. W. Hirt, B.D. Nichols, J. Comput. Phys. 39 (1981) 201-225.

[49] W. J. Rider, D.B. Kothe, J. Comput. Phys. 141 (1988) 112 – 152.

[50] G. K. Karch, F. Sadlo, P. Rauschenberger, C. Meister, K. Eisenschmidt, B. Weigand, T. Ertl, *Visualization of Piecewise Linear Interface Calculation*, Proc. IEEE Pacific Visualization Symposium, Syndney, Australia, 2013.

[51] H. Rusche, *Computational fluid dynamics of dispersed two-phase flows at high phase fractions*, PhD Thesis, Imperial College, London, UK, 2002.

[52] J.U. Brackbill, D.B. Kothe, C. Zemaach , J. Comput. Phys. 100 (1992) 335–354.

[53] G. H. Yeoh, J. Tu, *Computational Techniques for Multiphase Flows*, Elsevier Ltd., Oxford, UK, 2009.

[54] H.J. Ferziger, M Peric, *Computational methods for fluid dynamics*,Springer Verlag, Berlin-New York, 1995.

[55] M. Seifollahi, E. Shirani, N. Ashgriz, Europ. J. Mech.B/Fluids 27 (2008) 1–23.

[56] M. Sussman, E.G. Puckett, J. Comput. Phys. 162 (2000) 301–337.

[57] M. Sussman, P. Smereka, S. Osher, J. Comput. Phys. 114 (1994) 146-159.

[58] T. Menard, S. Tanguy, A. Berlemont, Int. J. Multiphase Flow 33 (2007) 510–524.

[59] R. Fedkiw, T. Aslam, B. Merriman, S. Osher, J. Comput. Phys. 152, (1999) 457–492.

[60] X. Li, M. Arienti, M. Soteriou, M. Sussman, *Towards an Efficient, High-Fidelity Methodology for Liquid Jet Atomization, Computations*, AIAA-2010-0210, 48th AIAA Aerospace Sciences Meeting, Orlando, Florida, USA, 2010.

[61] A. B. Liu, D. Mather, and R. D. Reitz, SAE Technical Paper 930072 (1993).

[62] A. D. Gosman, E. Ioannides, AIAA Papers (1981) 81-0323.

[63] M. Pilch, C.A. Erdman, Int. J. Multiphase Flow, 13 (1987) 741–757.

[64] W.E. Ranz , W.R. Marshall, Chem. Eng. Prog, 48 (1952) 141-146.

[65] C. Baumgarten, *Mixture Formation in Internal Combustion Engine* (Heat and Mass Transfer), Springer-Verlag, New York-Berlin, 2006.

[66] G. Damköhler, Z. Elektrochem. Angew. Phys. Chem., 46 (1940) 601.

[67] W. R. Hawthorne, D. S. Weddell, H. C. Hottel, Proc. Combust. Inst. 3 (1948) 266-288.

[68] R.W. Bilger, S. B. Pope, K. N. C. Bray, J. F. Driscoll, Proc. Combust. Inst 30 (2005) 21-42.

[69] D. Stirzaker, *Stochastic processes and models*, Oxford University Press, New York, 2005.

[70] S. Rigopoulos, Prog. Energy Combust. Sci. 36 (2010) 412–443.

[71] S.B. Pope, Prog. Energy Combust. Sci. 11 (1985) 119-192.

[72] R.O. Fox, *Computational Models for Turbulent Reacting Flows*, Cambridge University Press, Cambridge/New York, 2003.

[73] C. Dopazo, Phys. Fluids 18 (1975) 397‑404.

[74] S. B. Pope, Combust. Flame 27 (1979) 299‑312.

[75] J. Janicka, W. Kolbe, W. Kollmann, J. Non-Equilib. Thermodyn. 4 (1979) 47‑66.

[76] D.C. Haworth, Prog. Energy Combust. Sci. 36 (2010)168-259.

[77] K. W. Mao, H. L. Toor, AIChE 16 (1970) 49-52.

[78] K. J. Syed, C. D. Stewart, J. B. Moss, Proc. Combust. Inst. 23 (1991) 1533-1541.

[79] M. Fairweather, W. P. Jones, H. S. Ledin, R. P. Lindstedt, Proc. Combust. Inst. 24 (1992) 1067–1074.

[80] P. J. Coelho, M. G. Carvalho, J. Thermophys. Heat Transfer 9 (1995) 644-652.

[81] P. A. Libby, F. A. Williams, *Turbulent Reacting Flows*, T*opics in Applied Physics*, Springer-Verlag, Berlin-New York, 1980.

[82] K. N. C. Bray, M. Champion, P. A. Libby, N. Swaminathan, Combust. Flame 146 (2006) 665–673.

[83] N. L. Johnson, S. Kotz, N. Balakrishnan, *Continuous Univariate Distributions*, John Wiley & Sons, New York, 1995.

[84] L. Wang, R.O. Fox, AIChE J. 50 (2004) 2217-2232.

[85] T. S. Lundgren, Phys. Fluids 10 (1967) 969–75.

[86] T. S. Lundgren, Phys. Fluids 12 (1969) 485-497.

[87] C. Dopazo, E. E. Phys Fluids 17 (1974) 1968‑75.

[88] W. Kollmann, Theor. Comput. Fluid Dyn. 1 (1990) 249–285.

[89] S. B. Pope, J. Non-Equilib. Thermodyn. 7 (1982), 1-14.

[90] A.Y. Klimenko, Fluid Dyn. 25 (1990) 327-334

[91] R.W. Bilger, Phys. Fluids 5 (1993) 436-444.

[92] A. Kronenburg, R.W. Bilger, J. H. Kent, Combust. Flame 121 (2000) 24-40.

[93] A. Kronenburg, E. Mastorakos, Fluid Mech. Appl. 95 (2011) 91-117.

[94] D. B. Spalding, Proc. Combust. Inst. 13 (1971) 649–657.

[95] B. F. Magnussen, B. H. Hjertager, Proc. Combust. Inst. 16 (1977) 719–729.

[96] H. K. Versteeg, W. Malalasekera, *An introduction to computational fluid dynamics, The finite volume method*, 2nd ed. Pearson Education Limited, 2007.

[97] V. Golovitchev, N. Nordin, R. Jarnicki, J. Chomiak, SAE Technical Paper, 011891 (2000).

[98] P. A. Niklas Nordin, Complex Chemistry Modelling of Diesel Spray Combustion, PhD Thesis, Chalmers University of Technology, Gotheborg, Sweden, 2001.

[99] J. Chomiak, A. Karlsson, Proc. Combust. Inst. 26 (1996) 2557-2564.

[100] G. D'Errico, D. Ettorre, T. Lucchini, SAE Technical Paper 240045 (2007).

[101] R. Mikalsen, A.P. Roskilly, Appl.Energy 86 (2009) 1136-1143.

[102] J. Kusaka, Y. Daisho, J. KONES Internal Combust. Engines 10 (2003).

[103] M. Hallaji, K. Mazaheri, Comparison of LES and RANS in numerical simulation of *turbulent non-premixed flame under MILD combustion condition*, Mediterranean Combustion Symposium, Sardinia, Italy, 2011.

[104] M. A. Singer, S. B. Pope, Comb. Th. Model., 8 (2004) 361–383.

[105] S. K. Friedlander, *Smoke, Dust and Haze*, Oxford University Press, New York, 2000.

[106] T. T. Kodas, M. J. Hampden-Smith, Aerosol Proc. Materials, Wiley-VCH, New York, 1999.

[107] A. S. Myerson, R. Ginde, *Handbook of Industrial Crystallization*, Ed. A.S. Myerson. Butterworth-Heinemann, Boston, USA, 2002.

[108] D. Kashchiev, *Nucleation: Basic Theory with Applications*, Butterworth-Heinemann, Oxford, UK, 2000.

[109] R. Becker, W. Döring, Ann. d. Phys. 24 (1935) 719-752.

[110] J. W. Gibbs, *Collected Works, Vol. I, Thermodynamics*, Yale University Press, New Haven, USA, 1948.

[111] M. Volmer, *Kinetik der Phasenbildung*, Steinkopff, Leipzig, Germany, 1939.

[112] J. W. Mullin, *Crystallization*, 4th Ed., Butterworth-Heinemann, Oxford, UK, 2001.

[113] D. Kashchiev, G. M. van Rosmalen, Cryst. Res. Technol. 38 (2003) 555– 574.

[114] N. A. Fuchs, *The Mechanics of Aerosols*, Pergamon, Oxford, UK, 1964

[115] Y. Xiong, S. E. Pratsinis, A. W. Weimer, AIChE J. 38 (1992) 1685–1692.

[116] G. X. Yang, P. Biswas, J. Colloid. Interf. Sci. 211 (1999) 142-150.

[117] S. Tsantilis, H. Briesen, S. E. Pratsinis, Aerosol Sci. Technol. 34 (2001) 237-246.

[118] M. A. Asoro, D. Kovar, Y. Shao-Horn, L. F. Allard, P. J. Ferreira, Nanotechnol. 21 (2001) 025701-025706.

[119] R. M. German, *Sintering theory and practice*, John Wiley & Sons, New York, 1996.

[120] W. Koch, S. K. Friedlander, J. Colloid. Interf. Sci 140 (1990) 419-427.

[121] D. Ramkrishna, *Population Balances: Theory and Applications to Particulate Systems in Engineering*, Academic Press, New York, 2000.

[122] J. H. Seinfeld, *Atmospheric Chemistry and Physics of Air Pollution*, John Wiley & Sons, New York, 1986.

[123] Y. Xiong, S. E. Pratsinis, J. of Aerosol Sci., 24 (1993) 301–313.

[124] S. Tsantilis, H. K. Kammler, S. E. Pratsinis, Chem. Eng. Sci. 57 (2002) 2139-2156.

[125] F. E. Kruis, K. A. Kusters, S. E. Pratsinis, Aerosol Sci. Technol. 19 (1993) 514-526.

[126] R. Mueller, R. Jossen, H. K. Kammler, S. E. Pratsinis, M. K. Akhtar, AIChE 50 (2004) 3085-3094.

[127] H. Torabmostaedi, T. Zhang, P. Foot, S. Dembele, C. Fernandez, Pow. Technol. 246 (2013) 419-433.

[128] H. Mühlenweg, A. Gutsch, A. Schild, S. E. Pratsinis, Chem. Eng. Sci. 57 (2002) 2305 – 2322.

[129] T. Matsoukas, S. K. Friedlander, J. Colloid Interf. Sci. 146 (1991) 495-506.

[130] Y. Xiong, S. E. Pratsinis, J. Aerosol Sci. 24 (1993) 283-300.

[131] A. Kobata, K. Kusakabe, S. Morooka, AIChE J. 37 (1991) 347–359.

[132] G.D. Ulrich, Combust. Sci. Technol. 4 (1971) 47-57.

[133] Y. Xiong, S. E. Pratsinis, J. Aerosol Sci. 22 (1991) 637-655.

[134] A. P. George, R. D. Murley, E. R. Place, Symp. Farad. Soc. 7 (1973) 63-71.

[135] S. E. Pratsinis, P. T. Spicer, Chem. Eng. Sci. 53 (1998) 1861—1868.

[136] M. C. Heine, S. E. Pratsinis, Part. Part. Syst. Charact. 24 (2007) 56-65.

[137] J. I. Jeong, M. Choi, Aerosol Sci. 34 (2003) 965 – 976.

[138] A. Schild, A. Gutsch, H. Mühlenweg, S. E. Pratsinis, J. Nanopart. Res. 1(1999) 305–315.

[139] R. Hong , Z. Ren , J. Ding , H. Li, Chem. Eng. J. 108 (2005) 203–212.

[140] A. J. Gröhn, S. E. Pratsinis, K. Wegner, Chem. Eng. J. 191 (2012) 491–502.

[141] B. Buesser, S. E. Pratsinis, AIChE J., 57 (2011) 3132–3142.

[142] S. Tsantilis, S. E. Pratsinis, Langmuir 20 (2004) 5933-5939.

[143] M. Balthasar, F. Mauss, A. Knobel, and M. Kraft, Combust. Flame 128 (2002) 395–409.

[144] J. Baldyga, W. Orciuch, Transactions of the IChemE 75 (Part A) (1997) 160-170.

[145] M. Balthasar, M. Pfitzner, A. Mack, F. Mauss, J. Eng. Gas Turb. Pow. 124 (2000) 66-74.

[146] J. B. Moss, *Modelling soot formation for turbulent flame prediction. Soot formation in combustion: mechanisms and models* (H. Bockhorn, editor) Springer Series in Chemical Physics 5 (1995) 551–67.

[147] J. B. Moss, C. D. Stewart, K. J. Syed, Proc. Combust. Inst. 22 (1998) 413-43.

[148] R.P. Lindstedt, S.A. Louloudi, Proc. Combust. Inst. 30 (2005) 775-783.

[149] W. Kollmann, I.M. Kennedy, M. Metternich, J.-Y. Chen, Soot Formation in Combustion: Mechanisms and Models, (H. Bockhorn, editor) Springer-Verlag, Berlin-New York, 1994.

[150] J. Akroyd, A. J. Smith, R. Shirley, L. R. McGlashan, M. Kraft, Chem. Eng. Sci. 66 (2011) 3792-3805.

[151] S.B. Pope, Phys. Fluids 23 (2011) 011301.

[152] M. Muradoglu, P. Jenny, S. B. Pope, D. A. Caughey, J. Comp. Phys. 154 (1999) 342–371.

[153] G. Y. di Veroli, S. Rigopoulos, AIChE 56 (2010) 878-892.

[154] J. Baldyga, W. Orciuch, Chem. Eng. Sci. 56 (2001) 2435-2444.

[155] G. Y. di Veroli, S. Rigopoulos, Phys. Fluids 23 (2011) 043305.

[156] T. K. Lesniewski, S. K. Friedlander, Proc. R. Soc. London, Ser. 454 (1998) 2477–2504.

[157] N. Seubert, A. Kronenburg, O. T. Stein, *Large Eddy Simulation-Probability Density Function modelling of nucleation and condensation of DBP droplets in a turbulent jet*, ICLASS 2012, 12th Triennial Int. Conference on Liquid Atomization and Spray Systems, Heidelberg, Germany, 2012.

[158] J.D. Wilson, B.L. Sawford, Boundary-Layer Meteorology 78 (1996) 191-210.

[159] L. Bachelier, Théorie de la spéculation, Annales Scientifiques de l'école Normale Supérieure 3 (1900) 21-86.

[160] A. Einstein, Ann. d. Phys. 17 (1905) 549-560.

[161] J. Villermaux, J. C. Devillon, *Représentation de la coalescence et de la redispersion des domaines de ségrégation dans un fluide par un modèle d'interaction phénoménologique*, Proceedings of the 2nd Int. Symp. on Chemical Reaction Engineering, Elsevier, New York, 1972.

[162] C. Dopazo, E. E. O'Brien Acta Astronaut 1 (1974) 1239-1266.

[163] J. Janicka, W. Kolbe, W. Kollmann, J. Non-Equilib. Thermodyn. 4 (1977) 47-66.

[164] R. L. Curl, AIChE J. 9 (1963) 175-181.

[165] S. Subramaniam, S. B. Pope. Combust. Flame 115 (1998), 487-514.

[166] S Subramaniam, S. B Pope. Combust. Flame 117 (1999), 732-754.

[167] G. T. Linteris, M. D. Rumminger, V. I. Babushokc, Prog. Energy Comb. Sci. 34 (2008) 288-329.

[168] I. Wlokas, A. Faccinetto, B. Tribalet, C. Schulz, A. Kempf, Int. J. Chem. Kinetics 45 (2013) 487-498.

[169] N. Peters, *Turbulent Combustion*, Cambridge Monographs on Mechanics, Cambridge University Press, Cambridge/New York 2000.

[170] R. I. Issa, J. Comp. Physics 62 (1985) 40-65.

[171] L. Boltzmann, *Vorlesungen über Gastheorie*, J. A. Barth, Leipzig, 1896.

[172] H. Ge, E. Gutheil, *Coupled Joint PDF and Spray Flamelet Modelling for Methanol and Ethanol/Air Spray Combustion*, Proc. of the 21rst ILASS - Europe Meeting, Mugla, Turkey 2007.

[173] N. A. Beishuizen, *PDF modelling and particle-turbulence interaction of turbulent spray flames*, PhD thesis, Delft University of Technology, Delft, Nethaerlands, 2008.

[174] F. X. Demoulin, R. Borghi, Combust. Flame 129 (2002) 281-293.

[175] A. Rittler, F. Proch, A. Kempf, Combust. Flame, 162 (2015) 1575-1598.

[176] C. Hasse, N. Peters, Proc. Combust. Inst. 30 (2005) 2755-2762.

[177] C. Sheng, B. Moghtaderi, R. Gupta, T.F. Wall, Fuel 83 (2004) 1543-1552.

[178] C. Hollmann, E. Gutheil, Proc. Combust. Inst. 26 (1996) 1731–1738.

[179] E. Gutheil, W. A. Sirignano, Combust. Flame 113 (1998) 92-105.

[180] K. N. Bray and N. Peters *Laminar Flamelets in Turbulent Flames*, In P. A. Libby and F. A. Williams, editors Turbulent Reacting Flows. Academic Press. 63–114. 1994

[181] H. Pitsch, N. Peters, Proc. Comb. Inst. 27 (1998) 1057–1064.

[182] P. D. Lax, P. D. Richtmyer, Comm. Pure Appl. Math. 9 (1956) 267--293

[183] J. Crank, P. Nicolson, Proc. Camb. Phil. Soc. 43 (1947) 50–67.

[184] A. Harten, J. Comput. Phys. 49 (1983) 357–393.

[185] B.P. Leonard, Int. J. Num. Meth. Fluids 8 (1988) 1291–1318.

[186] P.H. Gaskell, A.K.C. Lau, Int. J. Num. Meth. Fluids 8 (1988) 617–641.

[187] P.K. Sweby, SIAM Journal on Numerical Analysis 21 (1984) 995–1011.

[188] H. Jasak, *Error Analysis and Estimation for Finite Volume Method with Applications to Fluid Flow*, PhD thesis, Imperial College, University of London, UK, 1996.

[189] B. van Leer, J. Comp. Phys. 14 (1974) 361–370.

[190] P.L. Roe, Ann. Rev. Fluid Mech. 18 (1986) 337–365.

[191] C. Hirsch, *Numerical computation of internal and external flows*, John Wiley& Sons, New York,1991.

[192] S. V. Patankar, *Numerical Heat and Mass Transfer*, Hemisphere Publ. Corp.,Washington, 1980.

[193] J. Crank, P. Nicolson, *A practical method for numerical evaluation of solutions of partial differential equations of the heat-conduction type*, Springer Verlag, Berlin-New York, 1947.

[194] OpenFOAM project web pages, available at www.openfoam.org (September 2014)

[195] H. Jasak, A.Jemcov, Z. Tukovic, *OpenFOAM: A C++ Library for Complex Physics Simulations*, International Workshop on Coupled Methods in Numerical Dynamics IUC, Dubrovnik, Croatia, 2007.

[196] P. A. Skovorodko, A. G. Tereshchenko, O. P. Korobeinichev, D. A. Knyazkov, A. G. Shmakov, Combust. Th. Model. 17 (2013) 1-24.

[197] Private communication Dr.-Ing. Christian Hecht.

[198] B. J. McBride, S. Gordon, M. A. Reno, NASA Report TM-4513 1993.

[199] C. R. Wilke, J. Chem. Phys. 18 (1950) 517-519.

[200] C. Weise, I.Wlokas, *Optimization of the setup and operating conditions simulation of nanoparticle synthesis reactors by simulation*, Aerosol Technology, Karlsruhe, Germany, 2014.

[201] T. A. Sipkens, R. Mansmann, K. J. Daun, N. Petermann, J. T. Titantah, M. Karttunen, H. Wiggers, T. Dreier, C. Schulz, Appl. Phys. B 116 (2014) 623-636.

[202] H. Wiggers, G. Schierning, I. Wlokas, C. Weise, N. Petermann, T. Schneider, N. Stein, J. Stötzel, *Microwave plasma synthesis of Si/Ge and Si/WSi2 nanoparticles for thermoelectric applications*, accepted by J. Physics D: Appl. Phys., as a Special Issue Article.

[203] C. Hecht, *Laserspektroskopische Charakterisierung von Reaktionsprozessen zur Gasphasensynthese von Nanopartikeln*, PhD Thesis, University of Duisburg–Essen, Duisburg, Germany, 2011.

[204] P. Ifeacho, T. Huelser, H. Wiggers, C. Schulz, P. Roth, Proc. Combust. Inst. 31 (2007) 1805–1812.

[205] P. Roth, A. Hospital, J. Aerosol Sci. 1 (1994) 61–73.

[206] B. Atakan, A. T. Hartlieb, J. Brand, K. Kohse-Höinghaus, Proc. Combust. Inst. 27 (1998) 435–444.

[207] H. Kronemayer, P. Ifeacho, C. Hecht, T. Dreier, H. Wiggers, C. Schulz, Appl. Phys. B 88 (2007) 373–377.

[208] W. G. Bessler, C. Schulz, V. Sick, and J. W. Daily, *A versatile modelling tool for nitric oxide LIF spectra*, (available at www.lifsim.com), 3rd Joint meeting of the US sections of the Combust. Inst., Chicago, 2003, PI05, 1-6.

[209] M. Marinov., W. J. Pitz, C. K. Westbrook, A. M. Vincitore, M. J. Castaldi, S. M. Senkan, Combust.Flame 114 (1998) 192-21.

[210] D. Goodwin, *Cantera: An object-oriented software toolkit for chemical kinetics, thermodynamics, and transport processes*, Caltech, Pasadena, 2009. [Online]. Available: http://code.google.com/p/cantera (accessed 01.08.2014).

[211] VDI-Wärmeatlas: Berechnungsblätter für den Wärmeübergang, Springer-Verlag, Berlin- New York 1997.

[212] C. Janzen, P. Roth, Combust. Flame 2001, 125, 1150–1161.

[213] S. R. Engel, A. F. Koegler, Y. Gao, D. Kilian, M. Voigt, T. Seeger, W. Peukert, A. Leipertz, Appl. Optics, 51 (2012) 6063-6075.

[214] T. Seeger, A. Leipertz, W. Peukert, *Gas Phase Temperature Measurements in a Flame Spray Pyrolysis Process by O_2 Pure Rotational CARS*, Laser Applications to Chemical, Security and Environmental Analysis, San Diego, California, USA, 2012.

[215] L. Maedler, W. J. Stark, S. E. Pratsinis, J. Mater. Res., 17 (2002), 1356-1362.

[216] S. Hardt, A. Hamid, C. Weise, I. Wlokas, H. Wiggers, C. Schulz, *Experimental and Numerical Investigation of Flame Spray assisted TiO2 Synthesis from Titaniumtetraisopropoxide*, 5th European Combustion Meeting, Cardiff, UK, 2011.

[217] C. Weise, J. Menser, S. Kaiser, A. Kempf, I. Wlokas, Proc. Combust. Inst. 35 (2015) 2259-2266.

[218] C. Weise, J. Menser, I. Wlokas, T. Dreier, C. Schulz, A. Kempf, H. Wiggers, *Towards a standardized nanoparticle synthesis spray flame,* MRS Fall Meeting & Exhibit, Boston, Massachusetts, USA, 2014.

[219] A. M. Thayer, Titanium Dioxide, Chem. Eng. News 9 (1998) 10-13.

[220] H. Hunter, *Formation and break up of microscale liquid jets*, PhD Thesis, Georgia Institute. Technol., Atlanta, USA, 2009.

[221] M. C. Heine, L. Maedler, R. Jossen, S. E. Pratsinis, Combust. Flame 144 (2006) 809-820.

[222] J. Menser, *Ramanstreuung an Nanopartikeln in der Gasphase*, Diploma Thesis, University of Duisburg-Essen, Duisburg, 2012.

[223] O. Desjardins, V. Moureau, E. Knudsen, M. Herrmann, H. Pitsch, *Conservative level set/ghost fluid method for simulating primary atomization*, Proc. ILASS Am. 20th Annu. Conf. Inst. Liq. Atom. Spray Syst. Am., Toronto, Canada, 2007.

[224] H. Grosshans, R.-Z. Szász, L. Fuchs, Int. J. Num. Meth. Fluids, 74 (2014) 898–918.

[225] C. K. Westbrook, F.L. Dryer, Combust. Sci. Technol. 27 (1981) 31–34.

[226] T. Seto, M. Shimada, K. Okuyama, Aerosol Sci. Technol. 23 (1995) 183–200.

[227] K. Okuyama, R. Ushio, Y. Kousaka, R. C. Flagan, J. H. Seinfeld, AIChE J. 36 (1990) 409–419.

[228] P. Rosin, E. Rammler, J. Inst. Fuel 7 (1933) 29-36.

[229] Private communication Dipl.-Phys. Jan Menser.

[230] J. D. Landgrebe, S. E. Pratsinis, J. Colloid. Interf. Sci. 139 (1990) 63–86.

[231] P. T. Spicer, O. Chaoul, S. Tsantilis , S. E. Pratsinis, Aerosol Sci. 33 (2002) 17–34.

Nomenclature

A	particle surface area concentration	[m^{-1}]
A	pre-exponential factor	[s^{-1}]
a	primary particle surface area	[m^2]
a_s	primary particle surface area of a spherical aggregate	[m^2]
C	fraction function	[-]
c	particle velocity	[m s^{-1}]
c	mass concentration	[kg m^{-3}]
C_d	drag coefficient	[-]
D	diffusion coefficient	[m^2 s^{-1}]
D_f	fractal dimension	[-]
d	diameter	[m]
E_A	activation energy	[J]
F	mass flux through a face	[kg s^{-1}]
$\boldsymbol{F_d}$	drag force	[N]
$\boldsymbol{f_V}$	volume forces	[N]
G	surface free energy	[J m^{-2}]
g	transition parameter	[m]
$\boldsymbol{g}$	gravitational coefficient	
h	specific enthalpy	[J kg^{-1}]
I	particle nucleation rate	[m^{-3} s^{-1}]
$\boldsymbol{I}$	unit vector	[-]
$\boldsymbol{J}$	diffusion flux	[mol m^{-2} s^{-1}]
K_c	equilibrium constant	[-]
k	turbulent kinetic energy	[m^2 s^{-2}]
k_f	reaction coefficient for forward reaction of order n	[mol^{-n+1} l^{n-1} s^{-1}]
k_b	reaction coefficient for backward reaction of order n	[mol^{-n+1} l^{n-1} s^{-1}]
l	particle mean free patch	[m]
M	molar mass	[kg mol^{-1}]
m	mass	[kg]
$\dot{m}$	mass flow	[kg s^{-1}]

N	particle number concentration	[m^{-3}]
$\boldsymbol{n}$	normal vector	[-]
n	number	[-]
n	particle size distribution function	
P	probability	[-]
P_k	production of turbulent kinetic energy	[$m^2 s^{-3}$]
p	pressure	[Pa]
$\dot{\boldsymbol{q}}$	heat flux	[W m^{-2}]
$\boldsymbol{R}$	Reynolds stress tensor	[N m^{-2}]
R_R	reaction rate	[mol $l^{-1} s^{-1}$]
r	radius	[m]
r_c	collision radius	[m]
$\dot{r}$	formation velocity	[mol $l^{-1} s^{-1}$]
S	supersaturation ratio	[-]
S	source/ sink term	
Sp	linear part of a source/ sink term	
Su	constant part of a source/ sink term	
$\overline{\boldsymbol{S}}$	Reynolds averaged strain rate tensor	[s^{-1}]
s	stoichiometric oxygen-fuel	[-]
T	temperature	[K]
$\boldsymbol{T}$	stress tensor	[N m^{-2}]
t	time	[s]
$\boldsymbol{U}$	velocity in the Lagrangian frame	[m s^{-1}]
$\boldsymbol{u}$	velocity	[m s^{-1}]
V	particle volume concentration	[-]
V	volume	[m^3]
v	primary particle volume	[m^3]
$\boldsymbol{X}$	particle position	[-]
X	chemical symbol	[-]
x_s	surface molar fraction	[-]
$\boldsymbol{x_c}$	cell centre	[-]

y	mass fraction	[-]
Z	mixture fraction	[-]

Greek

$\alpha.$	heat transfer coefficient	[W m^{-2} K^{-1}]
$\alpha.$	volume fraction	[-]
β	collision frequency	[s^{-1}]
ε	dissipation of turbulent kinetic energy	[m^2 s^{-3}]
λ	thermal conductivity	[W m^{-1} K^{-1}]
λ_x	interpolation factor	
μ	dynamic viscosity	[Pa s]
μ	Gibb's potential	[J mol^{-1}]
μ_{eff}	effective viscosity (dynamic +turbulent viscosity)	[Pa s]
ν	kinematic viscosity	[Pa s m^3 kg^{-1}]
ν_i	stoichiometric coefficient	[-]
ρ	density	[kg m^{-3}]
σ	collision diameter	[m]
σ_s	surface tension	[N m^{-1}]
τ	characteristic time	[s]
φ	intensive scalar	
$\boldsymbol{\phi}$	state vector	
$\boldsymbol{\varphi}$	composition vector	
$\boldsymbol{\psi}$	composition space	[-]
Ω	collision integral	[-]
ω	turbulent mixing rate	[s^{-1}]
$\dot{\omega}_h$	energy rate due to chemical reactions	[J s^{-1} m^{-3}]

Dimensionless quantities

Da	Damköhler number
Kn	Knudsen number
Nu	Nusselt number

Ma	Mach number
Oh	Ohnesorg number
Pr	Prandtl number
Re	Reynolds number
Sh	Sherwood number
Sc	Schmidt number
We	Weber number

A. Implementations in OpenFOAM

In this chapter the implementation of the new solvers, libraries and routines in OpenFOAM, which was done for the present work is explained. For this thesis, the OpenFOAM version 2.2.x was applied. This documentation is not a general part of the research work; it is provided for further advancements of the modelling approaches presented in this thesis.

A.1. New libraries

The **EBU model** has to be implemented in OpenFOAM, because the existing model for infinitely fast chemistry in OpenFOAM differs from the standard EBU model. The existing infinitely fast chemistry classes were taken as the basis for the implementation of the EBU approach and the routine for the calculation of the fuel consumption rate in the file *infiniteFastChemistry.C* was adjusted according to Equation 74. This file is located in the *myCombustionModels02_EBU* library.

The precursor TTIP is dissolved in the liquid fuel, which was isopropyl alcohol. For **TTIP,** the **evaporation** characteristics and material properties, which are required to calculate the evaporated mass flow rate, are unknown. Thus, the evaporation characteristics of TTIP and C_3H_8O are assumed to be equal. The injected liquid therefore consists of pure C_3H_8O and the evaporated mass flow rate of C_3H_8O is split into an amount of gaseous C_3H_8O and TTIP due to the real mass fraction of each of the both species in the liquid. The precursor evaporation rate was implemented into the library of the spray particles (the new libraries are denoted as *myIntermediate* for the Euler-Euler modelling and *myIntermediateMC* for the Monte Carlo calculation). The calculation of the evaporation rate is performed in the file *ReactingCloudI.H* in the method *SYi*, where the source term for the species conservation equation is determined. Additionally to the solver, the Lagrangian spray library, denoted as *spray*, has to be linked with this new library.

For the **particle nucleation rate**, a new method was implemented to calculate the nucleation according to the production rate of TiO_2 molecules (Equation 107). For the PaSR model, the production rate was defined within the new libraries *myCombustionModels* and *myChemistryModels* with the method *dC*, which is determined in *PaSR.C* and *chemistryModel.C*. For the Euler-Euler calculation using the EBU model, the nucleation term is determined in the library *myCombustionModels_Euler_Euler* and *myChemistryModels* with the routine *dC* in *infinitelyFastChemistry.C* and *chemistryModel.C.* For the Monte Carlo particles, a new object (*RRp*) was defined in the new Lagrangian Monte Carlo library (*monteCarlo13_var*) in *MonteCarloParcel.C* to determine the nucleation rate from the decomposition rate of the precursor for each Monte Carlo particle.

The **calculation of the mixture fraction field** (*Mf*) was implemented in the library *myCombustionModels02_EBU* in the source file *singleStepCombustion.C*.

A **new library** was implemented for the **Monte Carlo particles**, where the emergence and evolution of the Monte Carlo particles and the PBE for each particle are calculated. A new cloud class, the *monteCarloCloud* was created, where the basis was the existing *kinematicCloud* class. Therefore, the code of the libraries in the *intermediate* directory was modified and extended, where the new library included 435 files with more than 150,000 lines of code, whereof more than 9000 lines were newly created from scratch. The calculation of the population balance equations (according to Equations 106-110), the change of the mixture fraction and the precursor mass fraction, the nucleation rate (according to Equation 107) and the required coefficients (according to Equations 102-106) is located in the source file *MonteCarloParcel.C*. Therefore, this source file is the most important file within the *monteCarloCloud* class. The new properties of the Monte Carlo particles are initialised in the constructor of the class *MonteCarloParcel*. The calculation of the mean temperature field and the particle number field is performed in the file *MonteCarloCloudI.H*.

A.2. New solvers

Altogether, four solvers were implemented in OpenFOAM, where the basis was the *reactingFoam* solver. Solvers were created for each simulation model, where for the Monte Carlo model, one solver was used for the determination of the initial field followed by a second solver for the solution of the Monte Carlo approach. For all solvers, all methods are defined in the source file *sprayFoam.C*. The list of the linked libraries for each solver is given in the *options* file located in the *Make* directory. The individual solvers and methods are subsequently described in detail.

EBU

The calculation of the mixture fraction field is called by the statement *Mf = combustion->Mf()* in the header files *YEqn.H*. The statement *combustion->Mf().write()* in the source file *sprayFoam.C* is called to write out the mixture fraction field *Mf*. The new implemented object *Mf* is created and initialized in the header file *createFields.H*. The EBU constants according to Equation 74 are not hard coded in the solver; they have to be set individually for each case in the file constant/combustionProperties.

Spray particle calculation for the methods PaSR02, EBU and MC

For the solvers, which include spray particle evolution and evaporation, the function call for the determination of the spray particle evolution is the statement *parcel.evolve()*. The additionally implemented header file for the calculation of the spray particles is *createClouds.H*. Within this header file, the object *parcel* of the class *basicSprayCloud* is

created. The source and sink terms according to the spray particle evaporation, denoted as *parcels.Srho(), parcels.SU(U), parcels.Sh(he)* and *parcels.SYi(i, Yi),* are implemented in the header files *pEqn.H, UEqn.H, EEqn.H* and *YEqn.H*, respectively.

PaSR02

The transport equations for the nanoparticle number, surface area and volume concentration (according to Equations 108-110) are implemented in the new header file *ParticleEqn.H*. The required coefficients (according to Equations 102-106) are provided in the file *calculateParticleCoe.H*. The implemented variables for the calculation of the nanoparticle dynamics are created and initialized in the file *createParticleFields.H* and the constants are defined in *particleConstant.H*, respectively.

EBU

The *EBU* solver calculates the nanoparticle dynamics equations for the number, surface area and volume concentration in a post-processing step. Therefore, the velocity, pressure, and temperature fields are kept constant. The nanoparticle transport equations, the coefficients and constants are determined with the additional header files *ParticleEqn.H*, *calculateParticleCoe.H, createParticleFields.H,* and *particleConstant.H,* as described for the solver *PaSR02.*

MC

For the *MC* approach, two cloud classes have to be distinguished: the *basicSprayCloud*, where the evolution and evaporation of the spray particles are determined and the *basicMonteCarloCollidingCloud*, which corresponds to the new implemented Monte Carlo particle routine.

The number of Monte Carlo particles, which emerge due to evaporation of the spray particles, is determined in the header file *YEqn.H*. Each initialized Monte Carlo particle is a parcel, which represents a certain number of gas molecules. The number of TTIP parcels is determined with the variable XTTIP and the number of C_3H_8O parcel with the variable XC3H8O, respectively. The initialisation of the corresponding Monte Carlo particles is implemented in the source file *sprayFoam.C*. According to the previous calculated number of Monte Carlo particles new objects, denoted as *newParcel*, of the class *basicMonteCarloCollidingParcel* are created. The members of the Monte Carlo particle object are initialised. These members are the standard particle variables (default in the OpenFOAM library intermediate) and additionally, the particle ID, the mixture fraction and the precursor mass fraction. Only an integer number of particles can be created, therefore, a method was implemented to consider the decimal places of the calculated particle numbers *XTTIP* and *XC3H8O*, respectively. A random number between 0 and 1 is determined: if this

number is smaller than the particle number's decimal place, an additional Monte Carlo particle is created. The number of Monte Carlo particles, which are injected at the reactor inlets, has to be defined for each case in the file *monteCarloCloudProperties* in the *constant* directory. The statement *monteCarloCloud.evolve()* calls the Monte Carlo particle routines. The particle number within a cell is determined by the statement *Np = monteCarloCloud.SN()* and the average temperature by *T = monteCarloCloud.ST()*, respectively. The density field is calculated from the temperature in the header file *rhoEqn.H*. In the file *createClouds.H*, the additional object *monteCarloCloud* of the class *basicMonteCarloCollidingCloud* is created. The implemented variables are created and initialized in the header file *createFields.H*.